FLORIDA STATE UNIVERSITY

COLLEGE OF ARTS AND SCIENCES

INVESTIGATION OF THE NEUTRON-RICH OXYGEN ISOTOPES AT THE DRIP LINE

By

CALEM R. HOFFMAN

A Dissertation submitted to the
Department of Physics
in partial fulfillment of the
requirements for the degree of
Doctor of Philosophy

Degree Awarded:
Spring Semester, 2009

The members of the Committee approve the Dissertation of Calem R. Hoffman defended on February 6, 2009.

Samuel L. Tabor
Professor Directing Dissertation

Kenneth A. Goldsby
Outside Committee Member

Grigory Rogachev
Committee Member

Alexander Volya
Committee Member

Peng Xiong
Committee Member

The Graduate School has verified and approved the above named committee members.

To the pursuit of science simply for fun...

ACKNOWLEDGEMENTS

I would first like to thank my adviser, mentor, and friend over the last nine years Dr. Sam Tabor. He first turned my eyes toward the exciting world of nuclear physics when I was only a freshman, and has continually supported me from then on. Without his guidance and endless wisdom I would be lost, Thank you. In the same tone I would like to thank my adviser from afar Dr. Michael Thoennessen who provided me with countless opportunities I never thought possible. And who, encouraged and supported me from my time in Michigan until now, Thank you. Also, I would like to thank the members of my committee Grigory Rogachev, Alexander Volya, Peng Xiong, and Kenneth A. Goldsby, for their insight and interest into my work.

My thanks go out to everyone in the scientific community who has aided me in my journey, most notably Kirby Kemper, Mark Riley, Ingo Wiedenhover, Vandana Tripathi, Paul DeYoung, Thomas Baumann, Paul Mantica, and John Schiffer. Also, thanks are extended to the MoNA Collaboration members and the staff at the John D. Fox Superconducting Accelerator Laboratory, including Dave Spingler, Powell Barber, Dave Caussyn, Lagy Baby, Gerry Hutchins, Greg Brown, and Brian Schmidt.

I would like to thank the large number of past and present graduate students whom I have had the pleasure to call friends over my graduate career: Matt, Mathis, John, Dave, Akis, Kushal, Josh and Josh, Alfredo, Jon, Aaron, Chuck, Koshiro, Eric, Joe, Alex, Patrick, Michelle, Peter, Rob, and Matt.

Last but most certainly not least I would like to thank my family and close friends. Mom and Torissa, you have always supported me in everything I have done, I couldn't have asked for anything more. Thank you for all the opportunities you have given me and for showing me what it means to be a strong person. I hope you two are happy everyday, and I love you both very much! To April, for keeping me sane and making me so very happy! To the best friends that there ever were, ATHF for life; Jason, Aaron, John, the TJ, Payne and Gary.

TABLE OF CONTENTS

LIST OF TABLES

LIST OF FIGURES

ABSTRACT

To investigate the appearance of a new magic number at neutron number 16, resonance states around the oxygen ($Z = 8$) drip line have been investigated. The neutron unbound states were populated by a nucleon removal reaction from a radioactive ^{26}F ion beam and the invariant mass method was used to reconstruct the resonance decay spectrum. The secondary radioactive ^{26}F beam was created by the fragmentation of a ^{48}Ca beam, produced by the National Superconducting Cyclotron Laboratory's Coupled Cyclotron Facility, and was cleanly selected by the A1900 fragment mass analyzer. A complete kinematic measurement was made of the decay neutron and fragment using the Modular Neutron Array (MoNA) to detect neutrons, and the large gap dipole Sweeper magnet combined with charged particle detectors to select and measure the charged fragments.

Resonance spectra were reconstructed for both ^{24}O+n and ^{23}O+n coincidence data to investigate the resonance states in ^{25}O and ^{24}O, respectively. To extract resonance energies and widths from the spectra, a Breit-Wigner line-shape function was input into a Monte Carlo simulation that reflected the experimental response. A fit which minimized χ^2 was completed for each spectrum and for the ^{24}O+n coincidence data a single resonance at a decay energy of $E_{\mathrm{decay}} = 770^{+20}_{-30}$ keV and with a width of $\Gamma = 172(30)$ keV was determined. Two resonances of energies $E_{\mathrm{decay}} = 0.63(4)$ MeV and $E_{\mathrm{decay}} = 1.24(7)$ MeV were found in the fit to the ^{23}O+n coincidence data. The single state in the ^{24}O+n coincidence data is the first mass measurement of the ground state of the lightest neutron unbound oxygen isotope, ^{25}O. The two states in the ^{23}O+n data have been determined to be the first observation of the 2^+ and 1^+ neutron unbound excited states in ^{24}O.

The ground state mass of ^{25}O was used to determine the location of the $\nu 0d_{3/2}$ orbital at the oxygen drip line, and hence, determine the size of the $N = 16$ shell gap to be

4.86(13) MeV at this location. Also, the ground state mass measurement provided the one- and two-neutron separation energies for ^{25}O. Each of these observable were compared to shell model calculations using various interactions. Curiously, the interaction which best reproduced the experimental data was the universal *sd* shell model which calculates a bound ^{26}O ground state, contrary to experiment.

The two excited states observed in ^{24}O were also compared to a number of theoretical calculations. The best description of the data was found by a calculation which explicitly included a continuum $\nu 0d_{3/2}$ orbital into wave function. The $N = 16$ shell gap was also determined from the two states to be 4.95(16) MeV, in excellent agreement with the ^{25}O result (4.86(13) MeV). Finally, the energy of the first excited 2^+ state observed in ^{24}O was systematically compared with the same state in other nearby even-even nuclei. It was determined that ^{24}O is in fact a doubly magic nucleus having a magic number of protons $Z = 8$ and neutrons $N = 16$, due to the relatively high energy of its 2^+ excited state.

CHAPTER 1

INTRODUCTION

Investigating the outermost reaches and beyond the limits of the explored has forever been a key driving force in all scientific fields because it has so often led to fundamental new science. The discovery of something original, something that has never been observed before, not only quenches the thirst for curiosity but also adds new information to extend our understanding of the world around us. Such thrusts in forefront research have led to our current understanding of the four forces of nature - gravity, electromagnetic, strong, and weak. By searching and probing nuclei at the extremes, nuclear science can do its part to further advance the understanding of these forces and help provide a more complete picture of the physical world.

A window to gain a view of the characteristics of the strong force is to try and answer one of the most fundamental questions in nuclear physics: what combinations of protons and neutrons can bind together to make nuclei?? Physically this question is asking at which two points along an isotopic chain (constant Z) does the strong force saturate, and therefore, can no longer bind another nucleon to the nucleus. For light neutron-rich nuclei the determination between a particle-bound nucleus and a particle-unbound nucleus is easily distinguished because of the drastically different lifetimes between them. Bound neutron-rich nuclei will decay towards the valley of stability, or the line of stable nuclei, by β^- decay. This decay is mediated by the weak force and a typical lifetime for a β^- decaying state is on the order of milliseconds (1 millisecond = 10^{-3} seconds) up to hours or longer. However, when the nuclear strong force reaches its maximum capacity and the outermost neutron is unbound, the decay occurs on the time scale of zeptoseconds (1 zeptosecond = 10^{-21} seconds). The roughly 18 orders of magnitude difference between the decay times of the strong and weak decays, makes determination of a neutron-rich unbound nucleus versus

a bound one, relatively straight forward. The neutron drip line has only been mapped out for the lightest isotopes up to oxygen ($Z = 8$), and theoretical predictions above this differ substantially.

The one caveat to the determination of the neutron drip line, is that the nuclei in this region must be produced. With the recent advancements in accelerator physics throughout the world, more and more exotic nuclei are being produced. In particular, the advent of radioactive beams, which are beams of unstable nuclei, has opened doors to study more neutron-rich nuclei than ever before. The National Superconducting Cyclotron Laboratory (NSCL) at Michigan State University, and the John D. Fox Superconducting Accelerator Laboratory are two examples of such radioactive beam facilities. Furthermore, progress in technology and ingenuity has allowed for the detection and study of these exotic nuclei. One such device is the Modular Neutron Array (MoNA), used to detect neutrons with high efficiency, and good timing and position resolutions.

The location of the neutron drip line may be strongly influenced by the location of the magic nucleon numbers. The magic numbers in nuclei were first discovered by the experimental study of a large number of nuclei near stability. From these studies, clear experimental signatures arose for certain numbers of protons and neutrons. The signatures included increased binding energies, larger numbers of stable isotopes, high-energy first excited states, and decreased collectivity. The proton and neutron numbers that were deemed magic near stability were $N = Z = 2, 8, 20, 28, 50, 82$ and 126. Theoretically, these magic numbers came to be described by large energy gaps between single-particle energy orbitals in the nuclear shell model. Recently, experimental evidence has shown that the magic numbers for neutron-rich nuclei may change due to the evolution of the energies of the single-particle orbitals. This results in the disappearance of certain traditional magic numbers, while new magic numbers may appear. Whether a magic number exists or not near the neutron drip line greatly affects where the last bound nucleus may lie.

The properties of nuclei near, at, or beyond the neutron drip line may best be studied using neutron spectroscopy. The reason for this is simply that bound states, both ground states and excited states, cease to exist near the neutron drip line. Therefore, typical techniques used to study the structure of nuclei, such as γ ray detection or β detection, are ineffective. Hence, neutron spectroscopy must by employed as it is the most viable option in these cases. Because the neutron unbound states have extremely short lifetimes (on the order

of 10^{-21} seconds), they typically have decay widths on the order of keV to MeV as determined by the uncertainty principle. These states are therefore deemed resonance states, and their energies and decay widths provide important nuclear structure information on nuclei around the drip line in an experimentally unique way.

An interesting region of the nuclear landscape that is currently a mystery, and which may be understood through the probe of neutron spectroscopy, is around the neutron-rich oxygen drip line. Experimentally it has been observed that the oxygen ($Z = 8$) drip line abruptly ends at $N = 16$ ^{24}O, in sharp contrast to the fluorine ($Z = 9$) drip line, which extends to at least $N = 22$ ^{31}F. No theoretical explanation has been provided to fully explain the allowance of the binding of at least an additional 6 neutrons by adding only a single proton. A possible partial solution has been conjured, that for the oxygen isotopes, a new magic number appears at $N = 16$. Some indirect evidence for this new magic number has been found; however, a direct measure of the energy gap has not occurred. Whether a new magic number exists, direct measurement of it would add a great deal of insight into this region.

Two of the neutron-rich oxygen isotopes, in particular, the last bound nucleus ^{24}O, and the first unbound nucleus ^{25}O, are to be the focus of this thesis work. The outline for the thesis is as follows: The background and motivation for the experimental work will be given first, followed by an explanation of the experimental and theoretical techniques and tools that were needed to complete the study. Then, the analysis procedure and the results of the experimental work will be presented, followed by a discussion and interpretation of these observed values and their impact on the nuclear structure of neutron-rich nuclei. Finally, the entire work will be summarized.

CHAPTER 2

MOTIVATION

2.1 The Neutron Drip Line

Recently two neutron-rich isotopes (^{42}Al and ^{40}Mg) have been discovered at the National Superconducting Cyclotron Laboratory (NSCL) at Michigan State University [3]. The observation of these bound ground states is a general indication that the nuclear force is not well understood at the nuclear extremes and more investigation along the neutron drip line is needed. In Fig. 2.1 a section of the Chart of the Nuclides; which plots the combinations of protons (vertical axis) and neutrons (horizontal axis), shows the newly observed isotopes as well as all other observed isotopes from carbon to chlorine ($Z = 6 - 17$). Experimentally, the drip line has only been established up to oxygen; however, it had been believed that the drip line had been reached up to sodium until this recent observation of ^{40}Mg.

In their work, a ^{48}Ca beam at 141 MeV/u was fragmented on a ^{nat}W target to produce the exotic Mg and Al isotopes. The ^{40}Mg and ^{42}Al isotopes were separated and then identified by their energy loss and time-of-flight (ToF) information. The observation of ^{40}Mg alone is interesting as it extends the $Z = 12$ drip line to $N = 28$ and opens the question as to the location of the drip line below Mg, i.e. for fluorine, neon, and sodium. ^{40}Mg is in fact even-even, having $Z = 12$ and $N = 28$, so the extra binding energy from the nucleon pairing does not make this discovery a huge surprise as the staggered drip line is continued from fluorine to magnesium (see Fig. 2.1). ^{42}Al having a bound ground state however, disrupts the staggered pattern and since it has an odd number of both protons and neutrons, its discovery is quite surprising. This now suggests that for $Z = 13$ and above, the drip line may in fact shift toward more heavy isotopes than was previously thought.

To investigate this point, two of the best global mass models were chosen to compare with the experimental data, the finite range droplet model (FRDM) [4] and the Hartee-

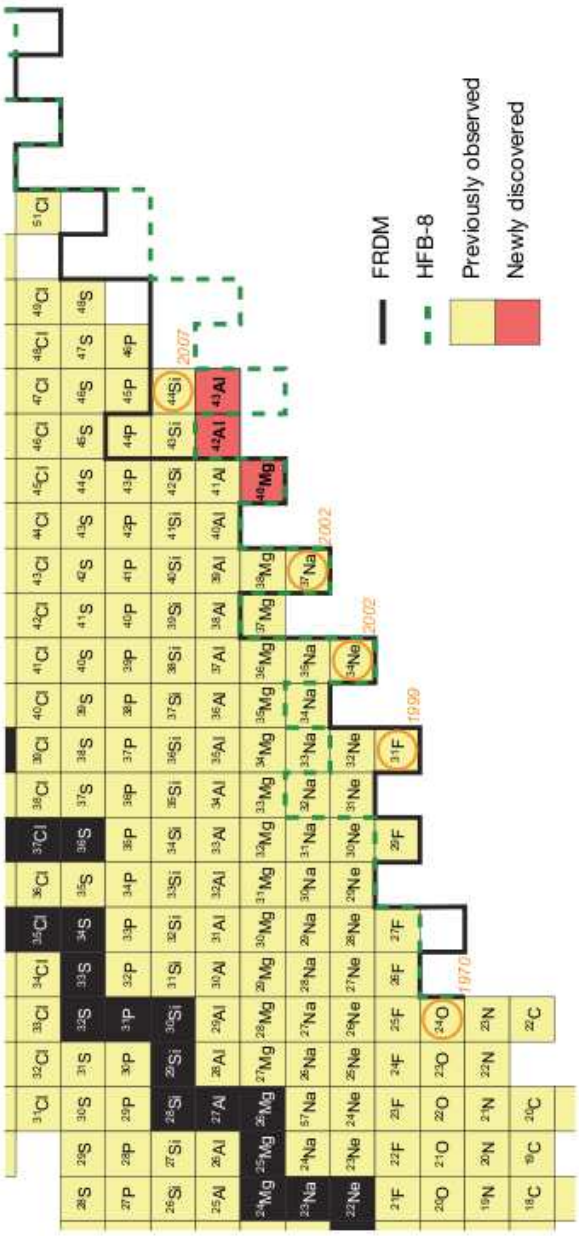

Figure 2.1: A section of the Chart of the Nuclides taken from Ref. [3] showing the experimentally observed neutron-rich nuclei from carbon (C $Z = 6$) to chlorine (Cl $Z = 17$). Proton number increases upward in the vertical direction and neutron number increases to the right in the horizontal direction. The drip line predictions of the finite range droplet model (FRDM) [4] and the Hartree-Fock-Bogoliubov model (HFB-8) [5] are also shown by the solid and dashed lines respectively.

Fock-Bogoliubov model (HFB) [5]. The predictions of these two models are shown by the solid (FRDM) and dashed (HFB-8) lines in Fig. 2.1, where clear discrepancies are seen between their drip line predictions. The FRDM is macroscopic in nature with the addition of microscopic corrections for the single-particle structure as well as the pairing effects. The HFB-8 version of the HFB model was chosen as it best reproduces the experimentally measured masses. It is quite on the opposite side of the FRDM as it is a fully microscopic model and is a contemporary quantum mechanical calculation. As can be seen in Fig. 2.1 both models have difficultly describing the regions around Mg-S and O-Na, while neither correctly predicted the bound ground state of ^{42}Al.

Focusing around the oxygen and fluorine region in Fig. 2.1, it is interesting to see the large difference in the observed drip lines for these two elements. Experimentally it has been determined that the bound oxygen isotopes abruptly end at $N = 16$ ^{24}O while the fluorine isotopes extend to at least $N = 22$ ^{31}F [6, 7, 35, 36, 37, 38, 39]. These measurables suggest that the addition of a single proton from $Z = 8$ oxygen to $Z = 9$ fluorine allows for the binding of, at minimum, 6 more neutrons. Searches for ^{26}O and ^{28}O were very prevalent, as many predictions had ^{26}O bound to two neutron decay; however, no bound events have been observed for either isotope. Shown in Fig. 2.2 are the data from two such searches for the neutron-rich oxygen isotopes as well as evidence for the binding of ^{31}F. As can be clearly seen there are empty holes were the expected ground states of the oxygen isotopes should be if they are in fact bound to neutron emission.

An expanded view of this region is shown in Fig. 2.3 where the FRDM and HFB-8 model predictions are shown by the solid red line and dashed green line respectively. Neither model is able to describe the fact that the oxygen isotopes are only able to bind until $N = 16$ (^{24}O) while the fluorine isotopes can handle an additional 6 neutrons up to at least $N = 22$ (^{31}F). As can be seen, the FRDM correctly (as far as we know) reproduces the fluorine and neon drip lines. However, it overshoots the oxygen drip line by predicting a bound ^{26}O ground state. The HFB-8 is the inverse of this as it predicts correctly the end of the oxygen drip line while coming up extremely short for the fluorine ($N = 18$) and neon ($N = 20$) drip lines.

A similar situation exists when the predictions of the oxygen drip line are investigated by a number of different shell model interactions (USD, USD05a,b and SDPF-M) [11, 13, 27]. The oldest of the interactions is the original universal *sd* (USD) shell model interaction [13]. This interaction is defined by the 63 two-body matrix elements (TBMEs) and 3 single-particle

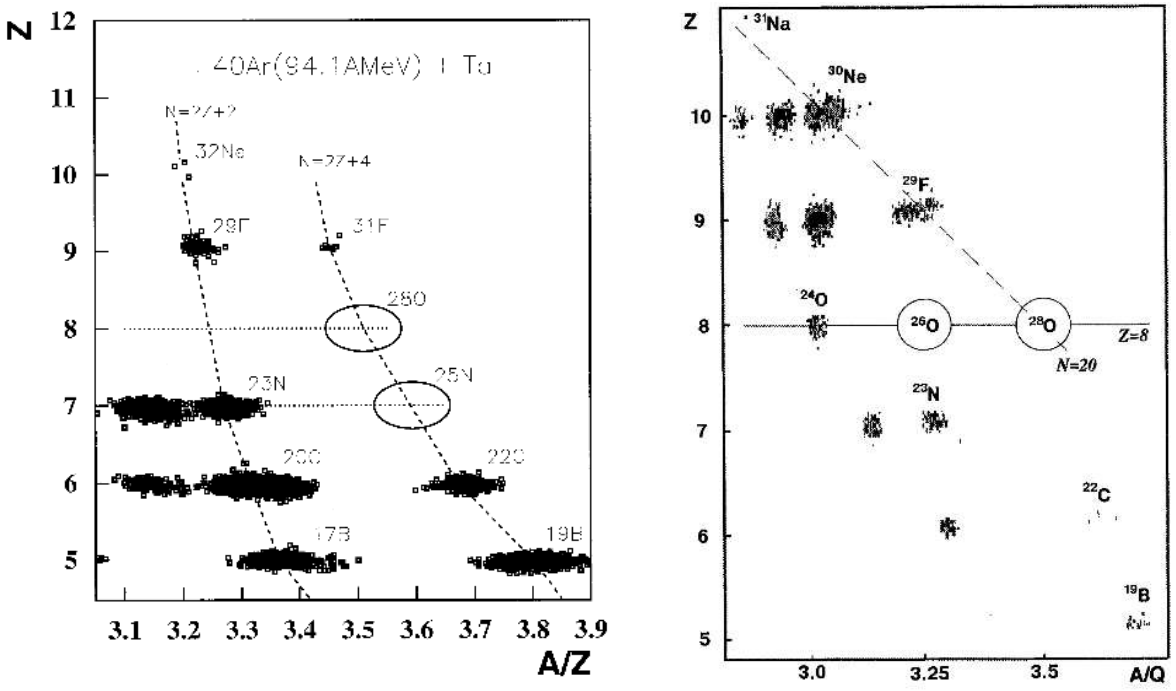

Figure 2.2: Two examples of particle identification plots from searches for bound ground states of the fluorine and oxygen isotopes. They each show element number Z on their vertical axis and mass over charge A/Z on their horizontal axis. The figure on the left comes from the fragmentation of a ^{40}Ar beam at 94.1 A MeV on a Ta target [6] and on the right is the results from the fragmentation of a ^{36}S at 78 A MeV on a Ta target [7]. Clearly noticed are the events identified for ^{29,31}F and the absence events for ^{26,28}O.

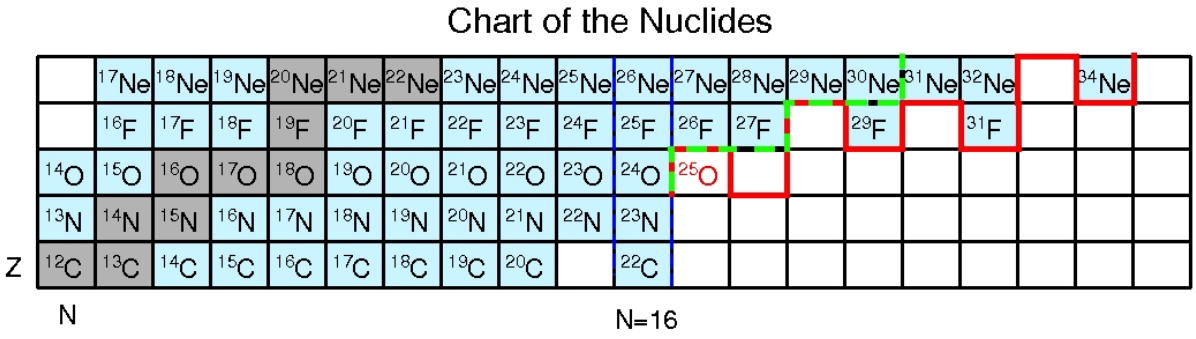

Figure 2.3: A selected region of the chart of the nuclides is shown for the neutron-rich carbon (C $Z = 6$) to neon (Ne $Z = 10$) isotopes. All nuclei that are shown have been observed experimentally and therefore lie within the drip line except for ^{25}O. The calculated drip line locations from the FRDM (solid red line) and the HFB-8 (dashed green line) mass models are also shown on the chart.

energies (SPEs) of the *sd* shell, which encompasses $A = 16 - 40$. The TBMEs and SPEs were first calculated from a real nucleon-nucleon (NN) potential to create a re-normalized G-matrix, and then were adjusted so as to reproduce the experimental data in the *sd* shell region. Recently, the USD interaction has been refitted to the plethora of new data available since its inception in 1988. The resulting interactions (USD05a and USD05b) differ by the fact that only a selection of the TBMEs were allowed to vary in the fit for the USD05a, while a completely free fit was performed to create the USD05b [27]. A highlight of this new fit was a much clearer delineation of the "island of inversion" by the large discrepancy in the ground state binding energies for $Z = 10 - 12$ [27]. Finally, three separate components were combined to create an interaction that allowed for calculations spanning across both the *sd* and *pf* shells. This interaction, referred to as the SDPF-M interaction, is made of the original USD interaction in the *sd* shell, the Kuo-Brown interaction for the *fp* shell, and a cross shell component based on the Millener-Kurath interaction. Slight modification were made however, including an adjustment of the $T = 1$ monopole terms for $0d_{5/2} - 0d_{3/2}$ and $0d_{5/2} - 0f_{7/2}$ to force the interaction to calculate the oxygen drip line at ^{24}O, i.e. an unbound ^{26}O ground state. Furthermore, care was taken to remove some pairing strength in the USD interaction as effects from the *fp* shell will be handled explicitly. More details of the shell model interactions will be presented in chapter 3.

The older USD interaction incorrectly calculates that ^{26}O is bound by two-neutron emission by 1 MeV, while the more recent fits to the data (USD05a,b) both correctly calculate an unbound ground state by ∼500 keV. The SDPF-M interaction also predicts an unbound ^{26}O ground state (-80 keV) by design. The SDPF-M interaction can also predict the binding energies for fluorine as it is not confined to the *sd* shell and in doing so it is seen that it incorrectly calculates the fluorine drip line to lie at $N = 20$ (^{29}F) instead of $N = 22$. It was mentioned in Ref. [40] that if the neutron $1p_{3/2}$ single-particle level was lowered by 350 keV then both ^{29}F and ^{31}F become bound.

2.2 New Magic Number $N = 16$

An interesting phenomenon that has recently been suggested in the neutron-rich oxygen isotopes, and may have implications on the location of the oxygen drip line, is the appearance of a new magic number in the neutron shells at $N = 16$ because of an increased energy gap between the $\nu 1s_{1/2}$ and $\nu 0d_{3/2}$ orbitals. This may impact the location of the neutron drip

line as it may suggest a $\nu 0d_{3/2}$ orbital that is high in energy, and hence, unbound. The first experimental evidence for this new shell gap came from the investigation of the neutron separation energies (S_n), the amount of energy needed to remove the outer most neutron from a nucleus, as a function of isospin $T_z = \frac{N-Z}{Z}$ [8]. The S_n systematics as a function of neutron number for nuclei with low isospin ($T_z < 3$), and therefore near stability in the $p-sd$ and sd shell regions, show sudden drops in energy following a magic number, i.e. $N = 8$ and 20. This experimental observable is shown in Fig. 2.4 where in (a) all of the measured S_n values for nuclei with odd N and even Z are plotted and in (b) where S_n is plotted for nuclei with both N and Z odd. The upward arrows guide the eye for the "traditional" magic numbers that are present near stability and can be seen in both (a) and (b) that for low isospin (T_z) the breaks in energy are present. As the isospin is increased toward more neutron-rich nuclei ($T_z \geq 3$) the "traditional" magic numbers begin to fade away; however, a new break appears at neutron number 16. The downward arrow in Fig. 2.4 guides the eye for this new gap for high isospin.

Further indirect empirical evidence for a new shell closure at $N = 16$ comes from the absence of an observed bound excited state in both ^{23}O and ^{24}O. These states were studied using a Barium Fluoride (BaF_2) detector array to collect the γ rays produced by the fragmentation of a ^{36}S beam on a Be target [9]. No evidence for any γ-decaying state from either of the two neutron-rich oxygen isotopes was found. The spectrum showing the lack of a bound excited state in ^{24}O is presented in Fig. 2.5. In particular, the lack of a bound excited state in ^{24}O determined that the first excited state must lie above the neutron threshold, which from a recent mass measurement puts that level above 4.09(10) MeV [24]. With this first excited state most likely being the 2^+ state, a lower limit is established for its excitation energy at 4.1 MeV. This energy is relatively high as compared to the 2^+ state in ^{22}O (3.19 MeV) [41, 42], believed to have a sub-shell closure at $N = 14$.

2.3 Shifting Shells

To understand the appearance of a new shell gap at $N = 16$ the underlying single-particle structure of the oxygen isotopes must be investigated. Oxygen with $Z = 8$ protons, fills the first three lowest single-particle orbitals ($0s_{1/2}0p_{3/2}0p_{1/2}$). The next single-particle ($0d_{5/2}$) level is much higher in energy and therefore creates a gap at $Z = 8$. The gap between shells

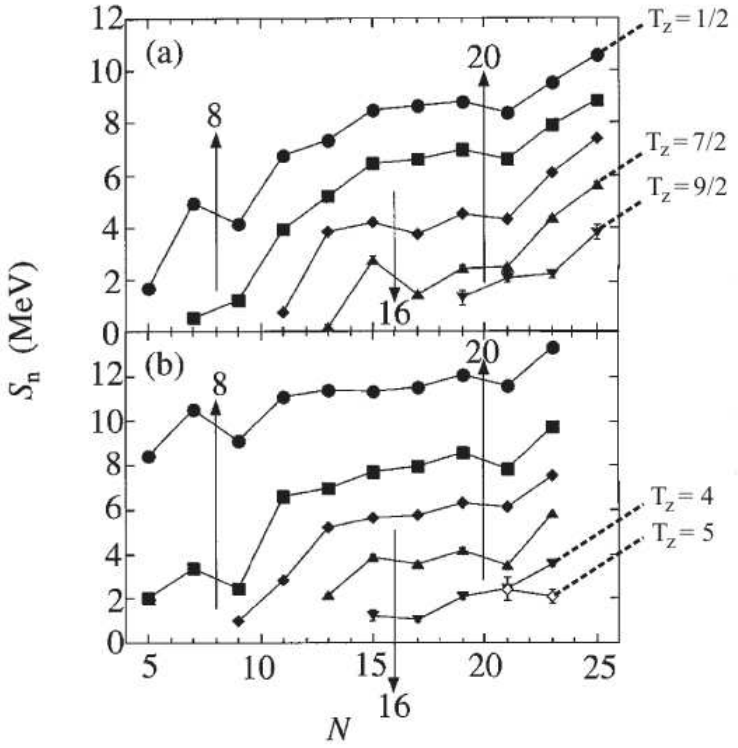

Figure 2.4: S_n values as a function of neutron number for (a) nuclei with odd N and in (b) where nuclei with both N and Z odd are both plotted. The symbols correlate to different isospin (T_z) values from 1/2 to 9/2 in (a) and 0 to 5 in (b). The arrows are there to guide the eye to the breaks in the S_n values for magic numbers. The tradition numbers for $N = 8$ and 20 are shown for low isospin with a new magic number at $N = 16$ appearing for $T_Z > 3$. [8]

creates the appearance of the magic number $Z = 8$ for the protons. Since this proton shell gap is relatively strong, it is possible to investigate the neutron shell structure independent of the effects of the protons, across the oxygen isotopes.

The oxygen isotopes may be investigated by their predicted effective (spherical) single-particle energies (ESPEs) which are shown for a number of different interactions in Fig. 2.6. The ESPEs represent the overall mean effects from all other nucleons on a single nucleon in a specific orbital. Therefore, the energies of these single-particle orbitals show the locations of shell gaps and the magic numbers. Fig. 2.6 shows the evolution of the single-particle energies (SPEs) for $Z = 8$ as a function of neutron number. The upper left corner shows the predictions for the universal *sd* shell model interaction [13] that was described above. As

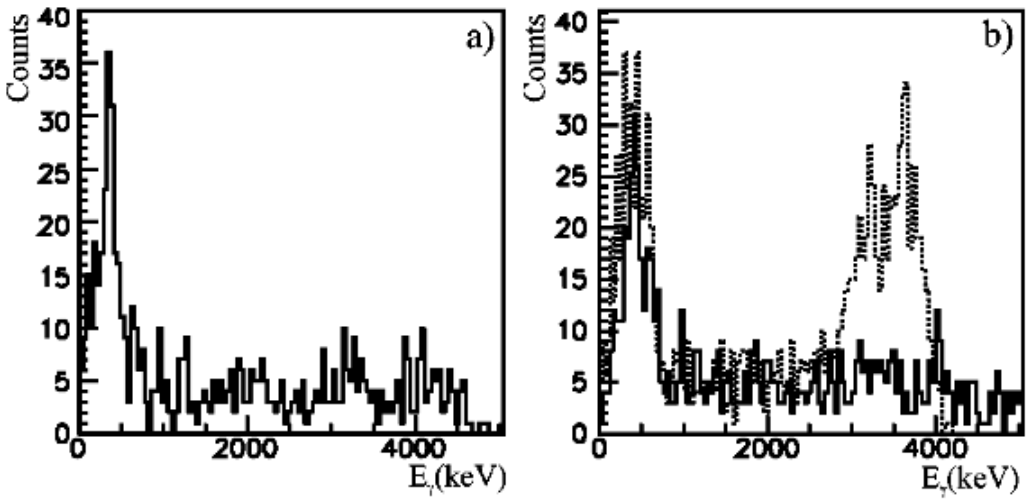

Figure 2.5: The γ-ray spectrum for ^{24}O from a BaF_2 array following the fragmentation of a ^{36}S beam on a Be target is shown in both a) and b) by the solid black line. As can be seen no clear γ-ray lines stand out against the background. To support this claim a simulated decay at an energy of 3.6 MeV is shown in b) by the dashed line [9].

can be seen, the orbitals move around in energy and therefore create relatively large gaps between different orbitals for certain neutron numbers. In particular, when neutrons fill the $0d_{5/2}$ orbital ($N = 14$) a shell gap is created between $0d_{5/2}$ and $1s_{1/2}$ creating a semi-spherical ^{22}O. This sub-shell closure has indeed been confirmed experimentally [41, 42]. Also noticed is that a filling of the $1s_{1/2}$ orbital ($N = 16$ ^{24}O) creates a new shell gap as the $0d_{3/2}$ orbital sits much higher in energy. Therefore, the appearance of a new magic number at $N = 16$ could be understood by the evolution of these single-particle levels.

The appearance of new shell gaps in the oxygen isotopes is also apparent when the SDPF-M interaction is used to calculate the single-particle energies [11]. Fig 2.7 shows the oxygen orbitals as a function of neutron number on the left, while the right side of the figure shows the orbitals for neutron number 20 as a function of proton number. Again, clearly visible is the sub-shell closure at $N = 14$ (^{22}O) and the appearance of a large shell gap at $N = 16$ for $Z = 8$ (^{24}O). Furthermore, the right side of Fig. 2.7 shows the strong proton dependence that the single-particle energies (SPEs) have. As proton number is increased from $Z = 8$ to $Z = 20$, the $N = 16$ shell gap dissolves and the traditional gap at $N = 20$ reappears between the $\nu 0d_{3/2}$ orbital and the fp shell orbitals. It should be noted that the appearance of the

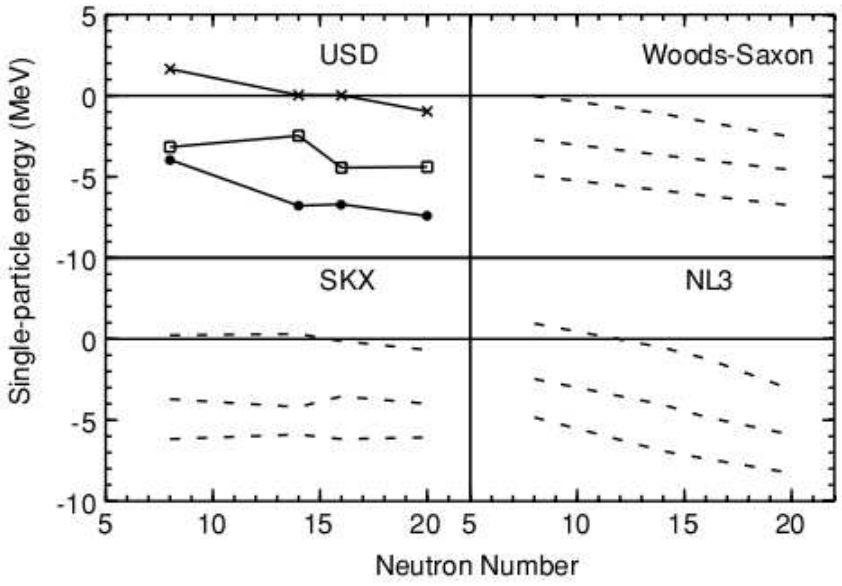

Figure 2.6: The single-particle energies (SPEs) for $Z = 8$ as a function of neutron number from four different calculations. The phenomenological USD effective interaction, a standard Woods-Saxon potential, Skyrme Hartree-Fock potential and the NL3 relativistic potential. The orbitals go from bottom to top for all calculations as the $\nu 0d_{5/2}$, $\nu 1s_{1/2}$, and the $\nu 0d_{3/2}$ [10].

$N = 16$ shell closure is directly related to the reduction in the $N = 20$ shell gap for the lower Z values, i.e. $Z < 13$.

A specific case that highlights the shell evolution and appearance of the $N = 16$ shell gap is shown in the top of Fig. 2.8 where the ESPEs for ^{30}Si and ^{24}O are plotted. Each of these nuclei has $N = 16$ but far different Z, ^{30}Si has $Z = 14$ and ^{24}O has $Z = 8$. The effects of the added protons in the $0d_{5/2}$ for $Z = 14$ are obvious as the $N = 16$ shell gap is not apparent for ^{30}Si. Hence, the energy of the $\nu 0d_{3/2}$ orbital can be greatly influenced by the number of protons present.

The underlying nature of the $N = 16$ shell gap is the energy separation of the $\nu 1s_{1/2}$ orbital and the $\nu 0d_{3/2}$ orbital. These single particle levels must become separated through some interaction to create a shell gap between them. One proposed mechanism for the strong evolution of these SPEs is the nucleon-nucleon (NN) tensor force, in particular the spin-isospin component of this force [43, 12]. The NN interaction shown in the middle of

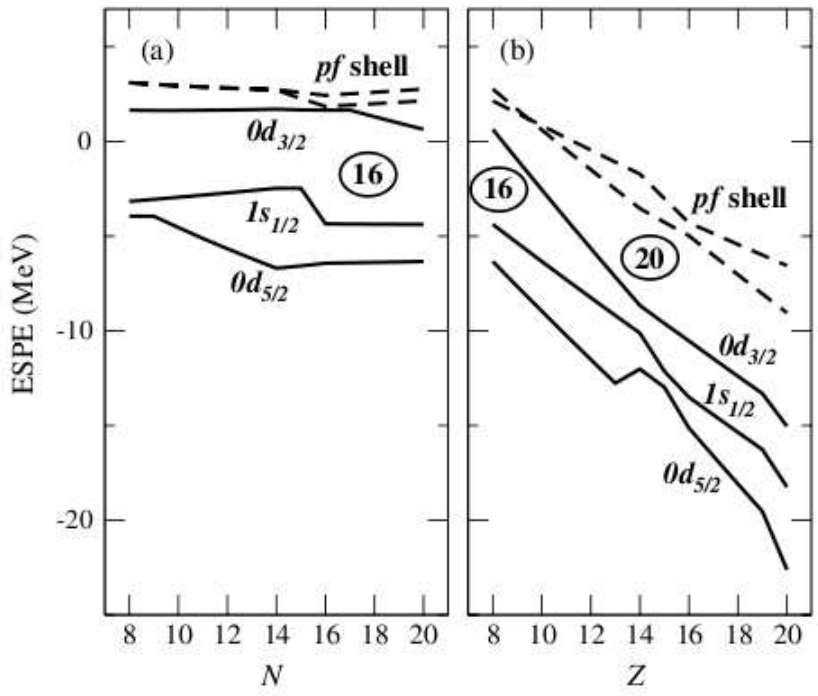

Figure 2.7: Calculated effective single-particle energies (ESPEs) from the SDPF-M interaction [11] for constant $Z = 8$ in (a) and constant $N = 20$ in (b). Note the location of the $\nu 0d_{3/2}$ orbital for $Z = 8$, and the appearance of the new shell gaps for $N = 14$ and $N = 16$ [12].

Fig. 2.8 is written as

$$V_{\tau\sigma} = \tau \cdot \tau\sigma \cdot \sigma f_{\tau\sigma}(r) \tag{2.1}$$

with "$\cdot$" denoting the scalar product between the isospin (τ) and spin (σ) operators. $f_{\tau\sigma}(r)$ is a general function of the interaction distance r. If we assume a relatively featureless function of r then $V_{\tau\sigma}$ produces a strong attraction between a spin- and isospin-flip pair of orbitals ($j_> = l + 1/2 - j_< = l - 1/2$ and proton-neutron). The strong interaction is described in figures in the bottom of Fig. 2.8 where the spin- and isospin-flips are favored at the vertices [12].

This force creates a strongly attractive feature for protons and neutrons in the spin flipped orbitals, i.e. $j_> = l + 1/2$ and $j_< = l - 1/2$. In this specific case, the angular momentum is $l = 2$ for the d orbitals hence, the $\nu 0d_{5/2}$ and $\nu 0d_{3/2}$ orbitals. As protons are added to the $0d_{5/2}$ orbital they start to interact strongly with the neutrons that occupy the $0d_{3/2}$ orbital

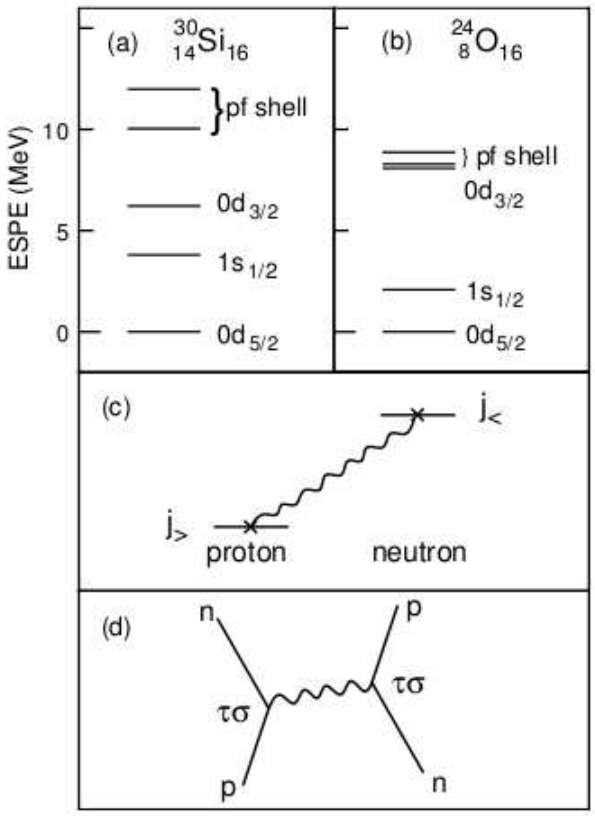

Figure 2.8: The top portion of the figure shows ESPEs for ^{30}Si and ^{24}O both having $N = 16$, but only ^{24}O having a large shell gap at $N = 16$. The middle section shows the attractive nature of the tensor force between spin partners, i.e. the protons in the $0d_{5/2}$ orbital and neutrons in the $0d_{3/2}$ orbital. The bottom portion shows the process for the spin-isospin flip interaction.

pulling it down. However, for the oxygen isotopes there are no protons in the $j_> = 0d_{5/2}$ orbital, so the attraction is missing, allowing the $0d_{3/2}$ orbital to remain high in energy and hence creating the new $N = 16$ shell gap for $Z = 8$.

Furthermore, just how high in energy the $0d_{3/2}$ orbital sits is very important to understanding the oxygen drip line. It can be noticed that the ESPE of the $0d_{3/2}$ orbital in the predictions using the USD interaction is negative for $N = 18$ (Fig. 2.6). When two neutrons are added to this orbital, as is the case for ^{26}O ($N = 18$), the ground state is understandably bound by $\sim$1 MeV [13]. This disagrees with the experimental result that ^{26}O has an unbound ground state as mentioned above. However, for the calculations of the SDPF-M interaction, as seen in Fig. 2.7 the $0d_{3/2}$ orbital is positive and therefore may

result in an unbound ^{26}O ground state. Indeed the SDPF-M interaction does predict an unbound ^{26}O ground state consistent with experimental measurements [11]. Also, the new USD05 interactions both predict an unbound ^{26}O ground state by nearly 500 keV [27]. This result came out of the fit to the data for the USD05 interactions and the main reason was that the $\nu 0d_{3/2}$ orbital was found to be raised by 500 keV as compared to the original USD interaction.

The energy of the $\nu 0d_{3/2}$ orbital is very crucial to understanding the oxygen drip line and its discrepancy with the fluorine drip line. By investigating the ground state of the $N = 17$ ^{25}O nucleus, the first determination of the location of the $0d_{3/2}$ neutron orbital can be made beyond the oxygen drip line. Furthermore, the location of the first excited states in ^{24}O also gives an indication of the size of the energy gap between the $1s_{1/2}$ and $0d_{3/2}$ levels, hence, providing further spectroscopic information at the oxygen drip line.

To have strong evidence of the new magic number of $N = 16$ a direct measurement of the lowest excited states in ^{24}O is needed. As was mentioned above, no bound excited states have been previously observed and therefore an investigation of the neutron resonance states is the only way to determine these levels. In particular, evidence of the lowest lying 2^+ level, which is predicted to be the first excited stated [13, 11, 27], may be observed. Then the level can be compared to other even-even isotopes to give a clear indication of its magicity.

CHAPTER 3

TECHNIQUES AND THEORY

The ground state of ^{25}O and the excited states of ^{24}O were populated by nucleon removal (knock-out) reactions from a radioactive ^{26}F beam. These states are unbound to neutron emission, and therefore, decay via the strong force on a timescale of $\sim 10^{-21}$ seconds. To reconstruct the energy of the decaying ^{25}O or ^{24}O state, the invariant mass method was used. The experimental decay spectra were fit by various line-shapes to reproduce the measured decay components. The line-shapes include; a single-level Breit-Wigner function to describe resonances, and a Gaussian or Maxwellian distribution to reproduce the non-resonance components. From this procedure, the characteristics of excited states in ^{24}O were measured along with a ground state mass measurement of ^{25}O. Theoretical comparisons of the observed resonance widths were made with single-particle estimates to confirm the validity of the fits to the data. Also, interpretation of the physical results and theoretical guidance came from a number of calculations. In particular, comparisons were made with the predictions and calculations of the many-body shell model using the USD [13], USD05 [27] and SDPF-M [11] interactions.

3.1 Reaction Mechanism: Nucleon Knock-Out

The use of nucleon knock-out reactions from fast radioactive beams has become an excellent way to study the structure of neutron-rich exotic nuclei [44]. For the population of the states in the neutron-rich oxygen isotopes of interest, a radioactive ^{26}F beam was impinged on a Be target. The 1^+ ground state [45] configuration of ^{26}F is believed to be dominated by a single proton in the $\pi 0d_{5/2}$ orbital ($Z = 9$) and 17 neutrons filling up to a single neutron in the $\nu 0d_{3/2}$ orbital. This neutron configuration is the same that has been predicted to dominate the ground state of ^{25}O [13, 27, 11]. Therefore, the removal of the valence proton

($\pi 0d_{5/2}$ proton) from ^{26}F should strongly populate the ground state of ^{25}O. The calculated spectroscopic factor between the ground states of ^{26}F and ^{25}O, using the USD interaction, is in fact 0.91 [13, 1]. The spectroscopic factor supports the strong overlap between these two states, since 1.0 would represent perfect overlap. More information on the calculation of the spectroscopic factor, and its meaning, is given below in section 3.5. Shown in Fig. 3.1, are the calculated cross sections from the removal of a proton from ^{26}F from the USD shell model interaction [13]. The removal of a $\pi 0d_{5/2}$ proton is shown to have a strong direct population to the ^{25}O ground state as mentioned above. The measured cross sections for only the bound ground states of the oxygen isotopes are also shown in Fig. 3.1 [14]. The cross section measurements came from the identifications of the ground states of the various oxygen isotopes following proton knock-out from the fluorine beams. The identifications of the oxygen isotopes are shown in Fig. 3.2.

Also shown in Fig. 3.1, is a relatively large cross section ($\sigma_{calc} = 25$ mb) for the population of high energy states (> 5 MeV) from the removal of a proton from the p–shell, i.e. $\pi 0p_{3/2}$ or $\pi 0p_{1/2}$ orbitals. The large cross section suggests that a large number of continuum states may be populated from the same reaction. The high energy continuum states, inparticular those of ^{25}O, may cascade by neutron emission into the low lying excited states of ^{24}O. Hence, the low lying neutron unbound excited state in ^{24}O could be measured in the same manner as the ground state decay of ^{25}O, i.e. ground state fragment plus coincidence neutron. This type of selective population was previously identified in a ^{26}Ne knock-out reaction on a Be target. In their work, only a weak population of the low lying excited states in ^{24}O were observed, and instead, the first excited state in ^{23}O was populated prominently [46].

Another possible avenue for the population of the excited states in ^{24}O, would be from a direct proton-neutron knock-out from the ^{26}F beam. If each valence nucleon (proton from the $\pi 0d_{5/2}$ orbital and a neutron from the $\nu 0d_{3/2}$ orbital) were to be removed, the resulting ^{24}O would sit in its bound ground state. Therefore, there would be no neutron decay, and it would not be observed in the present experiment. In order to populate the excited states in ^{24}O, the valence proton, plus a neutron below the occupied $\nu 0d_{3/2}$ orbital, would both have to be knocked-out. This process has a very small probability relative to a single nucleon removal reaction.

Proof that the nucleon removal reaction from ^{26}F populates at minimum the ground states of the bound neutron-rich oxygen isotopes, is shown in the bottom Fig. 3.2. Here, the

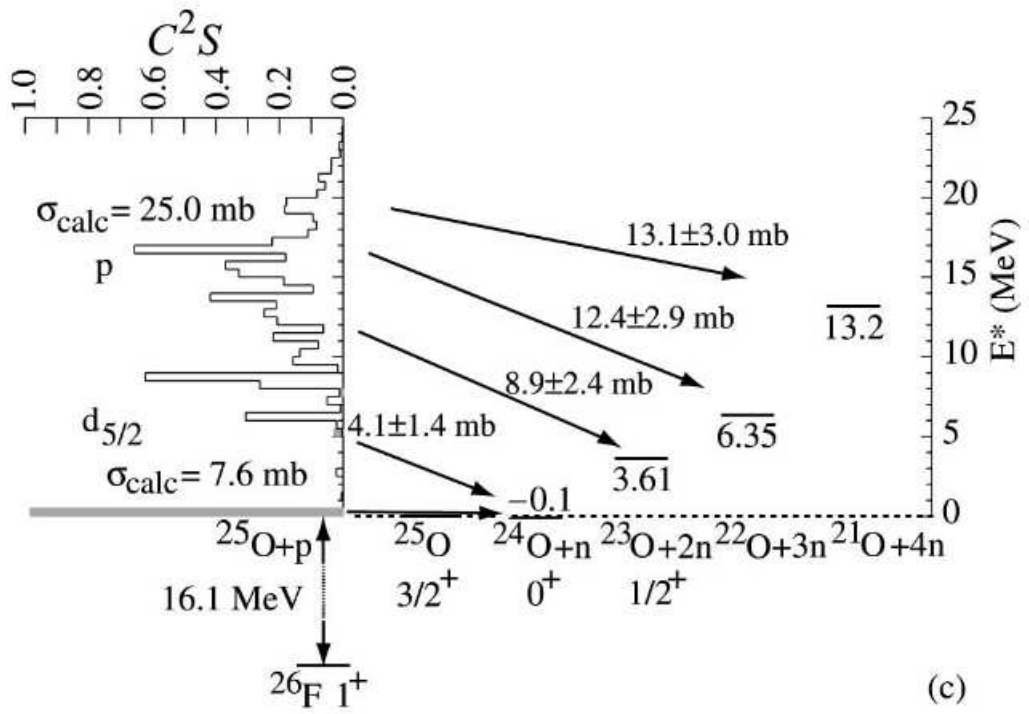

Figure 3.1: The calculated spectroscopic factors and cross sections from the USD [13] shell model interaction, are shown on the left side of the figure for the proton removal reaction of ^{26}F on a Be target [14]. The observed cross sections to the bound ground states of the oxygen isotopes for the same reaction are also shown by the arrows to their respective ground states.

clear identification of the $^{24-21}$O ground states, and their measured cross sections, from the proton knock-out of the fluorine beams, provides support for such a mechanism to populate excited states in this region. Also apparent from the measured data of Fig. 3.2, is only a very small amount of charge exchange cross section from the ^{24}F beam to the ground state of ^{24}O (top of Fig. 3.1). The lack of population of ^{24}O, provides support that the charge exchange reaction from ^{26}F to ^{26}O→^{24}O+n+n, should not be a strong contributor to the total reaction cross section of ^{24}O+n data.

3.2 Invariant Mass Method of Reconstruction

The invariant mass method is a well established technique used to reconstruct the rest mass of a resonance decay that has multiple final state fragments. The neutron decays of the ground

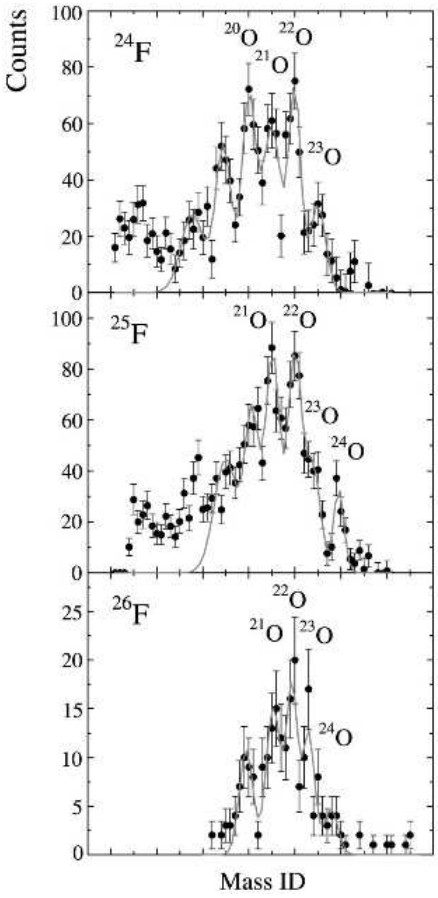

Figure 3.2: The distribution of the measured oxygen isotopes from the proton knock-out reactions from ^{24}F (top), ^{25}F (middle), and ^{26}F (bottom) are shown. From these values, the observed cross sections of Fig. 3.1 were determined. Furthermore, the lack of a strong population of ^{24}O in the knock-out reaction from ^{24}F, shows the weakness of the charge-exchange reaction channel [14].

state of ^{25}O and the excited states in ^{24}O, are mediated through the strong force. A decay of this nature is on the timescale of zeptoseconds (10^{-21} seconds). Therefore, these states may be reconstructed using the invariant mass method. The formulation of the invariant mass is given below for a two–body neutron decay. It should be noted that the speed of light has been set to equal 1 ($c = 1$) unless otherwise specified.

The four-vector representations for the total energies and momenta of the original state,

and each of its decay components, are given by

$$P_i^\mu = (E_i, \vec{P}_i), \tag{3.1}$$

$$P_f^\mu = (E_f, \vec{P}_f), \tag{3.2}$$

$$P_n^\mu = (E_n, \vec{P}_n). \tag{3.3}$$

The initial state is represented by i, f represents the fragment, and n is the label for the neutron. The decay process of the initial state into the two final products can then be written as

$$P_i^\mu = P_f^\mu + P_n^\mu. \tag{3.4}$$

The four-vectors are invariant to a Lorentz transformation. Taking the square of the left side of equation 3.4 results in a constant value. The square of both sides of equation 3.4 reveals

$$s = (P_i^\mu)^2 = (P_f^\mu + P_n^\mu)^2 = M_i^2 = M_f^2 + M_n^2 + 2(E_f E_n - P_f P_n cos\theta), \tag{3.5}$$

where s is the constant invariant value. The rest mass of the initial state M_i, is related to the rest masses of the final products (M_f, M_n), and the kinetic properties in the laboratory frame. The E's are their total energies, the P's are the momentum, and θ gives the angle between the fragment and the neutron in the laboratory frame. The rest mass of the reconstructed decay is simply the square–root of the invariant quantity, expressed as

$$M_i = \sqrt{s} = \sqrt{M_f^2 + M_n^2 + 2(E_f E_n - P_f P_n cos\theta)}. \tag{3.6}$$

Finally, the decay energy of the state may also be calculated by simply removing the rest masses of the decay products,

$$E^* = \sqrt{s} - M_f - M_n. \tag{3.7}$$

What is made clear by this procedure is that in order to complete the reconstruction of the initial state via the invariant mass, the complete four-vectors are needed for the decay products. This means a full kinematic measurement of both the outgoing fragment and neutron. Once these values have been determined, the decay energy may be easily found using the expressions presented above.

3.3 Decay Spectrum Line-Shapes

To extract information from the reconstructed invariant mass spectra for ^{23}O and ^{24}O fragments that have been found to be in coincidence with a neutron, the specific features of the spectra must be reproduced properly. There are two main components that contribute to the resonance spectrum. The resonance features of the state may be described by the single-level energy dependent Breit-Wigner line-shape. The non-resonance features contributing to the decay spectrum may be represented by either a Maxwellian distribution of beam velocity neutrons or a Gaussian distribution. The functional forms of these line-shapes are given below.

3.3.1 Resonance: Single-Level Breit-Wigner Line-Shape

The resonances observed in this work follow the decay process $A \rightarrow b + c$, where one of the decay products is a neutron. A resonance of this nature may be thought of in terms of a neutron with variable energy being scattered from the fragment nucleus. The cross section that would be measured in such a thought experiment may be well described by the R-matrix theory [47]. In particular, independent isolated resonance states in this cross section may be described by a single-level Breit-Wigner cross section distribution [48]. Although, in the present measurement, a cross section is not measured in absolute terms, the Breit-Wigner line-shape shall describe the resonance features that appeared in the data. The full energy-dependent Breit-Wigner line-shape that has been adopted to describe the resonance features of the experimental data may be expressed as

$$\sigma_l(E) \propto \frac{\Gamma_l(E)}{(E_{\text{decay}} + \Delta_l(E) - E)^2 + \frac{1}{4}\Gamma_l(E)^2}. \tag{3.8}$$

E is the relative energy between the fragment and the neutron, and E_{decay} is the resonance energy of the isolated state (when $\Delta_l(E_{\text{decay}}) = 0$). It should be noted that the phase factor is not needed here as only the decay channel has been observed in the reaction. The partial width of the state is given by $\Gamma_l(E)$. Since only the outgoing decay channel of the resonance was observed, and there is only a single decay channel via a neutron, the partial width in this work is also the total width (just deemed the width). The width $\Gamma_l(E)$ has both energy and orbital angular momentum dependence as

$$\Gamma_l(E) = 2P_l(E)\gamma^2. \tag{3.9}$$

The γ^2 is the reduced width squared and contains the wave function information of the states. $P_l(E)$ is the penetrability function, which is related to the spherical Bessel functions. The shift factor ($\Delta_l(E)$) also holds energy and orbital angular momentum dependence by

$$\Delta_l(E) = -(S_l(E) - B)\gamma^2. \tag{3.10}$$

The $S_l(E)$ is the shift function and is also related to the spherical Bessel functions and their derivatives. B is a boundary condition that must be set. A further description of each of these values and functions mentioned is presented below.

The single-level Breit-Wigner distribution may be derived from the R-Matrix theory, as done by Lane and Thomas in Ref. [47]. Although a complete derivation of the R-matrix analysis is beyond this work, the major points of the theory pertaining to the Breit-Wigner expression are highlighted below.

R-matrix theory is developed out of the solution for the nuclear wave functions at a boundary. The boundary condition represents the minimum distance that the two nuclei may come together without feeling a nuclear force from the other. This boundary condition is determined by the so called interaction or channel radius given as

$$a = r_\circ(A_1^{1/3} + A_2^{1/3}), \tag{3.11}$$

where typically $r_\circ = 1.4 - 1.5$ fm. Therefore, this radius is slightly larger than the size of the two nuclei, i.e. $r_\circ \approx 1.2$ fm.

The general Schrödinger equation for the radial wave functions, including the orbital angular momentum l, and the Coulomb potential V for the external region, is given by

$$\left[\frac{d}{dr^2} - \frac{l(l+1)}{r^2} - \frac{2M}{\hbar^2}(V - E)\right] u_l(r) = 0. \tag{3.12}$$

$V = 0$ in this instance as the Coulomb interaction is non-existent in the case of neutron decay. The general solutions of this equation come in two forms; either as incoming and outgoing waves (I_l, O_l), or as the regular and irregular solutions (F_l, G_l). The two forms of the solution are related by

$$\begin{aligned} I_l &= (G_l - iF_l), \\ O_l &= (G_l + iF_l). \end{aligned} \tag{3.13}$$

The incoming and outgoing waves are related to the Hankel functions according to

$$\begin{aligned} I_l &= -i(\pi\rho/2)^{1/2} H^{(2)}_{l+1/2}(\rho), \\ O_l &= i(\pi\rho/2)^{1/2} H^{(1)}_{l+1/2}(\rho); \end{aligned} \tag{3.14}$$

and the F and G functions may be related to the J-type Bessel functions by

$$\begin{aligned} F_l &= \pi\rho/2)^{1/2} J_{l+1/2}(\rho), \\ G_l &= (-1)^l (\pi\rho/2)^{1/2} J_{-(l+1/2)}(\rho). \end{aligned} \tag{3.15}$$

In each case $\rho = ka$, where a is the interaction radius (eq. 3.11). $k^2 = \frac{2ME}{\hbar^2}$, with M being the reduced mass of the system and E the relative energy between the particles.

In the external region the logarithmic derivative of the wave function is needed to determine the cross section. Therefore, the expression for the wave function's logarithmic derivative is given by

$$L_l = (\frac{\rho O_l^{'}}{O_l})_{r=a} = S_l + iP_l. \tag{3.16}$$

The S_l and P_l are the shift and penetrability functions mentioned above. These are explicitly expressed in terms of the F and G functions by

$$\begin{aligned} S &= \left[\rho(F_l F_l^{'} + G_l G_l^{'})/(F_l^2 + G_l^2)\right]_{r=a}, \\ P &= \left[\rho/(F_l^2 + G_l^2)\right]_{r=a}. \end{aligned} \tag{3.17}$$

The physical R-matrix is determined from the manipulation of the Schrödinger equation for the radial part of the wave function (eq. 3.12) for a particle at two energies. Using an application of the Green's theorem relation, the R-matrix, which relates the internal wave function to its derivative on the surface may be given by

$$R = \frac{\hbar^2}{2Ma} \sum_{\text{decay}} \frac{|u_l(a)|^2}{E_{\text{decay}} - E} = \sum \frac{\gamma^2}{E_{\text{decay}} - E}. \tag{3.18}$$

γ is the same reduced width as mentioned above, and here we see it represents the wave function at the boundary condition $r = a$,

$$\gamma = (\hbar^2/2Ma)^{1/2} u_l(a). \tag{3.19}$$

The relation of the R-matrix to the collision matrix U, needed to calculate the cross section, may be found by equating the logarithmic derivatives from the two regions at the boundary ($r = a$). The relation of U to the R-matrix and to L is

$$U_l = \frac{I_l}{O_l} \frac{1 - L_l^* R_l}{1 - L_l R_l} = e^{2i\delta_l}. \tag{3.20}$$

U may be expressed in terms of the phase shift δ because the R-matrix has real values. It should be noted that L_l^* represents the complex conjugate of the function L.

Each E_{decay} in equation 3.18 represents an eigenvalue identifier for a specific resonance energy. If one assumes that only a single resonance dominates the spectrum, the summation may be dropped. When this is carried out

$$R = \frac{\gamma^2}{E_{\text{decay}} - E}; \tag{3.21}$$

and the one-level approximation for the phase shift becomes

$$\delta_l(E) = tan^{-1}\left(\frac{\frac{1}{2}\Gamma_l(E)}{E_{\text{decay}} + \Delta_l(E) - E}\right) - \phi_l. \tag{3.22}$$

ϕ_l is the hard sphere scatter phase shift. The width $\Gamma_l(E)$ is the same as equation 3.9 and $\Delta_l(E)$ is the shift factor of equation 3.10. The resonance contribution to the collision matrix in the one-level approximation (eq. 3.21) is then

$$U_l = \frac{i\Gamma_{l_1}^{1/2}(E)\Gamma_{l_2}^{1/2}(E)}{E_{\text{decay}} + \Delta_l(E) - E - \frac{i}{2}\Gamma_l(E)}, \tag{3.23}$$

where the $\Gamma_{l_1}(E)$ and the $\Gamma_{l_2}(E)$ are the partial widths of the incoming and outgoing resonances. Again, for this measurement, only the decay channel has been experimentally observed and the incoming width will be removed from the final cross section expression. Inserting equation 3.23 into the cross section equation related the U collision matrix,

$$\sigma_l = \int \sigma(\theta) d\Omega = \pi k^{-2} \sum_l (2l+1)|1 - U_l|^2; \tag{3.24}$$

results in the original Breit-Wigner single-level equation

$$\sigma = \frac{\pi}{k^2} g_j \frac{\Gamma_{l_1}(E)\Gamma_{l_2}(E)}{(E_{\text{decay}} + \Delta_l(E) - E)^2 + \frac{1}{4}\Gamma_l(E)^2}. \tag{3.25}$$

The g_j is statistical factor given by

$$g_j = \frac{2J+1}{(2I_{l_1}+1)(2I_{l_2}+1)}, \tag{3.26}$$

with J being the total spin of the state, and I representing the momenta of the incoming and outgoing channels.

This result for the single-level Breit-Wigner equation (eq. 3.25) describes the observable cross-section when moving through a single resonance at energy E_{decay} and spin J. This is the final equation used to describe the resonance features of this work with some small

modifications. The first change is the removal of the incoming resonance width. The second change is allowing for the amplitude of the line-shape to vary. Hence, the phase and statistical factors out front of the cross section expression are absorbed into the amplitude parameter. The final Breit-Wigner line-shape adopted was given above in equation 3.8. The parameters of the Breit-Wigner fit must then include the resonance energy E_{decay}, the energy dependent width $\Gamma_l(E)$ via the reduced width γ^2, the orbital angular momentum l, and the overall amplitude.

The choice for the boundary conditions (the channel radius a, and inside the shift factor B), were determined based on standard values. The expression for a (eq. 3.11) was used to set the boundary point for the matching of the wave functions based on the fragments involved. A_1 was equal to either $A = 23$ or 24, depending if the state was from ^{24}O or ^{25}O. $A_2 = 1$ in both cases as it represented the neutron. The B value was set so that at the resonance energy, $\Delta_l(E_{\text{decay}}) = 0$. Therefore, B was made to equal the shift function at the resonance energy, $S_l(E_{\text{decay}})$. This was chosen so that the observed resonance energy would not lie outside of the resonance width.

Finally, it should be made clear that the inclusion of both the energy dependence of the width Γ, and the shift factor Δ, were both important to the final line-shape in the decay distribution. Hence, this has important effects when comparing with the experimental data. Shown in figure 3.3 are Breit-Wigner line-shapes that include all energy dependence components (red line), a lack of a shift factor but energy dependent width (green line), lack of energy dependence in the width and no shift factor (blue line), and a lack of an energy of the width but inclusion of a shift factor (purple line). What is clearly noticed is the strong variations between these lines-shapes for this $l = 2$ orbital angular momentum fit. Hence, the importance of the proper line-shape is made clear. In particular, the need for the shift factor when investigating nearly pure single-particle states.

3.3.2 Non-Resonance: Gaussian and Maxwellian Distributions

To simulate the non-resonant features of the decay spectrum a Maxwellian distribution of beam velocity neutrons and a Gaussian distribution of neutrons were used as inputs into the decay spectrum line-shape. A Maxwellian distribution of beam velocity neutrons was used

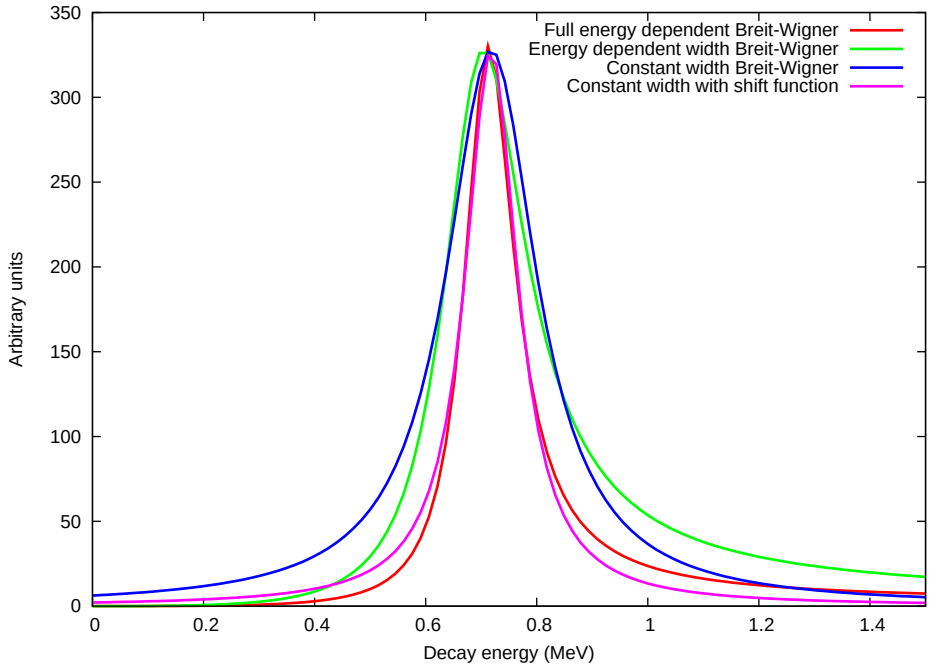

Figure 3.3: The Breit-Wigner line-shape (eq. 3.8) is plotted with an orbital angular momentum of $l = 2$, at a decay energy of $E_{\text{decay}} = 0.7$ MeV, and width of $\Gamma = 0.2$ MeV, with various components. The two components are the energy dependence of the width Γ, and the inclusion of the energy-dependent shift factor Δ. The full energy-dependent Breit-Wigner function is given by the red line, the function lacking the shift factor but including the energy dependence of the width is shown by the green line. The function with a full lack of energy dependence is shown by the blue line, and the function with no energy dependence in the width but an inclusion of the shift factor is shown by the purple line. All of the lines have been normalized to each other.

of the form

$$f_p = \left(\frac{1}{2\pi mkT}\right)^{3/2} e^{-\frac{\vec{p}^2}{2mkT}}, \tag{3.27}$$

where the thermal temperature T of the distribution was a free parameter. This temperature gives an indication of the kinetic energy, and its spread for the system. This expression given in units of energy, which is needed to compare with the decay spectrum, is

$$f_E dE = f_p \left(\frac{dp}{dE}\right) dE = 2\sqrt{\frac{E}{\pi(kT)^3}} e^{-\frac{E}{kT}} dE. \tag{3.28}$$

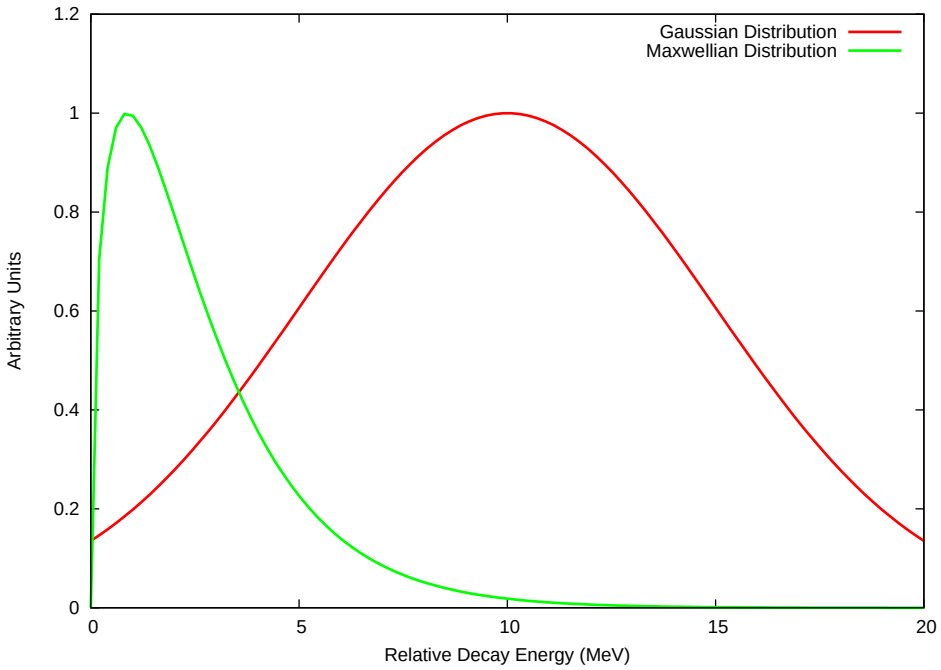

Figure 3.4: The two non-resonance input distributions, Gaussian (red line) and Maxwellian (green line), for the ST-mona [15] Monte Carlo simulation, are shown in the figure. The free parameters of each distribution have come from a best fit to the experimental ^{23}O+n coincidence data. The Gaussian distribution has $E_c = 10$ MeV, and $\sigma = 5$ MeV. The Maxwellian distribution has a thermal temperature of $T = 1.75$ MeV.

The Maxwellian line-shape that was input into the decay distribution of the ST-mona [15] Monte Carlo simulation, is shown by the green line in Fig. 3.4. The result of this distribution in the final decay spectrum is shown in Fig. 6.7 in Chapter 6 by the green line also.

The Gaussian non-resonance distribution is given by

$$f_G \propto e^{-\frac{(E-E_c)^2}{2\sigma^2}}, \tag{3.29}$$

where the centroid energy E_c, distribution width σ, and the amplitude of the distribution, are all free parameters. The distribution that was used as input for the decay distribution of the Monte Carlo simulation, and its result in the final decay distribution are shown by the red lines in Figs. 3.4 and 6.7 (chapter 6), respectively.

It should be noted, that although the two non-resonance distributions vary in their functional form, their final structures in the decay spectrum do not differ largely. Therefore, the choice of the non-resonance distribution does not drastically alter the fit to the observed

data. More discussion on this point will take place in chapter 6.

3.4 Single-Particle Width

To understand the observed width at the resonance energy ($\Gamma_l(E_{\text{decay}})$) that has been extracted from the Breit-Wigner line-shape fit, it may be compared to a width of a pure single-particle state. The pure single-particle prediction, by definition, uses only a single orbital angular momentum (l) state in the calculation. In the analysis of the resonance states of ^{24}O and ^{25}O, two single-particle calculations were used to predict single-particle widths. The first method used a simple square well potential to estimate the nuclear mean field, and therefore, predict the width of a resonance state for a neutron with a certain orbital angular momentum [49]. The second approach, used a Woods-Saxon potential as the mean potential. The parameters of the Woods-Saxon were adjusted to reproduce the energies and levels in ^{17}O and ^{17}F. The single-particle width was then calculated from the amplitude of the wave function for a resonance with particular spin J, and orbital angular momentum l.

The simplest way to determine a single-particle width is to take a spin-less neutral particle and scatter it off a spherically symmetric three-dimensional square well potential. This is an ideal procedure for the present work since we are concerned with neutrons, although they do have an intrinsic spin of 1/2. This procedure follows the same format as the previously presented R-matrix theory. The added component is an approximation of γ^2, the reduced width. The approximate value is solved for and this value is used to retrieve the total single-particle width Γ_{sp}. Starting by inputting the square well potential into the Schrödinger equation, results in

$$(\frac{d^2}{dr^2} + k^2 - \frac{l(l+1)}{r^2})u_l(r) = 0. \tag{3.30}$$

And for a radius larger than the size of the potential ($r > R$) we have

$$k^2 = \frac{2ME}{\hbar^2} \tag{3.31}$$

and,

$$u_l(r) = rR_l(r). \tag{3.32}$$

Here, $R_l(r)$ is the radial component to the wave function. The solutions to this differential equation are given in terms of the spherical Bessel and Neumann functions,

$$F_l(r) = krj_l(kr) \tag{3.33}$$

and

$$G_l(r) = krn_l(kr). \tag{3.34}$$

The general solution is then of the form

$$u_l(r) = cos\delta_l F_l(r) + sin\delta_l G_l(r) \tag{3.35}$$

with δ_l representing the phase shifts for the various orbital angular momentum. The phase shifts may be determined by the boundary conditions imposed on the wave function at the boundary $r = R$. Here, the wave function and its derivative must both be continuous. This boundary condition is expressed by the logarithmic derivative L_l,

$$L_l = R\frac{1}{u_l(R)\left(\frac{du_l}{dr}\right)_{r=R}}. \tag{3.36}$$

The value for L_l can be found when we evaluate the boundary condition for $r < R$. Setting V_0 as the constant of the potential, we have for the solution of the Schrödinger equation (eq. 3.30) for $r < R$,

$$K^2 = \frac{2ME}{\hbar^2}(E - V_0) \tag{3.37}$$

with

$$u_l \propto KRj_l(KR) \tag{3.38}$$

and,

$$L_l = 1 + KR\frac{j_l^{'}(KR)}{j_l(KR)}, \tag{3.39}$$

where the prime denotes a derivative with respect to the energy E.

A convenient form for the expression of the phase shift may be given by

$$\exp 2i\delta_l = \frac{L_l - \Delta_l + iP_l}{L_l - \Delta_l - iP_l}\exp 2i\xi_l. \tag{3.40}$$

Δ_l is given by

$$\Delta_l = \frac{G_l G_l^{'} + F_l F_l^{'}}{G_l^2 + F_l^2} \tag{3.41}$$

and P_l reflects the penetrability through the barrier and is expressed as

$$P_l = \frac{G_l G_l^{'} - F_l F_l^{'}}{G_l^2 + F_l^2} = kRv_l(kR) \tag{3.42}$$

with $v_l(kR)$ representing the ratio of the transmission at $r = R$ to $r = \infty$. Finally, the expression for ξ_l relates the phase shift from the scatter off a solid sphere. It is related to the Bessel and Neumann functions by

$$\exp 2i\xi_l = \frac{G_l - iF_l}{G_l + iF_l}. \tag{3.43}$$

Assuming a resonance feature, which may appear if the lifetime of the state is long compared to the time it takes for the particle to traverse the size of the nucleus, we then have $s_l \ll 1$ and $\xi_l \ll 1$. The phase shift will be small everywhere except around the resonance energy E_{decay} and so

$$L_l(E_{\text{decay}}) - \Delta_l(E_{\text{decay}}) = 0. \tag{3.44}$$

Expansion of this expression around the resonance energy leads, to first order, to

$$L_l(E) - \Delta_l(E) = -\frac{1}{\gamma}(E - E_r), \tag{3.45}$$

with the reduced width γ, equaling

$$\gamma^{-1} = -\left(\frac{\partial L_l(E)}{\partial E}\right)_{E=E_{\text{decay}}} + \left(\frac{\partial \Delta_l(E)}{\partial E}\right)_{E=E_{\text{decay}}}. \tag{3.46}$$

As was the case with the Breit-Wigner single-level equation (eq. 3.8), the observed width $\Gamma_l(E)$, is related to the reduced width by $\Gamma_l(E) = 2P_l(E)\gamma^2$. Therefore, to calculate the single-particle prediction for the observed width, the value of γ must be evaluated. From the solutions of the Schrödinger equation we have

$$\left(\frac{\partial L_l(E)}{\partial E}\right)_{E=E_{\text{decay}}} \approx -\frac{MR^2}{\hbar^2} \tag{3.47}$$

for $kR < l^{1/2}$ and

$$\left(\frac{\partial \Delta_l(E)}{\partial E}\right)_{E=E_{\text{decay}}} \approx \frac{MR^2}{\hbar^2}\frac{2}{2l-1} \tag{3.48}$$

for $l > 0$ and $kR < l^{1/2}$, while zero for $l = 0$. Inserting these into eq. 3.46, we get the resulting single-particle predictions from a spherical square well potential

$$\Gamma_{sp} = \begin{cases} \frac{2\hbar^2}{MR^2} kR v_l(kR) \frac{2l-1}{2l+1} & l > 0, kR < l^{1/2} \\ \\ \frac{2\hbar^2}{MR^2} kR & l = 0 \end{cases} \tag{3.49}$$

The second method to calculate the single-particle width for a resonance state used a Woods-Saxon potential to describe the mean effects of the nucleons on a single nucleon. The Woods-Saxon potential is given by

$$V(r) = \frac{V_\circ}{1 + exp(\frac{r-R}{a})}. \tag{3.50}$$

Also included into the potential was the strong-spin orbit contribution, related to the Woods-Saxon potential $V(r)$ by

$$V_{so}(r) \propto -\frac{1}{r}\frac{dV(r)}{dr}\vec{l}\cdot\vec{s}. \tag{3.51}$$

$V_\circ, V_{so}, R$ and a are the overall strength, spin-orbit strength, radius, and diffuseness parameters, respectively. These parameters were set by matching the single-particle energies and widths of the ground and single-particle states of ^{17}O. These states are the $5/2^+, 1/2^+$ and $3/2^+$ states of ^{17}O. To calculate these states the Schrödinger equation was solved for this potential for a specific spin and orbital angular momentum. The wave function from this state can then be calculated at a specific radius. The amplitude squared of the wave function may also be calculated at this particular distance and for the same conditions but with a different energy. From the amplitude squared of the wave function, a relative probability for the particle at a certain energy (and constant distance) may be obtained. It is the centroid of this distribution that gives the resonance energy of the state with chosen J and l values. The FWHM width of the distribution leads to the single-particle resonance width. Since these calculations are for a single-particle state, the spectroscopic factor of the state being compared must be multiplied with the single-particle width to directly compare with the experimental data. In the same sense, if a spectroscopic factor were unknown, comparison with the single-particle width would indicate the spectroscopic factor for that state.

To confirm the validity of the parameters of the potential, the calculated single-particle states in ^{17}F were reproduced. Inputting the matched parameters into Woods-Saxon potential allowed the calculation of the states in ^{24}O and ^{25}O. The potential radius was increased as $R = 1.2A^{1/3}$ fm and the reduced mass of the system was adjusted. Furthermore, the overall depth of the potential was adjusted to match the observed decay energy for each state. Therefore, a second independent prediction of the single-particle width was made possible.

3.5 Shell Model Calculations

To understand the significance of the physical results obtained for the neutron unbound states of the oxygen isotopes, they are to be compared with theoretical calculations and predictions. Furthermore, the theoretical calculations may also provide important information to guide and support the interpretation of the experimental data. The main theoretical model that has been utilized in this study is the large-scale Shell Model. A brief history of the origins of the shell model will be given below. Following this, a description of the workings of the modern shell model, and a description of the various shell model interactions that are to be used, is to be presented.

The idea that nuclei may be described by an underlying shell structure came about from a plethora of empirical evidence. The data showed that there were distinct experimental signatures for certain numbers of protons (Z) and neutrons (N). These particular nucleon numbers became known as magic numbers. Specific evidence for these magic numbers came from data that showed increased binding energies, and large numbers of stable isotopes for certain elements. Also, observed neutron and proton separation energies (the amount of energy needed to remove the outer most nucleon), showed sharp drops in energy directly after a magic number of nucleons. Neutron cross sections also revealed a lack of absorption at particular nucleon numbers, and for these same magic numbers discrepancies with the radius following the mass relation $A^{1/3}$ were found. Furthermore, some of the strongest evidence was found from the energies of the first excited states in nuclei. In particular, the 2^+ level in even-even nuclei, was a key signifier of magic or doubly magic nuclei. The energy of the first 2^+ state, if relatively high, indicated that the nucleus was spherical. This means that the energy gap to the next highest single-particle orbital must be large, and therefore, a magic number has been identified. The $B(E2)$ value for an excited state (2^+ states in particular), also indicates the collective nature of the nucleus. A relative decrease of this value for certain nucleon numbers, shows magicity. Again, this provides more evidence for the underlying shell structure in nuclei. The traditional magic numbers were experimentally deduced to lie at $N = Z = 2, 8, 20, 28, 50, 82$ and 126.

An independent particle shell model was first developed to describe the experimental data. The idea behind this model was that a single nucleon in the nucleus felt an overall mean field from all other nucleons. The single nucleon may then orbit inside the mean

field in a relatively un-hindered fashion. Therefore, the energies for these single-particle orbitals of a single nucleon may be found by assuming a single central mean potential. The central potential is spherically symmetric, and may be inserted into the time-independent Schrödinger equation (eq. 3.30). The energies and ordering of the orbitals are then calculated. The filling of the orbitals is done in a normal order, from lowest energy to highest energy, making sure that the Pauli Principle is up-held. This means no two nucleons of the same type may have the same quantum numbers. From this method, it is simple to determine where the shell gaps appear, as large energy differences between orbitals appear after the filling of a certain number of nucleons. The calculation of the orbitals from a central potential may be repeated using various potentials until a suitable one has been found which reproduces the experimental magic numbers. The nuclear potential must be predominantly strong and on a short range ($2-4$ fm), as it saturates around $A = 6-10$. A few common potentials that have been previously used, and are still widely used today, are the harmonic oscillator, the square well, and the Woods-Saxon potentials.

It has been found, that none of the aforementioned potentials (i.e. harmonic oscillator, square well, or Woods-Saxon), were able to describe the experimental magic numbers beyond $N = Z = 20$. Therefore, a crucial component to the description of the nuclear force was absent. A solution was found by introducing a strong spin–orbit force to the nuclear potential. This was done by Maria Goeppert-Mayer [50] and Johannes Hans Daniel Jensen and collaborators [51], both at the same time around 1950. The resulting spin–orbit force that was added was expressed as

$$V_{so}(r) \propto -\frac{1}{r}\frac{dV(r)}{dr}\vec{l}\cdot\vec{s}. \tag{3.52}$$

The $V(r)$ is the mean potential (i.e. harmonic oscillator), so the spin-orbit potential is proportional to the first derivative of the mean potential. The first derivative in the potential represents that this effect is strongest on the surface of the nucleus, away from where the mean potential is saturated. The addition spin–orbit force splits the previously degenerate levels having the same orbital angular momentum but different total spin J. This is due to the two different projections of the intrinsic spin value s for a single nucleon on the total spin, $J = l \pm s$. The energy splitting between levels with the same l but different J is given as

$$\Delta\epsilon_{nlj} = \frac{D}{2}\left[j(j+1) - l(l+1) - \frac{3}{4}\right]. \tag{3.53}$$

D is simply the strength of the splitting that depends on the choice of the potential. The projections of s for a given l are then

$$\begin{aligned} \Delta\epsilon_{nlj=l+1/2} &= -\frac{D}{2}\cdot l \\ \Delta\epsilon_{nlj=l-1/2} &= \frac{D}{2}(l+1). \end{aligned} \tag{3.54}$$

Therefore, the $-1/2$ projection, raises the single-particle orbital and the $+1/2$ projection lowers it, both, relative to the degenerate energy. The splitting of the single-particle orbitals causes a re-shuffling of the order of some of the levels. This is shown in Fig. 3.5, where the single-particle energy levels for ^{208}Pb are shown as calculated from a harmonic oscillator (left), a Woods-Saxon potential (middle), and a Wood-Saxon potential with the spin-orbit contribution (right). Clearly noticed is the lack of reproduction of the magic number above $N = Z = 20$ for the two potentials with out the spin-orbit part. The Woods-Saxon breaks the orbital angular momentum degeneracy of the harmonic oscillator, but is still inadequate. However, the addition of the spin-orbit potential, breaks the J degeneracy, and allows for the reproduction of all of the tradition magic numbers ($N = Z = 2, 8, 20, 28, 50, 82$ and 126). The inclusion of the strong spin-orbit splitting was vital to understanding the nuclear single-particle shell structure.

Although the independent particle model may describe certain spectroscopic information such as the magic numbers, it did a poor job of describing nuclei away from closed shells. An improvement to the independent particle model came from the inclusion of effective or correlation forces between nucleons. A Hamiltonian of this nature, for a nucleus with A nucleons may be expressed as

$$H = H_0 + H_{res}. \tag{3.55}$$

H_0 includes both the central potential U and the kinetic energy T. H_0 describes the nucleons independent of each other, and H_{res} is given by

$$H_{res} = \left(\frac{1}{2}\sum_{i,j=1}^{A} V_{i,j} - \sum_{i=1}^{A} U(r_i)\right). \tag{3.56}$$

Where here, $V_{i,j}$ are the residual interactions between two nucleons for two-body interactions only, in the central potential U. Taking two nucleons outside of a central core of nucleons described by H_0, along with the residual interaction, results in an energy shift of the bare

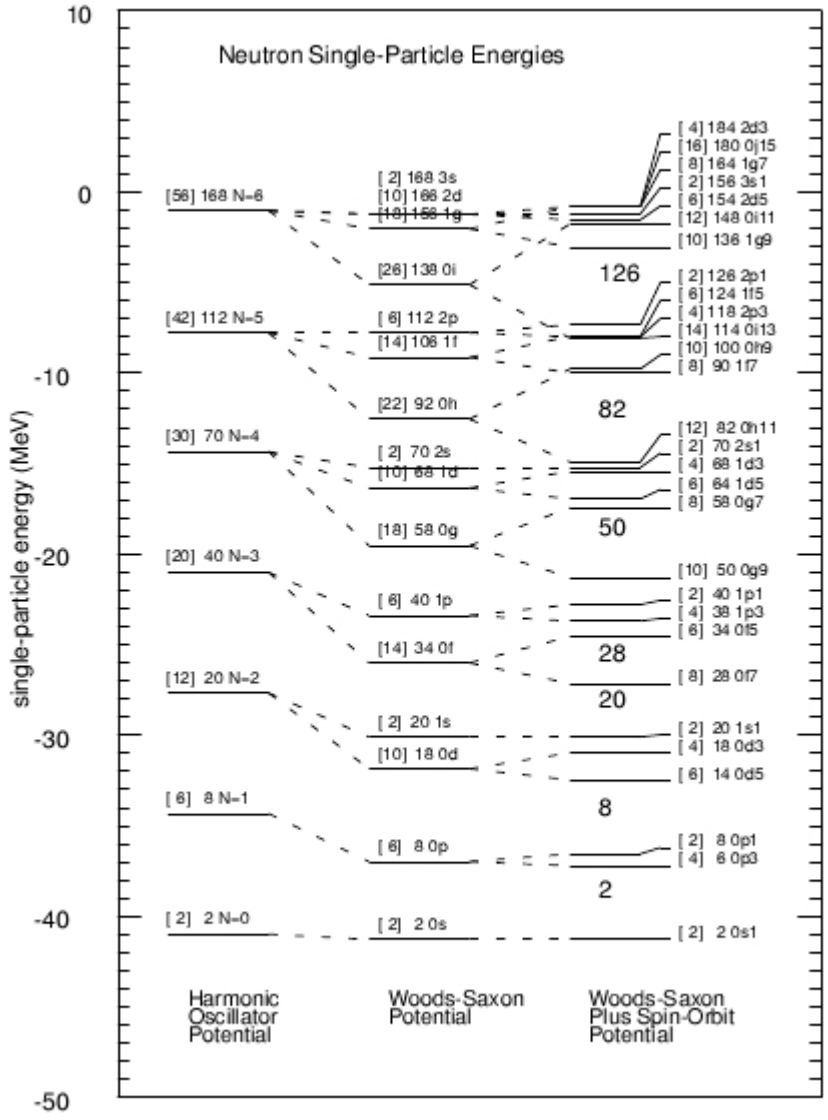

Figure 3.5: The single-particle energies are shown for ^{208}Pb using three different nuclear potentials in the Schrödinger equation, the harmonic oscillator potential (left), the Woods-Saxon potential (middle), and the Woods-Saxon potential with the spin-orbit potential included (right). The traditional magic numbers of $N = Z = 2, 8, 20, 28, 50, 82$ and 126, can only be reproduced when a strong spin-orbit force is included.

single-particle energies of

$$\Delta E(j_1 j_2; J) = \langle j_1 j_2; JM | V_{12} | j_1 j_2; JM \rangle \tag{3.57}$$

for a given total spin J and total spin projection M. Although, we see here how to calculate spectroscopic information for two nucleons outside a closed shell, in general we would like to do calculations for n nucleons outside a closed shell. Also, the inclusion of the largest number of orbitals (i.e. model space) would also be desirable. Therefore, one must move to large-scale shell model calculations which can be completed for large numbers of valence nucleons on the largest possible valence spaces. A general outline for the calculation of the energies and wave functions for a typical large-scale shell model calculation is given below. Further details may be found in Refs. [52, 53].

The first step in completing a large-scale shell model calculation is to define a valence space. The valence space is determined by which orbitals are included in the calculation. The size of the space should be small enough so that the calculation can be completed in a reasonable time, while large enough so as not to have drastic effects on the spectroscopic information being determined. For instance, in the case of the neutron rich oxygen isotopes, the *sd* shell space ($0d_{5/2}, 1s_{1/2}$ and $0d_{3/2}$ orbitals), is most often used. The choice of the *sd* model space for the oxygen isotopes is prime because the protons have a very good shell closure at $Z = 8$, and they have less than 20 neutrons. Once a model space has been determined, the number of nucleons A and the isospin T of the system must be decided. These two quantities simply define the nucleus of interest, as the isospin is related to the difference between the number of neutrons and protons in a nucleus.

Next, a complete set of basis states must be determined from the number of valence nucleons (n) and the model space. The number of valence nucleons may be found by subtraction the number of nucleons making up the closed core from the total number of nucleons. In the case of ^{25}O with $A = 25$, inside the *sd* shell model space, the number of valence nucleons (all neutrons in this case) is $n = A - 16 = 25 - 16 = 9$. There are two different methods for determining the basis states, either the m-scheme or the j-scheme. The m-scheme determines the basis states in terms of a definite magnetic quantum number M. The j-scheme is similar, only the basis states are represented in terms of definite total spin J. The m-scheme basis states do not have good J projections in general. However, since the Hamiltonian is spherically symmetric, and there is a complete set of basis states, the good

J value may be found from the total spin operator $\hat{\mathrm{J}}$ as

$$\langle \Psi_k | J^2 | \Psi_k \rangle. \tag{3.58}$$

Here, Ψ_k is the total wave function in terms of the magnetic substates m. The shell model calculations in this work use both the m-scheme [2, 1] and j-scheme [54] types of shell model calculations.

The total wave function (Ψ_k) for a single state with quantum numbers $k = |nlj\rangle$ may be described as a linear combination of its basis states by

$$|\Psi_k\rangle = \sum_{\alpha=1}^{n} a_{k\alpha} |\psi_\alpha\rangle, \tag{3.59}$$

where α defines a single-particle basis for the n number of basis state configurations, and ψ_α are the basis configurations. In the sd shell basis configurations are any combination of particles (or holes) in the $0d_{5/2}, 1s_{1/2}$ and $0d_{3/2}$ orbitals. Or, $0d_{5/2}^{n1} 1s_{1/2}^{n2} 0d_{3/2}^{n3}$, where $n1, n2$ and $n3$ may range from 0 to the total number of valence nucleons, as long as $n1{+}n2{+}n3 = n$. The $a_{k\alpha}$ are the weight coefficients that must be determined for each wave function. Inserting the total wave function into the Hamiltonian (eq. 3.55), which includes two-body interactions, we have

$$\begin{aligned} H|\Psi_k\rangle &= E_k|\Psi\rangle, \\ (H_0 + H_{res}) \sum_{\alpha=1}^{n} a_{\alpha k} |\psi_\alpha\rangle &= E_k \sum_{\alpha=1}^{n} a_{\alpha k} |\psi_\alpha\rangle, \\ \sum_{\beta=1}^{n} \langle \psi_\beta | H_0 + H_{res} | \psi_\alpha \rangle a_{\alpha k} &= E_k a_{\beta k}. \end{aligned} \tag{3.60}$$

Writing the above expression in matrix form we have,

$$\sum_{\alpha=1}^{n} H_{\beta\alpha} a_{\alpha k} = E_k a_{\beta k}, \tag{3.61}$$

with

$$H_{\beta\alpha} = E_\alpha^0 \delta_{\beta\alpha} + \langle \psi_\beta | H_{res} | \psi_\beta \rangle. \tag{3.62}$$

Or in terms of an eigenvalue problem for each eigenvalue E_k;

$$\sum_{\alpha=1}^{n} H_{\beta\alpha} a_{\alpha k} - E_k a_{\beta k} = 0, \tag{3.63}$$

and then

$$\begin{vmatrix} H_{11} - E_k & H_{12} & ...H_{1n} \\ H_{21} & H_{22} - E_k & ...H_{2n} \\ \vdots & \ddots & \vdots \\ H_{n1} & ... & H_{nn} - E_k \end{vmatrix} \tag{3.64}$$

E^0 represents the unperturbed energies of H_0 with the single particle basis functions ($|\psi_\alpha\rangle$). This expression simply gives the single particle energies of the orbitals by E^0 and the TBMEs by the $\langle\psi_\beta|V_{12}|\psi_\beta\rangle$, where $V_{12} = H_{res}$ and is the effective two-body interaction. The diagonalization of this Hamiltonian matrix in eq. 3.64 produces the n number of energy eigenvalues. Hence, the energies of the states inside the chosen model space, with selected A and T, are all determined.

Once the energy eigenvalues have been found, they may be substituted back into eq. 3.61 to calculate the coefficients a. The known coefficients may be placed into eq. 3.59 to determine the wave function for that particular state. This wave function may now be used to solve for other spectroscopic information related to the state.

The matrix elements of $H_{\beta\alpha}$ are a combination of the single-particle energies and the two-body matrix elements (TBMEs). The second part of equation 3.62 may be expressed in a more familiar form in terms of the total angular momentum J with the inclusion of isospin T as

$$\langle j_1 j_2; JM, T|V_{12}|j_3 j_4; JM, T\rangle, \tag{3.65}$$

for $T = 0$ or 1. These energies may be either calculated or determined by comparisons with experimental data. A description of three sets of effective interactions are given below. All that remains to complete the calculation is a determination of these TBMEs.

The choice of a two-nucleon interaction is difficult as the two nucleons feel the mean effects of all other nucleons in the nucleus. However, one way to determine the general two-body matrix elements (TBMEs) is from the free nucleon-nucleon interaction. This description will be hindered by the effects of all other nucleons in the nucleus, as mentioned above. Another possible way to find the TBMEs is to complete an empirical fit. Here, certain TBMEs are allowed to vary in a fitting procedure to the known experimental levels. This second procedure has been implemented to determine the shell model interactions used in the present work.

There are three main interactions that provide the two-body matrix elements (TBMEs) needed for the large scale shell model calculation that will be used to calculate spectroscopic

information in this work. They include the universal *sd* (USD) interaction [13] and the newer versions of this interaction (USD05a and USD05b) [27]. Also, the SDPF-M interaction, which uses a combination of interactions (SD-CB-KU) to span the *sd* and *fp* shells [11]. The USD and USD05 interactions were used with the nuclear shell model code CoSMo [2, 1] to calculate energies, spectroscopic factors and occupation numbers. The SDPF-M results were calculated using the OXBASH code [54].

The USD [13] interaction consists of three (3) single-particle energies (SPE) and sixty-three (63) two-body matrix elements (TBME). The starting point for this interaction comes from the re-normalized G matrix, which is based upon real nucleon-nucleon (NN) interactions. Taking a closed ^{16}O core and ^{40}Ca core (roughly $A = 17 - 39$), a set of TBME are found from the G matrix theory. This matrix can then be re-normalized to account for the effects of the reduced model space. Then, combined with experimental SPEs, these TBME can be used to describe nuclei near the closed shells. However, as one moves towards the center of a shell, this description deteriorates rapidly. To allow for a more complete description of an entire region of the nuclear chart, in this case the *sd* shell ($0d_{5/2}$, $1s_{1/2}$ and $0d_{3/2}$ orbitals), the TBME may be adjusted to match known experimental data. This empirical renormalization inside the *sd* shell was used to create the USD interaction [13]. The TBME of the G matrix that were determined to be of the largest importance, by the eigenvalues of the least-squares-fit matrix to the experimental data, were replaced by their empirical counter parts. The remaining TBME were left as the G matrix values. One set of TBMEs that held a large importance were those of the monopole interaction. This was due to the fact that they have a large effect on the SPEs mass dependence. These TBME are fit to the experimental SPEs and are given by

$$V^{T}_{j,j'} = \frac{\sum_J (2J+1)\langle j_1, j_2, J, T|V|j_1, j_2, J, T\rangle}{\sum_J (2J+1)} \tag{3.66}$$

with j_1 and j_2 representing the spins of the two nucleons. The USD interaction was found from a fit to 380 energies in the $A = 18 - 39$ region and the root-mean-square of the fitting was of about 185 keV. The resulting USD interaction has an overall mass dependence for the TBME of TBME^{A}=TBME$^{A=18}(A/18)^{-0.3}$. This interaction, has throughout the years, proved to be very valuable and a standard of comparison for all other models. The TBME and SPE for the USD interaction are given in Table I of Ref. [13].

The USD05 interactions [27] are simply more recent versions of the USD interaction [13].

Since a plethora of data has been acquired in the *sd* shell region since the first empirical renormalization of the G matrix occurred, a new fit to the data was competed. The fit included 608 states in 77 nuclei dispersed across the entire *sd* shell [27]. In this fit, great care was taken to not include states of known intruder configurations, such as, the group of *fp* intruder states apparent in the "island of inversion" region around $N = 20$ and $Z = 10 - 12$ [55]. The USD05a interaction was created by only allowing 30 of the TBME to vary from the starting point of the USD interaction. The USD05b interaction however, allowed for 56 of the TBME to vary to get the best over fit to the data. These interactions result in rms deviations of 171 keV and 126 keV when fit to the experimental data that was used in the first fitting of the USD interaction. Tables for each of these interactions (USD05a and USD05b) are shown in Ref. [27].

The SDPF-M interaction is comprised of three components, and allows for calculations across the $sd - pf$ $N = 20$ shell closure. The interaction for the *sd* component was the USD interaction [13], with some simple modifications. Since the USD interaction incorrectly calculates a bound ^{26}O ground state [13], the $T = 1$ matrix elements for the $\nu 0d_{3/2}$ and $0f_{7/2}$ orbitals were adjusted to be more repulsive. The reason that these two orbitals are important is because the neutrons occupy these orbitals for ^{26}O and above. The, $T = 0$ components were then made more attractive to compensate. However, only the $T = 1$ energies matter for oxygen, as only the neutrons are active in the *sd* shell. The matrix elements and their adjustments are given by

$$\begin{aligned} \delta V^{T=1,0}_{0d_{5/2},0d_{3/2}} &= +0.30, -0.70\text{MeV} \\ \delta V^{T=1,0}_{0d_{5/2},0f_{7/2}} &= +0.16, -0.50\text{MeV} \end{aligned} \tag{3.67}$$

These modifications ensure an unbound ^{26}O ground state, while having little effect on the $^{17-24}$O ground states. Also, the pairing interaction in the *sd* shell had to be modified. Implicit effects of the upper *pf* shell had to be removed by shifting the pairing matrix elements by $\delta G = -0.1$ MeV. This change did not affect the 2^+ energies of the *sd* states outside of the range of the original USD interaction. The *pf* shell component of the SDPF-M interaction comes from the Kuo-Brown (KB) interaction [56]. This interaction was also found from the re-normalized G matrix. The cross-shell contribution between the *sd* and *pf* shells, is the third part of the interaction [57]. This was based on the Milleneer-Kurath (MK) interaction [58]. All interactions scale with mass as $A^{-0.3}$, as was the case with the

USD, and USD05 interactions. The SDPF-M interaction has played an important role in describing the ground and excited states, as well as other spectroscopic factors such as $\log ft$ values, in the "island of inversion" region around $N = 20$ [11, 40, 55, 59].

A main quantity that is important in the present work is the spectroscopic factor $S_{l,j}$ between two states for various values of orbital angular momentum. The spectroscopic factor is related to the expansion of the wave function of an initial nucleus (Ψ_i^A) with mass A in terms of the summation over a complete set basis states in the $A-1$ nucleus (Ψ_f^{A-1}). This is given by

$$\Psi_i^A = \sum_{f,l,j} \Theta_{i,f,l,j}(\vec{r})\Psi_f^{A-1}. \tag{3.68}$$

Therefore, the overlap function is expressed as

$$\sum_{l,j} \Theta_{i,f,l,j}(\vec{r}) = \langle \Psi_i^A | \Psi_f^{A-1} \rangle. \tag{3.69}$$

The spectroscopic amplitude $A_{l,j}$ may be related to the normalized overlap function by

$$A_{i,f,l,j} = \int \Theta_{i,f,l,j}(\vec{r}) d\tau, \tag{3.70}$$

and the spectroscopic factor is simply the absolute square of the amplitude

$$S_{i,f,l,j} = |A_{i,f,l,j}|^2. \tag{3.71}$$

Furthermore, the overlap function may be expanded in terms of a complete set of single-particle wave functions ($\phi_k(\vec{r})$) as

$$\Theta_{i,f,l,j}(\vec{r}) = \sum B_{i,f,k}\phi_k(\vec{r}), \tag{3.72}$$

where the coefficients are given by $B_{i,f,k}$. The spectroscopic factor may now be give by

$$S_{i,f,l,j} = |B_{i,f,k}|^2. \tag{3.73}$$

As can be seen from the derivation above, the spectroscopic factor indicates the overlap between two states for various values of orbital angular momentum l. What this value can further show is if the decaying state has a similar wave function to the states that it decayed too. Therefore, the spectroscopic factor highlights the favorable decay paths for a decaying state.

CHAPTER 4

EXPERIMENT

4.1 Ion Beam Characteristics

4.1.1 Primary Beam

The radioactive secondary ^{26}F beam was produced by the Coupled Cyclotron Facility (CCF) at the National Superconducting Cyclotron Laboratory (NSCL) on the campus of Michigan State University. The primary ^{48}Ca beam began with an injection from the ion source into the K500 superconducting cyclotron with a charge state of +8, i.e. lacking 8 electrons. Exiting the K500 cyclotron at an energy of 12.3 MeV/u the $^{48}Ca^{+8}$ was stripped of all its remaining electrons to a charge state of 20^+ and then injected into the larger of the two cyclotrons, the K1200. Extraction of the $^{48}Ca^{20+}$ from the K1200 occurred at a primary beam energy of 140 MeV/u and was transported to the object position of the A1900 mass separator [16] at a beam intensity of ∼15 particle nano-Amperes (pnA). At the object position was a 987 mg/cm^2 thick natural Beryllium (Be, $Z = 4$) production target to fragment the incoming $^{48}Ca^{20+}$ primary beam. A schematic of the CCF and the A190 mass separator is shown in Fig. 4.1.

4.1.2 Secondary Beam

The A1900 mass spectrometer works as a mass analyzer by selecting charged ions with specific momentum and mass over charge ($^{m}/_{q}$) ratios. The selection is accomplished by setting the magnetic rigidity of the four superconducting dipole magnets to proper magnetic rigidities. The final dipole magnet had a rigidity of $B\rho = 3.9301$ Tm. Also, for the optimum cleanliness of the secondary ^{26}F beam, an Aluminum (Al, $Z = 13$) wedge of thickness 1050 mg/cm^2 was inserted at the intermediate focal plane to selectively disperse the contaminant products

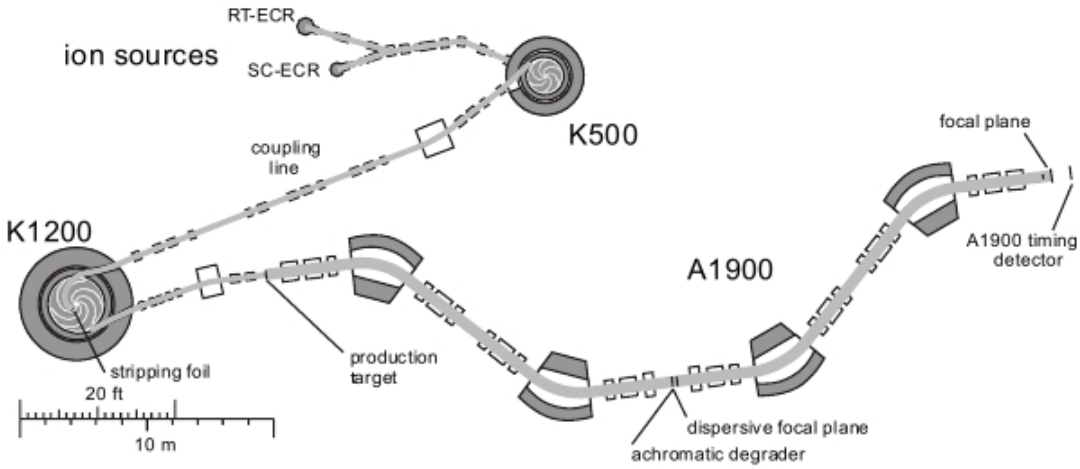

Figure 4.1: The Coupled Cyclotron Facility at the National Superconducting Cyclotron Laboratory at Michigan State University is shown by the schematic above. Also shown is the A1900 mass spectrometer [16]. The cyclotrons and mass separator were used to create a high intensity secondary beam of the radioactive ion ^{26}F.

from the desired ^{26}F beam. Slits were also imposed at the intermediate focal plane to further remove contaminant fragments while not reducing the rate of the ^{26}F too drastically. Exiting the A1900 mass separator was an 85 MeV/u ^{26}F beam with a beam purity of 50%. The energy of the final beam is lower than the primary ^{48}Ca beam due to the energy loss of the fragmentation and the energy losses of the ions as they carry through the primary Be target and the Al wedge. The major contamination was from the isotope of ^{29}Na. A final rate of $\sim$ 1 particle per-second per-particle nano-Ampere (pps/pnA) was transported to the experimental.

4.2 Experimental Setup

The experimental setup used in the measurements of the neutron unbound states of the oxygen isotopes at the NSCL is shown in Fig. 4.2. The secondary ^{26}F beam that has been selected by the A1900 spectrometer interacts with a thin 5 mm plastic timing scintillator upon its exit. Then the ^{26}F beam enters the experimental area (Yellow line coming from the left in Fig. 4.2) and its spatial characteristics are determined by two position sensitive parallel-plate avalanche chambers (PPACs) that were placed 3.97 m upstream of the

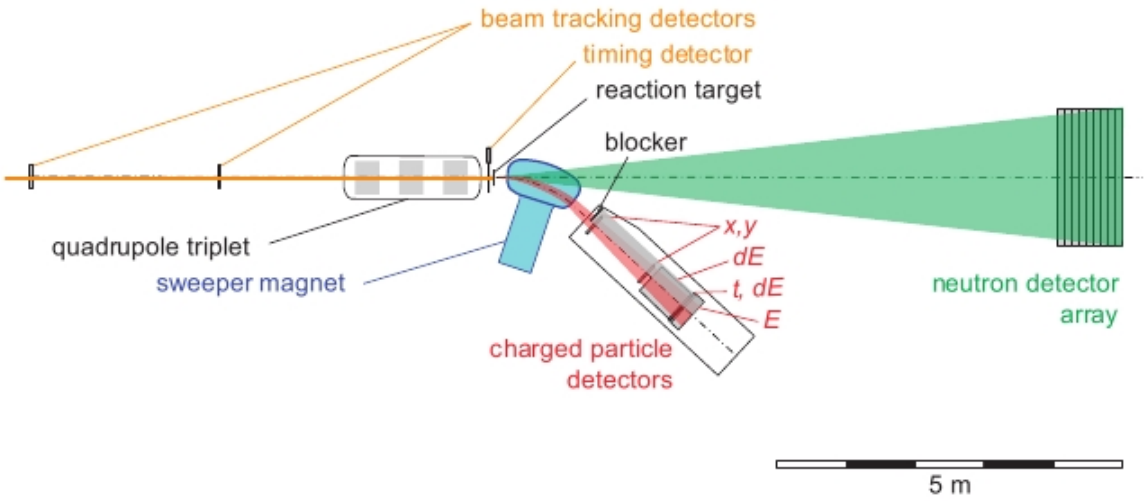

Figure 4.2: The Sweeper-MoNA experimental setup at the NSCL is shown above. The flight path of the beam is shown in yellow. The decay fragments and neutrons flight paths after the target are shown by the red and green lines respectively. The dipole Sweeper magnet [17] is shown in blue.

secondary target. The secondary beam is focused onto the target by a triplet of quadrupole magnets. Another thin 0.254 mm plastic scintillator is located just before the target giving timing information of the beam and for the neutrons' times-of-flight (ToF). The ^{26}F beam interacts with a secondary Be target that was located at the object position of a 4 Tesla (T) large-gap dipole (Sweeper) magnet [17].

Fragments produced in the secondary reaction (^{26}F impinging on ^{9}Be) are bent 43° by the Sweeper magnet and their position and angle information were determined by two cathode-readout drift chambers (CRDCs). Following the CRDCs was a multi-sectioned ion-chamber and two segmented plastic scintillators. The first plastic scintillator is a thin ΔE 0.5 cm thick detector which provided the master timing trigger for the experiment. The second plastic scintillator was thick 15 cm and stopped the charged fragments while measuring their remaining energy. The ion chamber was used with the plastic scintillators to give fragment energy loss and total kinetic energy information.

Neutrons that originated from the secondary reaction target were forward focused due to the high beam velocity ($\sim$ 0.3c) and were detected by the Modular Neutron Array

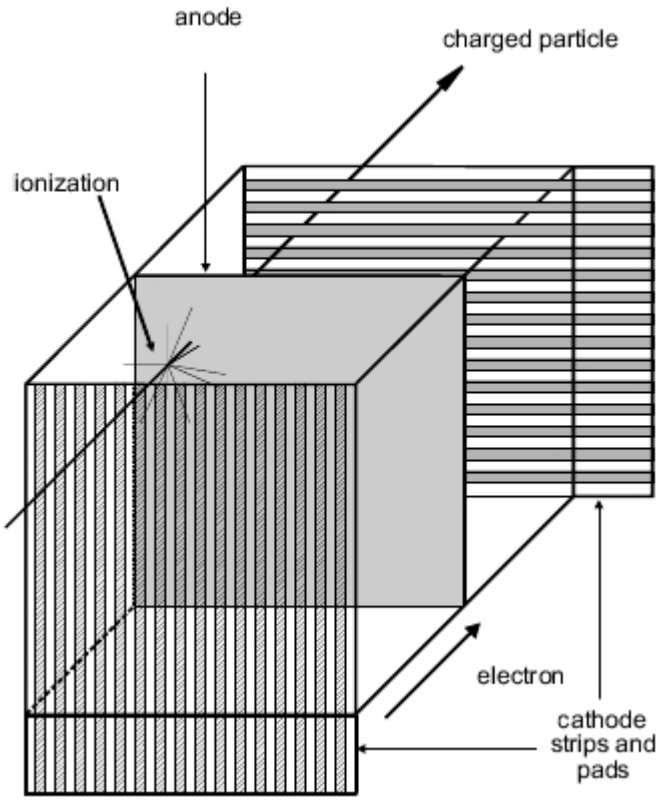

Figure 4.3: The design and mechanism of a Parallel-Plate Avalanche Counter (PPAC).

(MoNA) [60]. MoNA was centered around 0° and located 8.2 m from the target so as to give the time-of-flight (ToF) information of the neutrons. Due to its segmented design, position and angle information of the neutrons was also measured.

4.2.1 Beam Line Detectors

The secondary ^{26}F beam is tracked to the target by two position sensitive Parallel-Plate Avalanche Counters (PPACs). The purpose of these detectors is to provide input information to a forward mapping matrix which maps the secondary beam particles to their locations and angles at the reaction target. Fig. 4.3 shows a schematic view of the inner workings and design of the PPACs that were used. A PPAC could detect the position of a particle as it passed through the detector. The PPACs functioned as follows. The central plate (anode) was set to a central voltage of 590 V. The anode plate and the cathode strips which were

located at each end, were all enclosed inside 5 Torr of iso-butane gas. There are 40 cathode strips at each end with one set being arranged in the vertical direction and the other in the horizontal direction. A charged fragment propagating through the detector ionizes the iso-butane gas creating a positive ions and electrons. The electrons are drawn toward the cathode grid and are detected by a number of the strips. The measured charge distribution on the strips is used to determined the position of the passing ion. A final position resolution of $\sim$ 1 mm FWHM was found for each detector. Using the two PPACs simultaneously spaced 2.719 m apart, an angle resolution of $\sim$ 2 mrad FWHM was found. These values translate into a final target position and angle resolutions (FWHM) of $\sim$ 2 mm and 2.5 mrad after using the forward tracking prescription described in chapter 5. The total efficiency for the PPACs during the experiment was $\sim$ 50% due to the tripping of high voltage of the anode due to the large charge deposition of a high rate secondary beam.

4.2.2 Target Chamber

The target chamber housed the 987 mg/cm^2 secondary Be target and the target timing scintillator. The target was located at the object position of the dipole Sweeper magnet and the scintillator was located 0.34 mm in front of the secondary target. The plastic timing scintillator was made of BC-404 fast counting plastic material and had a thickness of 0.254 mm. As fragments passes through the detector they created electron-hole pairs which recombined to form visible light. The visible light was collected by a single photo-multiplier tube (PMT) that was intimately connected to the scintillator to capture as much light as possible. The PMT converted the light into an electronic signal representing the time the fragment passed through the material. The final timing resolution of this detector was $<$ 1 ns and its signal is important for secondary beam fragment identification and for the determination of the neutron times-of-flight (ToF).

4.2.3 Sweeper magnet

A large-gap superconducting dipole Sweeper magnet was commissioned and built by the Florida State University National High Magnetic Field Laboratory [17]. The Sweeper magnet is capable of deflecting charge fragments with magnetic rigidities up to 4 Tm by 43°. The vertical gap of the magnet is large (14 cm) to allow neutrons to go through relatively unabated. The problem that the large-gap creates is that the magnetic field is slightly less

uniform over the region of the fragment's flight path. Therefore, great care was taken to map out the magnetic field and reconstruct it properly [20]. Niobium-Titanium (Nb-Ti) coils create the maximum 4 T field and resistive coils on the outside of the magnet can cancel the field outside the yoke to allow for sensitive instrumentation to be placed nearby. For this experiment the central track rigidity of the magnet was set to $B\rho = 3.7755$ Tm, the rigidity of the ^{24}O fragments after the target, to allow for the greatest acceptance of these ions.

4.2.4 Fragment Detectors

Placed directly after the dipole Sweeper magnet are two position sensitive Cathode-Readout Drift Chambers (CRDCs) separated by 1.88 m. These two detectors are 30×30 cm^2 and measure positions and determine angles of recoil fragments with resolutions (FWHM) of $\sim$2 mm and $\sim$ 2 mrad. The detector design is shown in Fig. 4.4. They functioned by having the 50 Torr 20% iso-butane and 80% CF_4 gas mixture create charged ion-electron pairs as a fragment propagated through the detector. The free electrons moved along an electric field created by a -700 V potential at the top of the detector which was connected to a set of 128 Aluminum pads through a resistor chain. The electrons passed through a Frisch grid held at around -10 V and after were collected by an anode wire at +900 V. The induced electrons that were created around the anode wire caused an avalanche to occur. These avalanche electrons were collected by the 128 Aluminum pads. The cathode pads had a fixed spacing (pitch of 2.54 mm) and hence determination of the horizontal position of the charged fragment was made possible by knowing which pads collected the charge. The time it took for the electrons to drift to the anode wire held determined the vertical position of the charged fragment. Following the second CRDC was an energy-loss ion-chamber detector of length 0.706 m. The detector was filled with 150 Torr of 90% argon and 10% methane gas. 16 collection plates held at +200 V measured the electrons created by the interaction of the recoil fragments as they passed through the gas mixture. A potential of -800 V was applied to the opposite side of the plates to force the drift of the electrons. By using a number of collection plates the noise of the system could be reduced as well as letting higher particle rates to be handled. The combination of the total charge collection by all 16 plates allowed for an accurate energy loss measurement which would be used for proper elemental identification.

Two scintillators made of BC-404 plastic with thicknesses of 0.5 cm (thin ΔE) and 15 cm

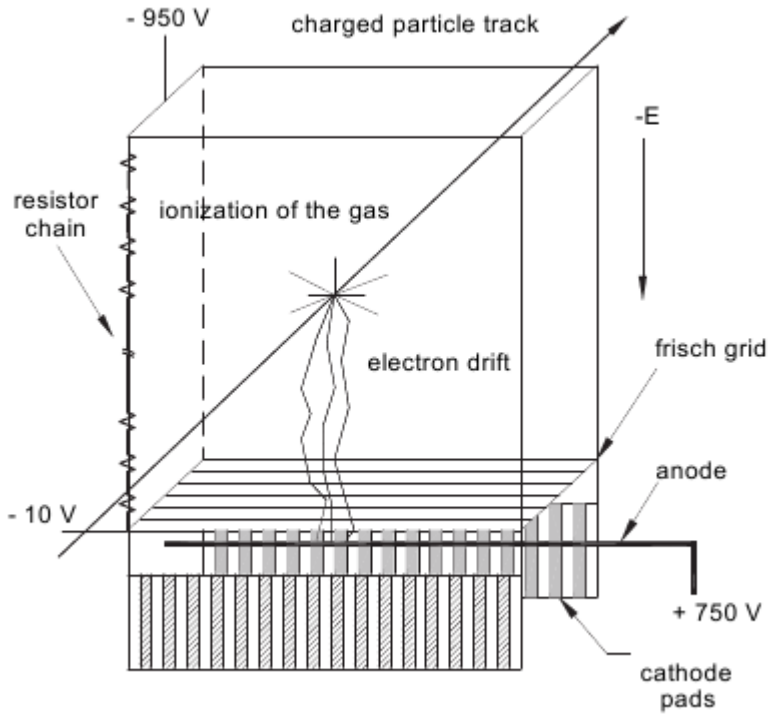

Figure 4.4: The design and mechanism of a Cathode-Readout Drift Chamber (CRDC).

(thick TKE) were located immediately following the ion-chamber and CRDCs. Each plastic scintillator was 30×30 cm^2 and used four separate photo-multiplier tubes (PMTs) for the collection of light. The thin ΔE (0.5 cm) detector was placed before the thick TKE (15 cm) detector. The thin ΔE detector acted as the main trigger in the experiment, while the thick TKE detector stopped the recoil fragments and determined their total kinetic energy (TKE). The thin ΔE detector also measured the light output to determine the energy loss through its material. These energy measurements also helped in the elemental identification. The thin ΔE detector also gave the timing information needed to distinguish isotopes.

4.2.5 Modular Neutron Array (MoNA)

The Modular Neutron Array (MoNA) lies at 8.20(5) m from the target and around 0° relative to the beam direction. MoNA is comprised of 144 $10 \times 10 \times 200$ cm^3 BC-408 plastic scintillator bars arranged in a 16 X 9 configuration. The size of the detector allowed

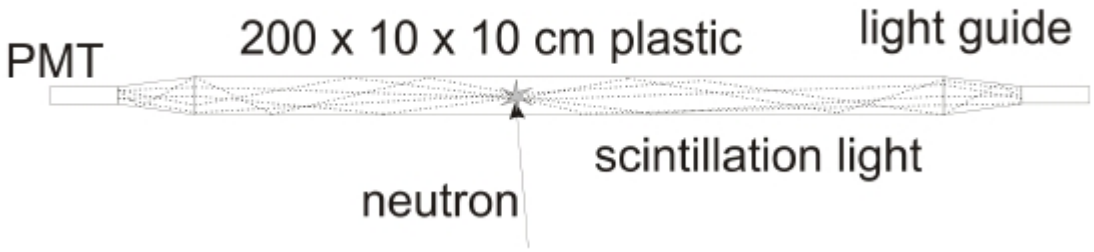

Figure 4.5: A single MoNA bar ($10 \times 10 \times 200\text{cm}^3$) is shown above schematically. The photo-multiplier tubes (PMTs) located at each end of the bar collect the light produced by a neutron interacting with the BC-408 plastic, a hydrogen-carbon compound. Also shown schematically is a neutron interacting with the plastic lattice producing visible light that is guided to the PMTs where it is collected. The time difference between the collection of the light for the two PMTs gives the horizontal location of the interacting neutron.

for $\pm 7.0^\circ$ of horizontal and $\pm 5.6^\circ$ of vertical frontal coverage for the detection of neutrons from the target. Each plastic bar has a photo-multiplier tube (PMT) attached to each end accompanied by a connecting light guide. As neutrons interact with the charged particles of the plastic (protons or carbon nuclei), they become excited and relax by the release of photons of light which are gathered by the PMTs at the bars ends. A schematic view of a single neutron bar is shown in Fig. 4.5 The PMTs outputs give the time and total charge collection information. The time difference between the PMTs at different ends gives the location of the horizontal position of the interaction. The average time of the two PMT signals gives a time stamp that can be used with the coincidence time of the target scintillator to determine the time-of-flight (ToF) of a neutron to MoNA. The ToF can be used to calculate the kinetic energy of the decay neutron if its flight path is known. The vertical and longitudinal positions of a detected neutron were determined by which bar of the array was struck. Therefore, these two position measurements each have an uncertainty of ± 5 cm.

4.2.6 Electronics and Data Acquisition

The neutron detector (MoNA) and the fragment detectors (Sweeper), may both be run independently. They each have sophisticated electronics and data acquisition (DAQ) setups that have been well described in Ref. [18] for MoNA and Ref. [20] for the Sweeper. In this thesis, only the electronics and DAQ that highlight the interplay between the two setups

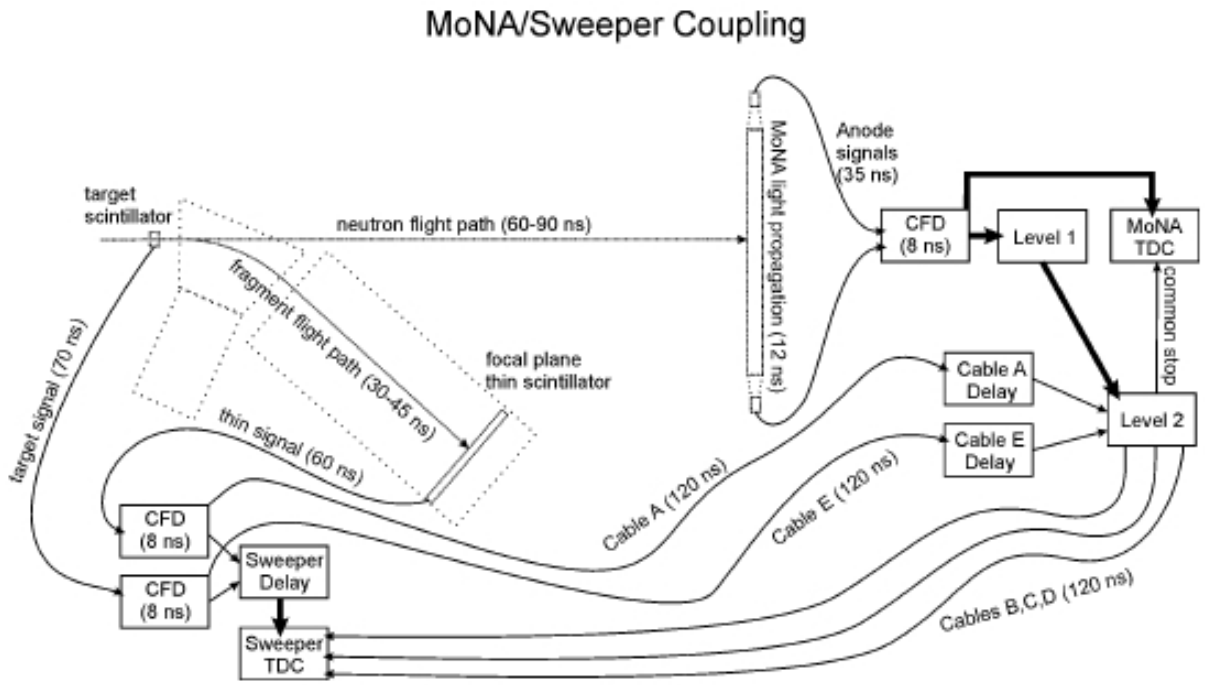

Figure 4.6: A schematic diagram of the coupling of the timing electronics of the MoNA experimental device and the Sweeper detector electronics. There are five cables can intimately connect the two and they are cables A,B,C,D, and E. Cables A and E transport the master trigger and common timing stop signals from the Sweeper electronics to MoNA. Cable B sends out a latched "veto" signal, cable C sends a "fast clear" signal and cable D sends out a computer 'GO' signal. The Level 1 and Level 2 boxes represent the logic modules used to determine a valid coincidence event. The amount of time for the particle and signal propagations are also included on the diagram in ns. [18]

will be described as this is how the experiment was carried out. The electronics and DAQ for running the MoNA setup and the Sweeper setup in tandem are shown schematically in Fig. 4.6. As can been seen there are five cables that interconnect the MoNA setup with the Sweeper setup, they are label A,B,C,D, and E. The master trigger for the entire setup is a signal from the thin ΔE plastic scintillator located in the dipole Sweeper magnets focal plane. The 'OR' of the four PMTs connected to this scintillator produces a time signal that is sent to a logic module at MoNA (Level 2) through cable A. At the same moment, cable E sends a common stop signal from the thin plastic scintillator located at the target position. This is a common stop signal for all of the MoNA PMTs. When the time signal

arrives through cable A a latched "veto" is sent out through cable B back to the Sweeper electronics. This signal halts all other electronic processes until the Level 2 logic decides if their is a good coincidence or not. In the Level 2 logic module, a good coincidence is determined if the MoNA Level 1 logic model signal sent a signal showing two simultaneous PMT signals for a single bar of MoNA, i.e. a neutron event, and this Level 1 signal overlaps with the thin ΔE time signal. If this overlap does not happen then a "fast clear" signal is sent to the MoNA modules and the Sweeper electronics through cable C. The "fast clear" resets all the modules as quickly as possible ($\sim$700 ns) so that they can begin collection again. This signal also closes the latched "veto" so that the electronics are free to collect the next event. However, if a good neutron event (Level 1 signal) does indeed overlap with the thin ΔE time signal then a computer 'GO' signal is sent out to the MoNA electronic and the Sweeper electronics via cable D. This signal allows for the DAQ to read all modules and collect all the data that is in coincidence. This refers to the digitizing of the electronic data which is on the order of microseconds. After the computer has finished its data collection, the latch "veto" is closed and the electronics are reset to allow collection of the next event. The entire process takes less than $\sim$800 ns to determine if there is a valid event.

CHAPTER 5

ANALYSIS PROCEDURE

5.1 Overview

The ultimate goal of the data analysis is to extract the resonance parameters for the decay energy and width from the invariant mass spectra of $^{23-24}$O+n coincidence data. After calibration of the experimental devices, the fragment-neutron coincidence events must be identified. The full kinematics for these pairs are then calculated and, using equations 3.5 and 3.6, the decay spectra are obtained. The experimental analysis uses the software package SpecTcl [61]. The entire experimental response is simulated using the Monte Carlo simulation software ST-mona [15]. Inserting a Breit-Wigner line-shape function (eq. 3.8) into the simulation allowed for the extraction of the physical energy and width for the observed resonances. Described below is the optimized analysis procedure to investigate the observed states in ^{24}O and ^{25}O.

5.2 Calibrations

5.2.1 MoNA

The Modular Neutron Array (MoNA) uses 144 plastic scintillator bars of dimensions $10 \times 10 \times 200$ cm^2 which have photo-multiplier tubes (PMTs) on each end [60]. It is the collection of light by these PMTs that give the stopping time for neutrons emanating from the target, as well as the horizontal position of the interaction inside a single bar. The total charge of the interaction is also collected by the PMTs and therefore, a careful calibration of these PMTs is needed.

A number of the calibrations for MoNA are done by using data collected from cosmic ray muons. These muons are created when a cosmic ray (typically a fast moving proton)

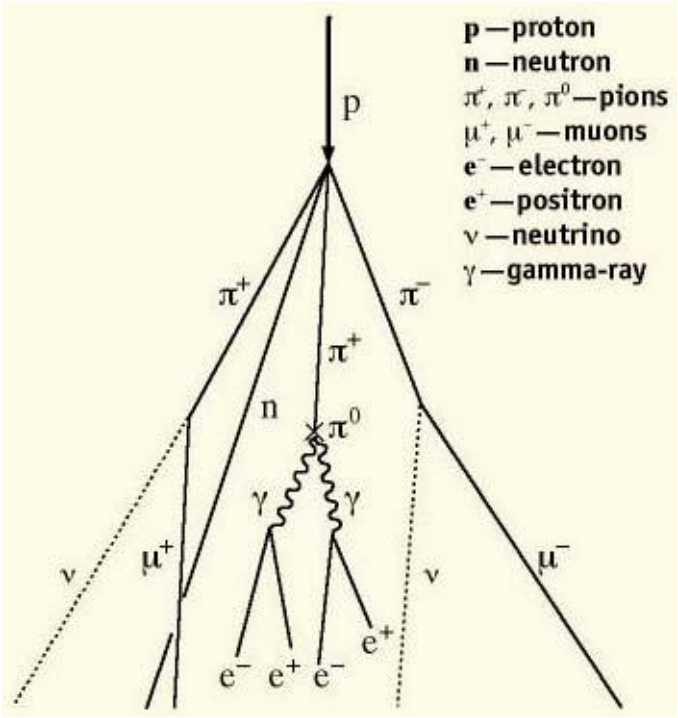

Figure 5.1: Shown schematically is the process of a cosmic ray, composed of mainly high energy protons, interacting with the earths upper atmosphere. This process creates a large number of pions which then decay into high velocity (0.998c) muons. The muon flux that reaches sea level is on the order of 1 per cm^2 per minute.

strikes the earths upper atmosphere creating a shower of pions. The pions then decay into fast moving muons ($v = 0.998c$) which make it to the earth's surface with a flux of about 1 per cm^2 per minute. A schematic of this process is shown in Fig. 5.1. Fast moving muons scatter off of the plastic inside the MoNA bars in the same way as a neutron, depositing on average the electron equivalent of 22 MeV of energy in each bar as they pass through the entire array at once. Since muons travel at nearly the speed of light and deposit a standard, known amount of energy, they are excellent for detector calibrations.

A slight variation in PMT voltage may result in largely different light collection efficiencies. To ensure that each bar, and each PMT at the end of a single bar, are consistent, the PMTs are gain matched. To due this a long run is completed to allow for all of the bars to have ample cosmic ray data, in particular, PMT data for the raw charge-to-digital (QDC) spectra. The QDC converts the measured light output to a digital signal and provides an

excellent measure of the relative energy. Each of the individual PMT spectra are fitted using a simple routine to check that the low channel cutoff and the center of the muon peak are at certain channel numbers previously chosen [18]. If a PMT is not, then the high voltage is adjusted until all PMTs have nearly identical muon spectra. These QDC muon spectra are calibrated by setting the low channel cutoff to zero energy and the centroid of the peak to the energy deposited by the muon (the electron equivalent of 22 MeV).

The anode outputs from the PMTs are sent to the time-to-digital (TDC) converter modules which accurately measure the time difference between the PMT and another input signal, i.e. the master trigger time. The way a TDC works is to begin charging a capacitor when the start signal is acquired. Then when the stop signal arrives the capacitor stops being charged and is allowed to discharge with a constant current source. The amount of time it takes for the discharge to occur gives a relative timing signal. Since each TDC does not have the exact charge and discharge rates, they must be calibrated to each other. This is accomplished using a pulser device which can supply all of the TDCs with a series of pulses of known interval simultaneously. Then these spectra can be fit and slopes and offsets are determined to make spectra match.

The kinetic energy of a neutron coming from a decay inside the reaction target may be found using the time-of-flight (ToF) of the neutron from the target to MoNA. This time can be found by using the average time from the calibrated TDC spectra for two PMTs from a single MoNA bar and its difference from the time of the plastic scintillator located just before the target. This overall spectrum must be calibrated very precisely to ensure proper calculation of the neutron ToF and hence, velocity and kinetic energy. To calibrate this spectrum the γ-ray flash from the reaction target is looked at for a single bar in MoNA of known distance. γ rays from the target come from the excited states of nuclei produced by a number of reactions involving the secondary beam on the secondary target. Since γ rays have zero mass, they travel at the speed of light and their ToF can be determined very precisely when the flight distance is known. Therefore, a single bar in MoNA is chosen. In this particular case it was the middle bar of the first column, at a distance of 8.2 m so the γ-ray peak was adjusted to come at 27.3 ns. After a single bar has been calibrated, all of the remaining bars of MoNA can be calibrated relative to it by using the cosmic ray data. With a velocity of nearly the speed of light, the average flight time for a muon to travel from bar to bar is 0.33 ns for the 10 cm flight path. Therefore, the data can be searched for

muons that travel through adjacent bars and their relative times are then adjusted to the one calibrated bar. This results in all of the bars of MoNA being calibrated relative to the target position, i.e. the position of the neutron decays.

The position calibrations for neutrons interacting with MoNA are simple for the longitudinal and vertical as these are simply determined by which bar was struck, i.e. two good PMT signals. The horizontal position is determined by the time difference between the two PMTs at the ends of a single bar, given by

$$\Delta t = \frac{1}{2}(t_l - t_r) \tag{5.1}$$

with the times (t) in ns. To convert the value into cm a calibration is needed. Again, using the cosmic ray data which illuminates the entire array, a fitting procure is done which searches for the edge of the time spectra by find the point at with 1/3 of the maximum is reached. It has been determined through simulation that this point well represents the real horizontal ends of the bars. Once these horizontal left and right positions have been determined from the cosmic data, the slope and offsets are found by

$$M = \frac{200}{x_l - x_r} \tag{5.2}$$

$$B = -M\frac{x_l + x_r}{2} \tag{5.3}$$

where M is the slope, B is the offset, and x_l, x_r are the horizontal left and right positions. The final horizontal position is then

$$x = M \cdot \Delta t + B \tag{5.4}$$

5.2.2 Position Detectors

The position sensitive detectors before the target to track the beam (parallel-plate avalanche counters PPACs) and after the Dipole magnet to track the fragments (cathode-readout drift chambers CRDCs) both needed to be calibrated. The CRDCs have 128 pads in the horizontal direction, and the PPACs had 40 pads in each direction, which had to first be gained matched by looking a the total charge deposited in each and adjusting the pedestals. The position of a particle was determined by making a Gaussian fit to the charge distribution across a

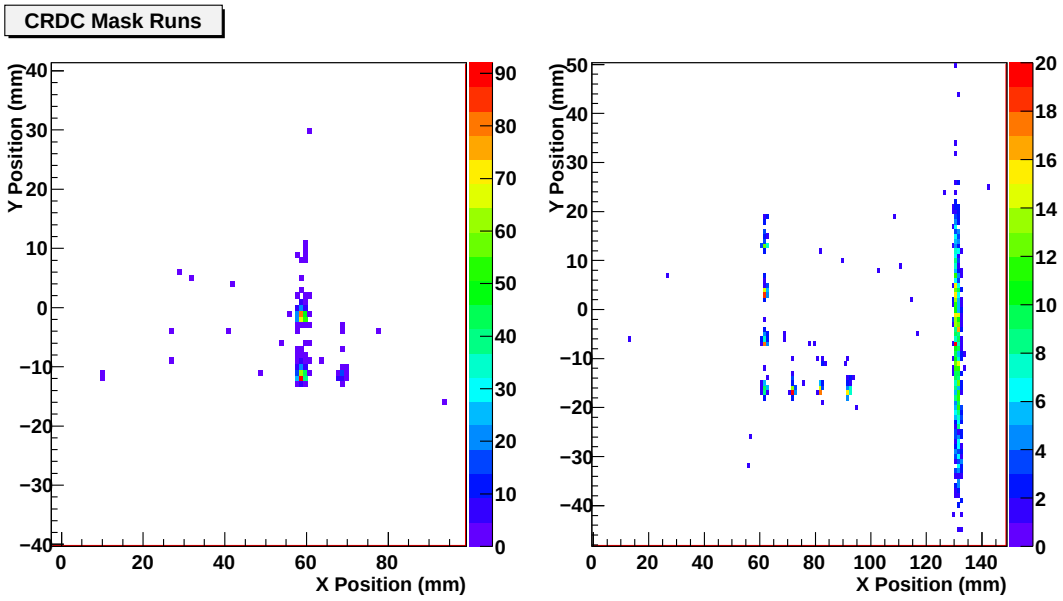

Figure 5.2: A calibrated mask run is shown for the two cathode-readout drift chambers (CRDCs) located after the dipole Sweeper magnet. The mask was placed in front of the detectors and the positions of the holes were used to calibrate calculate the offsets and the vertical slope. The same procedure was used for the beam-line tracking detectors (PPACs).

certain number of the pads. The σ value for this Gaussian fit was determined by looking at the pad multiplicity for typical data. The values of $\sigma = 5$ and $\sigma = 3$ were determined for the CRDCs and PPACs respectively. The centroid of the Gaussian determines the position which then had to be calibrated in real space. The slope can easily be determined by using the pitch of the pads for the horizontal direction of the CRDCs (pitch = 2.54 mm) and the both directions for the PPACs (pitch = 1.27 mm). The offsets for these positions were found by placing a mask in front of each detector, in which holes in the mask as well the placement in space were previously known. Hence, an offset could be included to match the already known mask hole positions. Fig 5.2 shows a single mask run for the two CRDCs, the hole positions were known physically in space so as to set the offsets and the vertical slope. Furthermore, the vertical direction for the CRDCs was calibrated by taking a number of holes in this direction and fitting them linearly to acquire an offset and slope. Hence, all vertical and horizontal positions were calibrated for the CRDCs and PPACs. Final resolutions for the angles and positions of the the PPACs were 1.3 mrad and 1.3 mm FWHM. The same values for the CRDCs were 1.3 mrad and 1.3 mm FWHM.

5.2.3 Energy Detectors

The ion-chamber and two plastic scintillators located after the CRDCs and after the Sweeper Dipole Magnet had to be calibrated to identify the different elements that made their way into the focal plane. The ion-chamber energy is comprised of the sum of all 16 plates, all being gained matched, and the energy from the ΔE (0.5 cm) and TKE (15 cm) scintillators is simply the energy sum of their four photo-multipliers for each. Using the positions and angles from the CRDCs, each detector included a correction for the flight path of an ion through its material. This was done using a simple linear relation between distance and energy, whereby the linear coefficient was adjusted until the two-dimensional plot of energy loss versus distance showed straight parallel lines. The energy loss and total energy spectra were then calibrated absolutely by using the secondary beam comprised of ^{26}F and ^{29}Na at known energies, with no target in place. Also, as a check of the calculation, the energy losses for the un-reacted ^{26}F and ^{29}Na ions that made it through the detectors were calculated. Hence, there are two calibrated energy loss measurements (ΔE) and a total kinetic energy measurement (TKE).

5.2.4 Timing Detectors

The timing relations for particles, including beam, fragments and neutrons, are all very important to the data analysis. Because of this, special care had to be taken for the timing detectors that were used. These include the A1900 focal plane scintillator, a plastic scintillator before the target and the ΔE and TKE plastic scintillators. The ΔE scintillator was the overall timing start for the experiment. Therefore, the measured times from each of its four photo-multiplier tubes were corrected for the flight path of the light through the detector. This was done by extrapolating the impact position from the CRDC measurements and then calculating the linear distance from the impact point on the plastic to the center of each PMT. The velocity of light in BC-404, the plastic of the scintillator is given by

$$v = \frac{d}{t} = \frac{c}{1.58} \tag{5.5}$$

where the distance d is the distance from the interaction point to the center of the PMT and the time t is the amount subtracted from the raw measured value for each PMT. This produces a much sharper average start time for all events [20].

An absolute time calibration for the flight time between the A1900 focal plane detector and the target is useful for identifying secondary beam fragments. This time as calculated by the rough energy and distance for one of the identified fragments. The ^{29}Na was a strong secondary beam product and using its calculated energy and a distance of 35.68 m from the A1900 to the target, these time spectra were calibrated. In the same manner the time difference between the target detector and the thin ΔE detector was estimated by using the secondary beam products, again with no target in place. Using the magnetic rigidity of the Sweeper magnet, the flight path for each fragment can be estimated and combined with their known energies to calculate an approximate ToF. This is only approximate because the particles may take slightly different trajectories through the magnet resulting in various different flight paths. The calibration for the time between the target detector and MoNA was described above.

5.3 Oxygen Fragment Identification

5.3.1 ^{26}F Secondary Beam Selection

The ^{26}F secondary beam that was selected by the A1900 mass spectrometer [16] and made it to the secondary target, was contaminated by 50%. Most of the contamination came from the ^{29}Na isotope, while a few light particles appeared, as well. The magnetic rigidity of this secondary beam is the same constant value for all beam particles, and is determined by the last dipole magnet of the A1900 spectrometer, $B\rho = 3.9301$ Tm. The magnetic rigidity is derived by the force of a particle with charge q moving through a magnetic field of strength B, and with a velocity of v,

$$\vec{F} = \frac{d\vec{p}}{dt} = q\vec{v} \times \vec{B} \tag{5.6}$$

Now integrating with respect to time on both sides taking $p(t_\circ) = 0$ and $v(t_\circ) = 0$, also assuming a constant magnetic field,

$$p = mv = qB\rho, \tag{5.7}$$

with ρ being the radius of the circle that the ion is traveling, and m the mass of the particle. Finally, through simple manipulation

$$B\rho = \frac{mv}{q}, \tag{5.8}$$

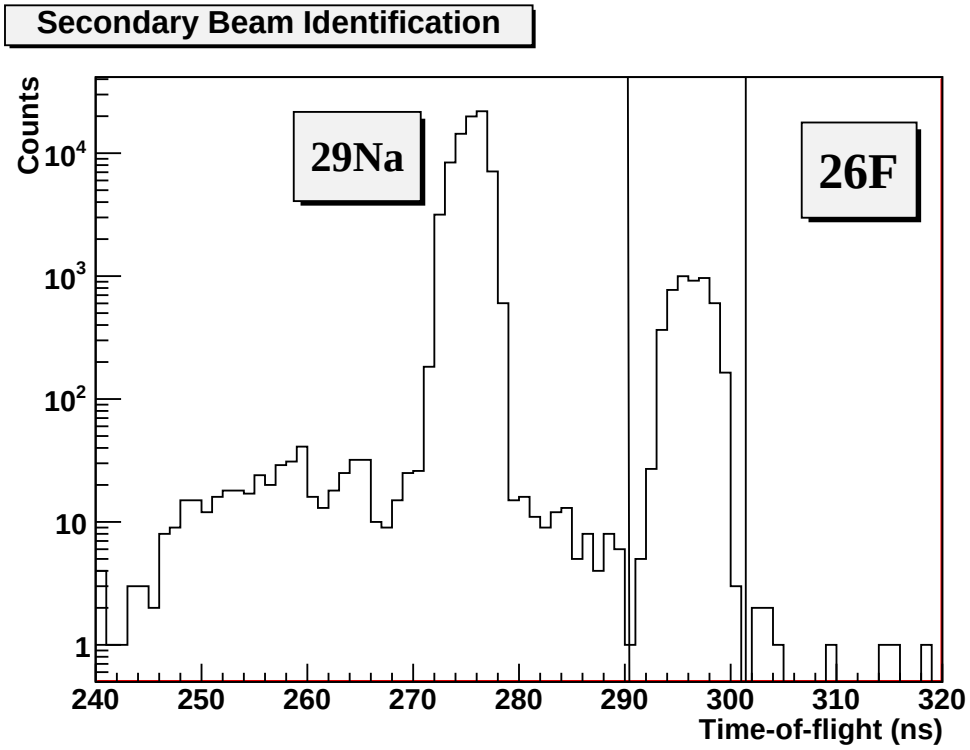

Figure 5.3: The calibrated time-of-flight spectra measured from the extended focal plane of the A1900 spectrometer to the secondary target positions (35.68 m). The radioactive ^{26}F beam is cleanly identified from the other contaminants, mainly ^{29}Na, by the difference in their mass over charge ratio m/q which leads to different times-of-flight for a constant magnetic rigidity ($B\rho$).

where $B\rho$ is the magnetic rigidity, mv is the momentum which is the product of the mass m and velocity v, over q, the charge of the ion. Noting that the m/q ratio differs for ^{26}F and ^{29}Na, $\frac{26}{9} = 2.89$ and $\frac{29}{11} = 2.64$ respectively, we see that their velocities are then also different, ^{26}F=12.024 cm/ns and ^{29}Na=12.975 cm/ns. Using this information we can cleanly identify the ^{26}F beam from contaminants based on its velocity.

Since the velocity of an ion is given classically as $v = \frac{Distance}{Time-of-Flight}$, then over a fixed distance the time-of-flight (ToF) reflects the different velocities. Hence, using the timing scintillator that was placed at the focal plane of the A1900 mass separator and the timing scintillator that was located at the secondary target position, we can calculated a ToF for beam particles over a distance of 35.68 m. This long distance and the timing resolution of the scintillators (< 1 ns) give more than enough resolution to cleanly separate the ^{26}F beam

as the calculated ToFs for the ^{26}F and ^{29}Na ions are 296.7 ns and 275.0 ns respectively. Shown in Fig. 5.3 is the times-of-flight for the secondary beam from the A1900 focal plane to the secondary target with the ^{26}F and ^{29}Na beams cleanly identified. A gate was set in this spectrum to be sure that only the incoming radioactive ^{26}F beam and its reaction products be considered as real decay events.

5.3.2 Element Selection

After the decay process, the charged recoil fragments having desired magnetic rigidities ($B\rho$) made it through the Sweeper magnet and into the detectors which were positioned around the central track of the magnet. Since a number of different mass over charge products were accepted, these fragments must be identified if they are to be used to reconstruct a decay energy.

Energy loss information collected by the ion-chamber, thin ΔE (0.5 cm) plastic scintillator, and thick TKE (15 cm) plastic scintillator, may be used to distinguish different elements, i.e. proton number Z. The energy loss per thickness ($\frac{dE}{dX}$) of a charged particle as it propagates through a material is proportional to Z by the relation

$$\frac{dE}{dX} \propto \frac{mZ^2}{E}, \tag{5.9}$$

where m and E are the ion's mass and energy. The Z^2 component provides favorable separation for $Z = 7 - 9$, and therefore, the oxygen isotopes from fluorine or nitrogen.

The energy measurements that were used to differentiate between various elements were the ion-chamber energy loss, the thin ΔE 0.5 cm plastic scintillator energy loss, and the thick TKE plastic scintillator which measured the remaining kinetic energies. All three energies were calibrated and corrected for the flight paths of the ions as described above. Two sets of identification plots were made and they are shown in Fig. 5.4. The plot on the left shows the ion-chamber energy loss versus the ΔE scintillator energy loss. The plot on the right of Fig. 5.4 shows the energy loss sum of the ion-chamber and thin scintillator against the total energy measurement. The total energy was determined from a sum of all three energy measurements including the TKE scintillator energy. There are no neutron requirements in these plots and therefore, the un-reacted ^{26}F beam shows up as the strongest distribution. This clearly identifies the $Z = 9$ fluorine elements and ensures a proper energy calibration. The resolution of the energy detectors is good enough to separate the $Z = 8$ oxygen isotopes

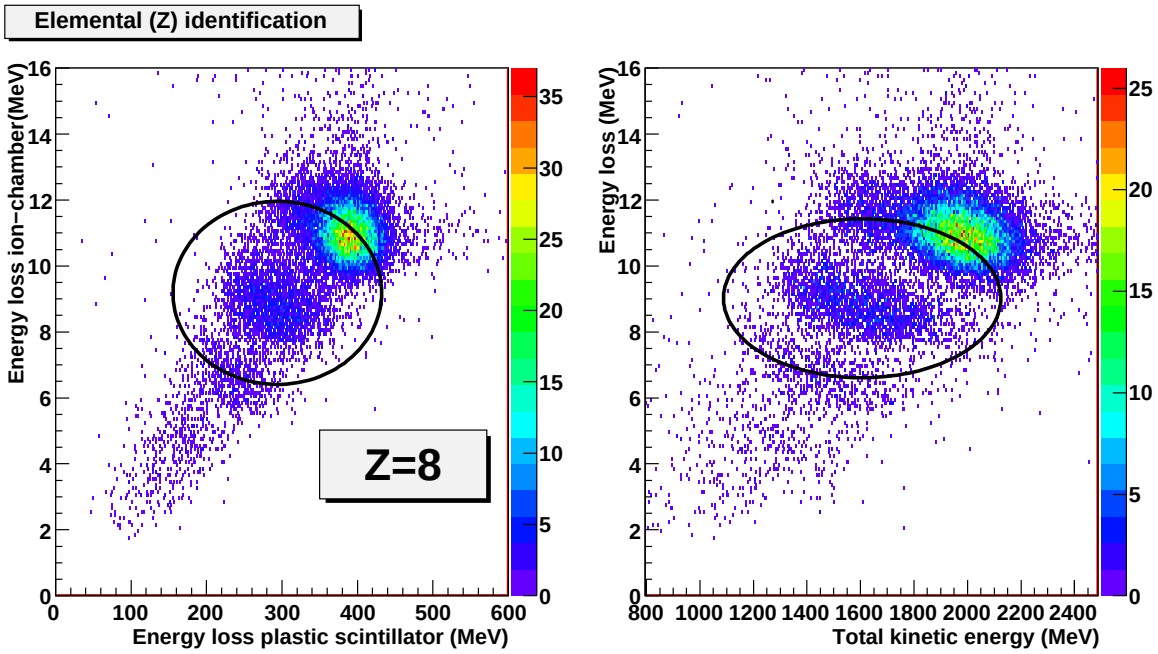

Figure 5.4: Element identification of fragments detected in the focal plane of the Sweeper dipole magnet by their energy loss and total kinetic energy. The plot on the left shows the energy loss through the thin ΔE plastic scintillator versus the energy loss through the ion-chamber. The plot on the right shows the sum of the two energy loss measurements (ion chamber and thin plastic scintillator) plotted against the total kinetic energy (sum of ion-chamber and both the thin and thick plastic scintillators). The largest number of counts shows the location of the un-reacted ^{26}F beam ($Z = 9$) with the oxygen isotopes located below ($Z = 8$).

below $Z = 9$ as can be seen in Fig. 5.4. Gates were applied to each spectrum to select only the oxygen $Z = 8$ isotopes.

In principle, isotopic separation should be possible from these energy loss spectra since the energy loss is proportional to mass m, as is shown in equation 5.9. Furthermore, the total kinetic energy should provide mass separation as it is proportional to $\frac{1}{m}$. Because of the limited acceptance of the Sweeper magnet, the $B\rho$ for all of the fragments that make it to the focal plane can be considered constant $B\rho = C$. Using equation 5.8, the relation for the velocity becomes

$$v = \frac{Cq}{m} \tag{5.10}$$

with C as a constant. Inserting this equation into the classical expression for the total kinetic

energy we arrive at

$$E = \frac{1}{2}mv^2 = \frac{1}{2}m\frac{C^2q^2}{m^2} \propto \frac{1}{m} \tag{5.11}$$

showing the $\frac{1}{m}$ dependence for the energy.

However, the resolution of the energy measurements, even with corrections for the flight paths of the ions through the detectors, is not adequate to identify mass 24 from 23, i.e. ^{24}O from ^{23}O. The lack of isotopic identification is apparent in Fig. 5.4 as separate distributions do not show up inside the black $Z = 8$ gates. Therefore, a separate procedure involving the fragment's times-of-flight had to be implemented.

5.3.3 Isotopic Separation

A clean isotopic selection of the $Z = 8$ oxygen isotopes is crucial to the decay reconstruction. Since the energy loss information did not provide enough resolution for isotopic selection, a time-of-flight (ToF) method was implemented. The foundations of the method are the same as those described above for the secondary beam identification. The Sweeper magnet selects only fragments of nearly constant rigidity and therefore the various $\frac{m}{q}$ ratios have different velocities. This is pointed out by equation 5.8. The velocity of the fragments is determined through their times-of-flight as they move from the timing scintillator at the secondary target position to the thin ΔE plastic timing scintillator located after the Sweeper dipole magnet. The straight line trajectory for this flight is 4.33 m, resulting in a ToF for the central track ^{24}O fragments ($B\rho \approx 3.8$ Tm and v=11.36 ns) of $\sim$38 ns.

Looking at the raw ToF spectrum for the oxygen elements in bottom portion Fig. 5.5, we see no clear isotopic separation at all. Furthermore, in the 2-D spectra, plotting the dispersive angle of the fragments as the leave the Sweeper magnet and the total kinetic energy each against the raw ToFs, again the different isotopes of oxygen are not defined.

The lack of separation is due to the various flight paths that recoil fragments may take when traversing the Sweeper magnet and the overall distance to the thin ΔE timing scintillator. The recoil fragments exit the secondary target at various angles due to their angle straggling in the target as well as small momentum kicks from the knock-out reaction and neutron decay. Therefore they are injected into the dipole magnet at various angles, causing many fluctuations in their flight-paths. The calculation of the times-of-flight for these fragments then is not enough to properly determine their velocity. However, measured angle

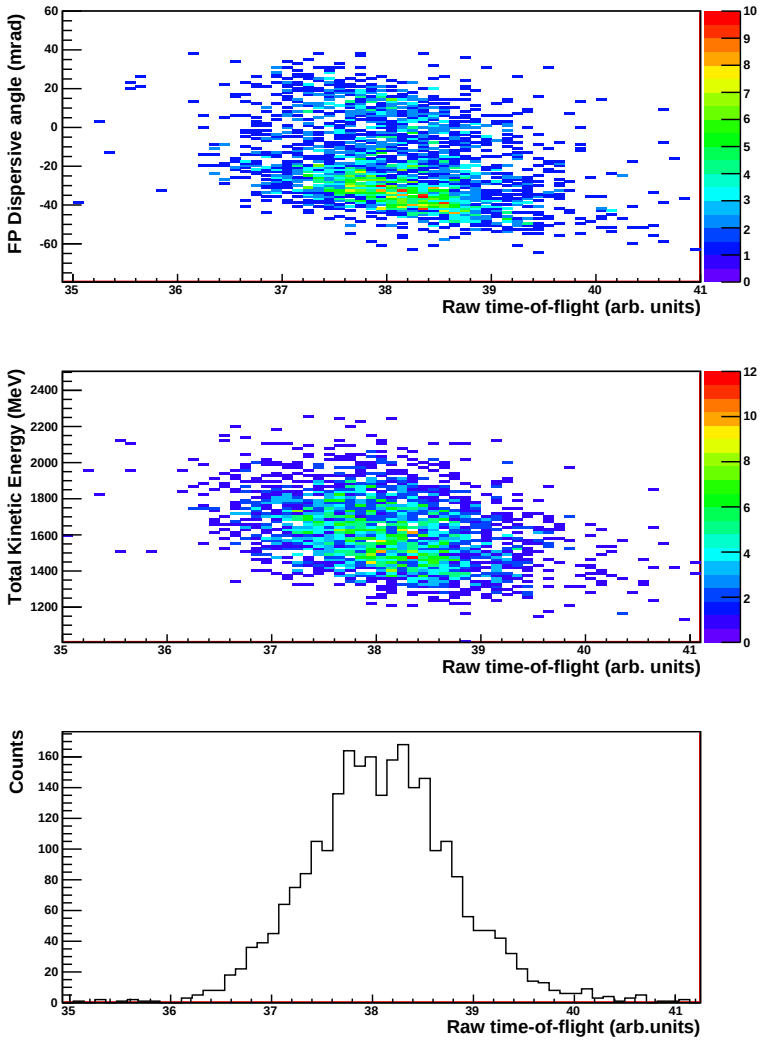

Figure 5.5: The raw time-of-flight (ToF_{raw}) for only oxygen $Z = 8$ recoil fragments from the target scintillator to the thin ΔE scintillator is shown in the bottom figure. ToF_{raw} is also plotted against the measured dispersive angle in the focal plane (top) and the total kinetic energy (middle). These show the lack of separation for the oxygen isotopes because of the variations in the fragments flight paths between the timing detectors.

Table 5.1: A table listing the parameters of the adjusted time-of-flight.

Parameter	Coefficient	Description
Afp	60	Dispersive angle in the focal plane
Afp^2	-0.25	2^{nd} order dispersive angle in the focal plane
Xfp	-3.5	Dispersive position in the focal plane
Xfp^2	-0.6	2^{nd} order dispersive position in the focal plane
Xta	40	Dispersive position at the target
Yta	20	Non-dispersive position at the target
D_{flight}	0.25	Flight path in the focal plane

and position information gathered by the two cathode-readout drift chambers and the beam tracking PPAC detectors can be used to adjust the measured time-of-flight to compensate for the flight path differences. Most crucial to the ToF adjustments are the dispersive angles (Afp) and positions (Xfp) of the observed fragments as they leave the Sweeper magnet. These two values were included to second order in the adjustment. The other components were included only to first order and they include, the total flight distance of the fragment after the Sweeper magnet and the dispersive target position of the ^{26}F beam. All of these components had a weight parameter that was adjusted to optimize the separation of the oxygen isotopes. The adjusted time-of-flight equation with the final parameter values was

$$\begin{aligned} ToF_{adj} = ToF_{raw} + 60 \cdot Afp - 0.25 \cdot Afp^2 - 3.5 \cdot Xfp \\ -0.6 \cdot Xfp^2 + 40 \cdot Xta + 20 \cdot Yta + 0.25 \cdot D_{flight}, \end{aligned} \tag{5.12}$$

where the descriptions of the parameters are given in Table 5.1.

To correctly determine the parameters for each measurable, the adjusted ToF was plotted against each parameter individually in a 2-D spectrum. All the parameters used for the $Z = 8$ oxygen isotopic separation are given in Table 5.1. The clean identification of the ^{24}O and ^{23}O isotopes is shown in the 2-D plots of Fig. 5.6. The 1-D adjusted time-of-flight (TOF_{adj}) spectra, reflecting equation 5.12, is shown in the bottom left portion of Fig. 5.6. The adjusted ToF is shown plotted against the total kinetic energy (TKE) (top left), the dispersive angle at the target (top right), and the dispersive angle in the focal plane (bottom right), in the 2-D spectra of Fig. 5.6. Clearly observed is the separation between the $A = 23$ and 24 masses, identified by the labels in the 1-D adjusted ToF spectrum shown in the bottom left

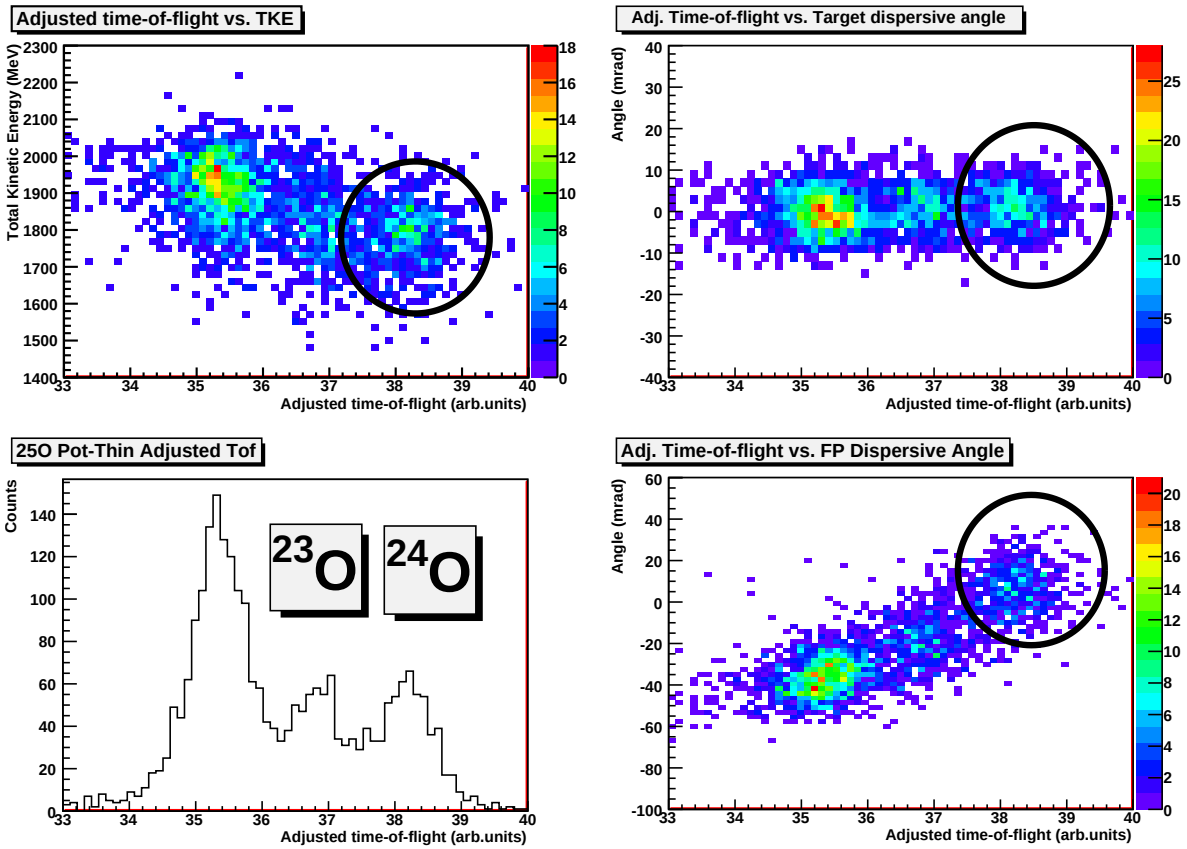

Figure 5.6: The isotopic identification of the oxygen $Z = 8$ isotopes. The fragments adjusted times-of-flight (TOF_{adj}) are plotted against the total kinetic energy (top left), dispersive angle at the target (top right), and dispersive angle in the focal plane (bottom right). The projection of all the 2-D spectra results in the 1-D adjusted TOF_{adj} spectra, shown in the bottom left figure. The ^{24}O and ^{23}O fragments are cleanly identified in the 1-D and 2-D spectra. The black circle shows a typical gate that would be placed to select the ^{24}O fragments for a coincidence measurement.

picture of Fig. 5.6. The black circles in each 2-D spectrum of Fig. 5.6 also identify the ^{24}O fragments for each case.

Now that the isotopes are clearly separated, they must be identified by their masses m. The identification of ^{24}O over ^{23}O can be made by looking at the total energy (TKE) versus the adjusted ToF 2-D spectrum. Shown by equation 5.11 the TKE is proportional to $\frac{1}{m}$ so the lowest distribution on the plot represents the heaviest mass. With ^{24}O being the heaviest bound oxygen isotope [6, 7, 14, 36, 37, 39] their is no concern for a mis-identification as no

other oxygen isotopes survive the flight to the thin ΔE detector. This results in the isotopic identification of ^{24}O,^{23}O and ^{22}O fragments in the focal plane. As an independent check of these identifications, the ^{22}O+n coincidences were analyzed and the previously observed ∼45 keV resonance in ^{23}O [46] was indeed reproduced.

5.3.4 Fragment Momentum Four-Vector

The decay fragment four-vector must also be reconstructed to determine the decay energy of the initial state. Therefore, the fragments' positions and angles at the target must be reconstructed, and two tracking techniques are needed to accomplish this. They are a forward tracking of the secondary beam particles onto the reaction target and the inverse tracking of the fragments back through the Sweeper dipole magnet to the secondary target. The need for the forward tracking is described below.

The Dipole Sweeper magnet was constructed to have a large-gap (> 10 cm) to allow for the relatively free passage of decay neutrons [17]. This large gap creates a problem for the reconstruction of the magnetic field of the magnet due to inhomogeneous fields and significant gradients. Because of this, special care was taken in mapping out its field and the program COSY infinity [62, 63] was used to create ion-optical matrices to represent these fields to 3^{rd} order. Furthermore, the dipole Sweeper magnet had no other focusing magnets and therefore the beam was run in focused mode. However, radioactive secondary beams have large position spreads, as was the case with ^{26}F, $\sigma_{x,y} \sim 2$ cm as is shown in the bottom left of Fig. 5.7. The target dispersive (x) position then can not be simply neglected when creating an inverse ion-optical matrix as is done by COSY infinity. A novel partial inverse matrix technique was developed to reconstruct the fragment trajectories using the measured dispersive position of the ^{26}F beam at the target [19]. The result is a FWHM of $\sim$ 1.5% for the reconstructed distributions over the $\sim$ 4% value found from the COSY infinity reconstruction.

Secondary Beam Tracking

A key component to the partial inverse matrix technique is the input of the target position of the fragment. This position can be estimated by using the forward tracked position of the ^{26}F secondary beam. This was done by tracking the ^{26}F from the two parallel-plate avalanche chambers (PPACs) though the quadrupole triplet magnets located before the

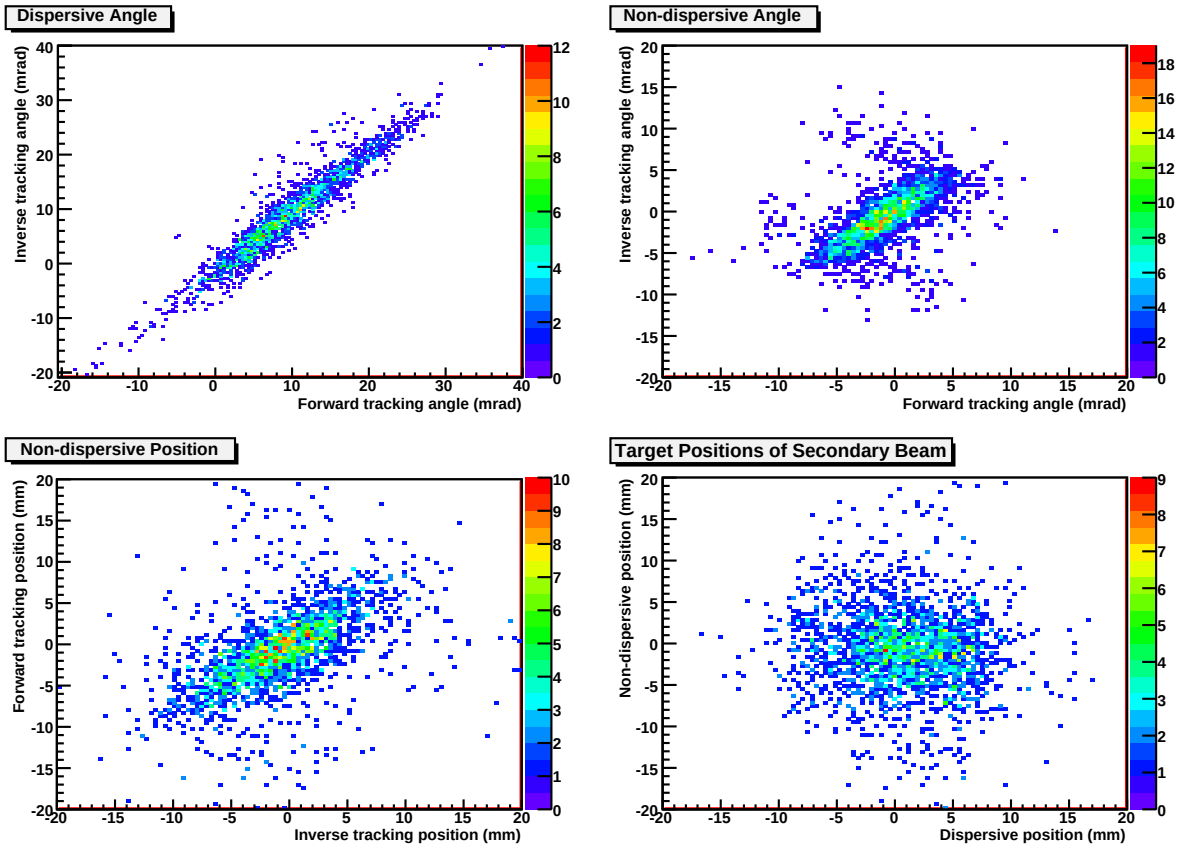

Figure 5.7: The forward tracking of the ^{26}F beam is plotted against the inverse tracking of the ^{26}F beam for the dispersive angle (top left) as well as the non-dispersive position (bottom left) and angle (top right). There is no target in place for this data so the beam is un-disturbed as it travels from the beam pipe to the focal plane. The reconstruction should be exactly 1:1, however resolutions and non-perfect tracking causes the spread around the 1:1 lines. Also shown in the bottom right plot is the ^{26}F beam profile that has been tracked to the target position. The dispersive position was used as an input for the inverse tracking [19, 20].

target position. An ion-optical matrix that describes the path of the beam ions through the triplet was developed and it relates the measured positions and angles from the PPACs to the target by

$$\begin{pmatrix} x \\ \theta_x \\ y \\ \theta_y \\ \delta \end{pmatrix}^{Target} = M_{forward} \begin{pmatrix} x \\ \theta_x \\ y \\ \theta_y \\ \Delta L \end{pmatrix}^{PPAC} \tag{5.13}$$

where the x and y represent the horizontal and vertical positions, and θ_x and θ_y are the horizontal and vertical angles. ΔL is the path length of the ion through the magnetic field and δ is given by

$$\delta = \frac{E - E_\circ}{E_\circ} \tag{5.14}$$

with E being the energy of the fragment and $E_\circ$ being the central track energy of the magnet.

Using the measured angles and positions of the secondary ^{26}F beam found from the two PPACs as inputs, the properties at the target were determined with a FWHM$\approx$ 1 mm. The forward tracked x and y positions for the beam are shown in the bottom right plot Fig. 5.7.

Inverse Fragment Tracking

The reconstruction of the fragments' four-vectors is made complicated by the large-gap acceptance and hence, irregular magnetic field of the dipole (Sweeper) magnet. To create a matrix that is possible to transform the measured properties of the fragments after the Sweeper magnet back to the target, the magnetic field was carefully probed along the central track. Then taking a Fourier transformation of the central track the three-dimensional magnetic field outside of the mid plane is calculated. The only problem is that the mapped mid plane field has to be extrapolated to places that could not be measured. The program COSY infinity [62, 63] was also used for this.

The ion-optical matrices that COSY creates from the determined magnetic field for the dipole Sweeper magnet relate a particle of particular energy, charge and mass to properties either before the magnet to after it or vice-versa. There is a forward map created which has the same relations as given for the forward tracking of the secondary beam (eq. 5.13. However, also created by COSY is an inverse ion-optical matrix which related the properties of the fragments in the focal, i.e. CRDC measurements, back to the target position. This would be fine except that the inverse matrix of COSY assumes a focused beam and takes the dispersive position at the target to equal zero. This is not the best assumption for a radioactive beam having a $\sigma_{x,y} \sim 2$ cm as mentioned above. This led to the creation of a new partial inverse map which used the ^{26}F beam position, determined by the forward tracking as described above, as input to the matrix. The details of the creation procedure of the new inverse matrix from the forward matrix of COSY are described in detail in Refs. [19, 20].

The final relation between the focal plane observables and the target parameters is given by

$$\begin{pmatrix} \theta_x \\ y \\ \theta_y \\ \delta \\ \Delta L \end{pmatrix}^{Target} = M_{Inverse} \begin{pmatrix} x \\ \theta_x \\ y \\ \theta_y \\ x^{Target} \end{pmatrix}^{CRDC} , \tag{5.15}$$

where $CRDC$ represents the measurable parameters in the focal plane (i.e. the inputs) and $Target$ shows the parameters to be calculated.

The δ parameter represents an accurate measurement of the fragment energy to be used as input into equations 3.5 and 3.6 to determine the decay energy. Also, the positions and angles of the fragments at the target are used with the same values from coincident neutrons to determine the opening angle for the decay, also needed in equations 3.5 and 3.6 to calculate the decay. The reconstructed resolution varies for different fragments because of their different rigidities and, hence, their population of different phase spaces. The FWHM energy resolution for the ^{24}O fragments was 0.9 MeV/u and for the ^{23}O fragments was 1.07 MeV/u. The FWHM angle resolutions for ^{24}O and ^{23}O were 6.6 mrad and 9.2 mrad, respectively. The reconstructed fragment kinetic energies for ^{24}O fragments and ^{23}O fragments that had a coincidence with a neutron are shown in Fig. 5.8. To ensure that the forward and inverse tracking techniques were correct in their calculations, the full technique was performed for the secondary beam with no target in place. In this scenario a 1:1 relation should be present for the incoming and out going parameters if the reconstruction were perfect. However, with the resolutions of the detectors and the no-perfect reconstruction, the 2-D plots should be spread around the 1:1 line. Indeed this is apparent in the 2-D plots of Fig. 5.7. Here the angles and vertical position for the forward tracking to the target are plotted versus the same parameters but inversely tracked to the target.

5.3.5 Neutron Momentum Four-Vector

The full neutron four-vector must be reconstructed in order to calculate the invariant mass of the original state. To accomplish this, the energy and momentum of neutrons emanating from the target were measured using the Modular Neutron Array (MoNA) [60] as a time-of-flight (ToF) position sensitive neutron detector. By determining the flight path of the neutron from the target as well as the amount of time it took to traverse that distance, the energy and momentum may be determined.

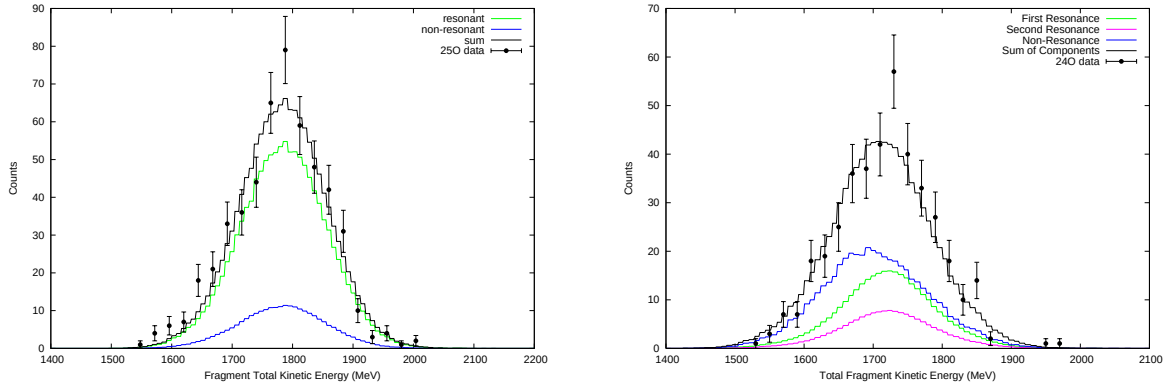

Figure 5.8: The calculated fragment kinetic energies, using the novel partial inverse tracking technique [19, 20], are shown for both ^{24}O+n data (left) and ^{23}O+n data right by the black data points with their statistical uncertainties. The lines are the same kinetic energies but determined from the Monte Carlo Simulation ST-mona.

The horizontal (X), vertical (Y), and longitudinal (Z) positions all need to be determined for a single neutron. The horizontal position was obtained by taking the calibrated time difference between the photo-multiplier tube (PMT) signals from each end of a single MoNA bar ($10 \times 10 \times 200$ cm^3). Using this method a FWHM resolution of 7.5 cm was achieved. The vertical and longitudinal directions were both determined by the physical location of the MoNA bar that was hit. The bars were arranged in a 16x9 rectangle with adjacent bars touching, therefore, when a single bar had adequate signals in both PMTs its location could be calculated. The plastic bars of MoNA are 10×10 cm^2 in the Y and Z directions causing an uncertainty of ± 5 cm for each position measurement. Neutron positions measured by MoNA are shown in Fig. 5.9 for ^{24}O+n coincidence data.

The kinetic energy of the neutrons can be determined using the distance of the neutron from the target and by the time-of-flight (ToF) between the target timing scintillator and the time of the first interaction of the neutron at MoNA. The start time of the ToF comes from the 0.253 cm plastic scintillator located $\sim$6 cm before the secondary Be target. The stop time is the average time of the first two simultaneous PMTs from a single neutron bar. This ToF has been calibrated using the known velocity and flight distance of γ-rays from the reaction target as was described above. The calculation of the neutron kinetic energy

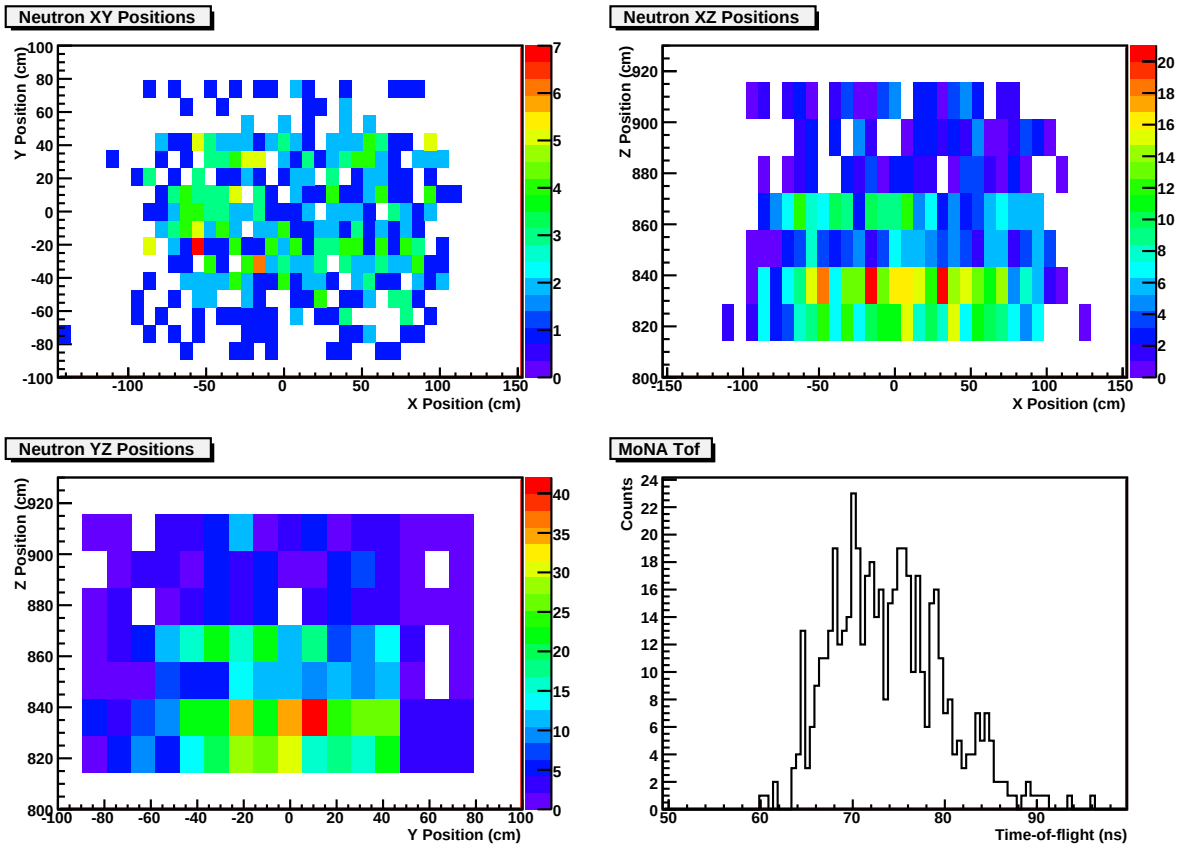

Figure 5.9: The positions of neutrons that were detected by the Modular Neutron Array (MoNA) for ^{24}O+n coincidence data. The data shows the X-Y (top left), X-Z (top right), and Y-Z (bottom left) 2-D spectra. The neutron time-of-flight spectra for ^{24}O+n coincidence data is shown in the bottom right for the first neutron interaction inside MoNA.

from the observed ToF and flight path is done using relativistic equations. The velocity of the neutron is

$$\mathrm{v} = \frac{D}{ToF} \tag{5.16}$$

where D is the distance from the target to the interaction inside MoNA. The energy calculation from the velocity follows the expressions:

$$\beta = \frac{\mathrm{v}}{c} \tag{5.17}$$

$$\gamma = \sqrt{\frac{1}{1-\beta^2}} \tag{5.18}$$

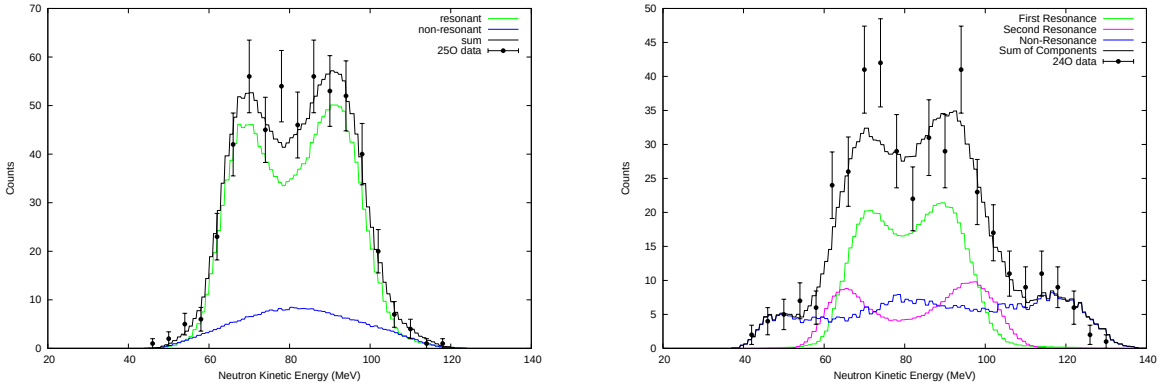

Figure 5.10: The calculated neutron kinetic energies, using the prescription described above, are shown for both ^{24}O+n data (left) and ^{23}O+n data (right) by the black data points with their statistical uncertainty. The lines show the results of the calculated kinetic energies from the Monte Carlo Simulation ST-mona.

The neutron kinetic energy KE is now determined with the neutron rest mass M_n

$$KE = M_n(\gamma - 1) \tag{5.19}$$

The angle, kinetic energy, and rest mass information for the neutron are now all available, completing the four-vector reconstructed. The reconstructed neutron kinetic energies that have a coincidence with either an ^{24}O fragment or an ^{23}O fragment are shown in Fig. 5.10. The four-vector components of a coincident fragment must now be determined to combine with the neutron's and be inserted into equations 3.5 and 3.6 to calculate the invariant mass and decay energy.

5.3.6 Total Reconstruction

The full reconstruction of both the neutrons and the fragments provides all of the components necessary to reconstruct the invariant mass of neutron unbound states using equations 3.5 and 3.6. The neutron and fragment kinetic energies used to reconstruct the decay energy have been shown in Figs. 5.10 and 5.8. The relative angle between the coincident neutron and fragment in the laboratory frame, may be found on an event-by-event basis. This relative angle, needed for the reconstruction of the decay energy, is shown in Fig. 5.11. The relative

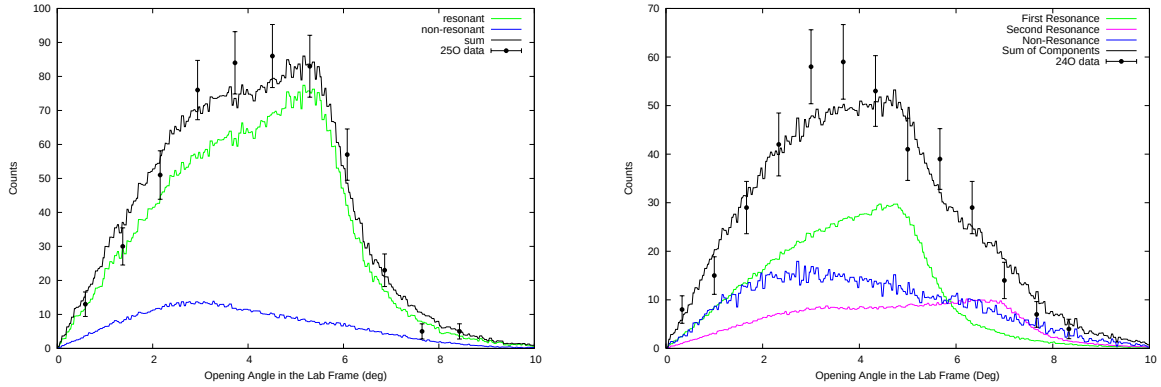

Figure 5.11: The relative decay angle in the laboratory frame for ^{24}O+n (left) and ^{23}O+n (right) coincidence data is shown by the data points with their statistical error bars. The lines shown the calculated values for the angle from the Monte Carlo Simulation ST-mona.

decay energy is reconstructed for neutrons in coincidence with either an ^{24}O fragment or and ^{23}O fragment. The experimentally observed relative decay spectrum for the ^{25}O decay and for the ^{24}O, are shown in top and bottom of Fig. 5.12, respectively.

The top plot shows the ∼400 ^{24}O+n coincidence events, the middle plot shows the ∼300 ^{23}O+n coincidence events and the bottom plot shows the ∼1000 ^{22}O coincidence. These experimental plots have not been corrected in any way. They are all affected by the experimental resolutions and acceptance cuts. The three plots do show some resonance type structures that must be investigated. To accomplish this, the experimental response must be understood so as to extract only the true physical properties of any resonant states.

5.4 Monte Carlo Simulation

The observed decay spectra are hampered by experimental resolutions and acceptances. To extract useful physics information from these spectra, a simulation package was developed to reflect the experimental response and analysis techniques. This software package, ST-mona [15], uses Monte Carlo methods to simulate decay events. These events are then analyzed in the same manner as the experimental data so that the two may be directly compared. Details of the simulation, components and usage are given below, as well as in [15, 18, 20].

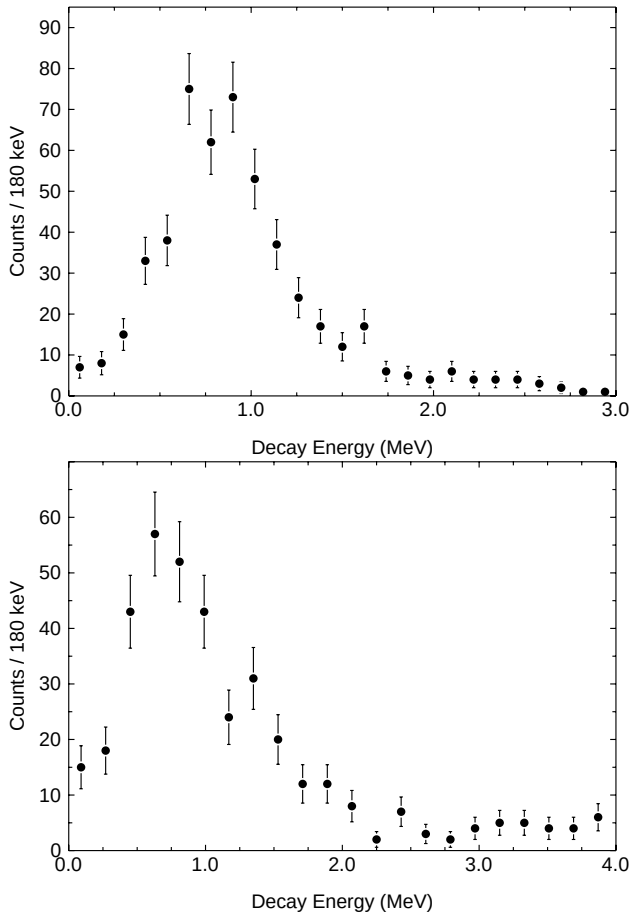

Figure 5.12: The reconstructed relative decay energy spectra for coincidence ^{24}O+n (top) and ^{23}O+n (bottom) events are shown by the black data points with their statistical uncertainties. The spectra were calculated using the invariant mass equations of 3.5 and 3.6.

The simulation included all of the geometrical acceptances of the experimental setup. Most crucial to the resolution were the neutron acceptances at MoNA. Also very important are the recoil fragment acceptances through the Sweeper magnet and the acceptances of the detectors in the focal plane. A Gaussian smearing was included for resolutions of the beam-line PPACs and the CRDCs. Also, Gaussian distributions for the timing resolution for each scintillator were also included. The FWHM resolutions for all of the detectors are shown in Table 5.2. Furthermore, a Glauber reaction model was used to describe the knock-out reactions by the target. This provided random momentum kicks to the fragments. The angular straggling of the recoil fragments as they moved through the remainder of the

Table 5.2: A table listing the resolution parameters and inputs into the ST-mona Monte Carlo simulation.

Parameter	σ (Units)
Beam Energy Spread	-0.025 (MeV/u)
Target Resolution	0.0007 (cm)
Time Resolution	0.3 (ns)
CRDC Position Resolution	0.001 (mm)
CRDC Angle Resolution	0.0013 (mrad)
MoNA X Position Resolution	0.08 (m)
MoNA Y and Z Position Resolution	0.05 (m)
Input Dispersive Position	0.005 (m)
Input Dispersive Angle	0.009 (m)
Input Non-Dispersive Position	0.004 (m)
Input Non-Dispersive Angle	0.0035 (m)

target was also incorporated into the simulation. Finally, any effects that the scattering of a neutron inside MoNA may have on the position resolution of the neutrons was simulated by GEANT3 [64] and also included in the calculations.

The final resolution of the entire experimental response was determined by fitting the FWHM of a delta function decay at various decay energies. In Fig. 5.13 the FWHM functions for the experimental response for the ^{25}O decay (inset left) and the ^{24}O* decay (inset right) are both shown. These functions are proportional to the square-root of the decay energy ($\sqrt{E_{decay}}$), where the decay energy is in keV. For the decay of ^{25}O (^{24}O+n events) the resolution as a function of decay energy was FWHM= $17\sqrt{E_{decay}}$ and FWHM= $40\sqrt{E_{decay}}$ below and above $\sim$1 MeV respectively. The cause for the abrupt increase in resolution is because at $\approx$ 1 MeV perpendicularly decaying neutrons are beginning to be missed by MoNA. The resolution for the ^{24}O decay was FWHM= $41\sqrt{E_{decay}}$. Also shown in Fig. 5.13 are the delta function decays at three different relative decay energies for each (0.1 MeV, 0.75 MeV and 1.5 MeV). The delta function was used as the input distribution into the ST-mona simulation. Therefore, the widths of these states is purely from the experimental resolution. These were calculated at a number of different decay energies and those widths were used to determine the FWHM resolution function. Because the experimental setup was optimized for an ^{25}O decay, the ^{24}O resolution and acceptance are slightly worse. This is

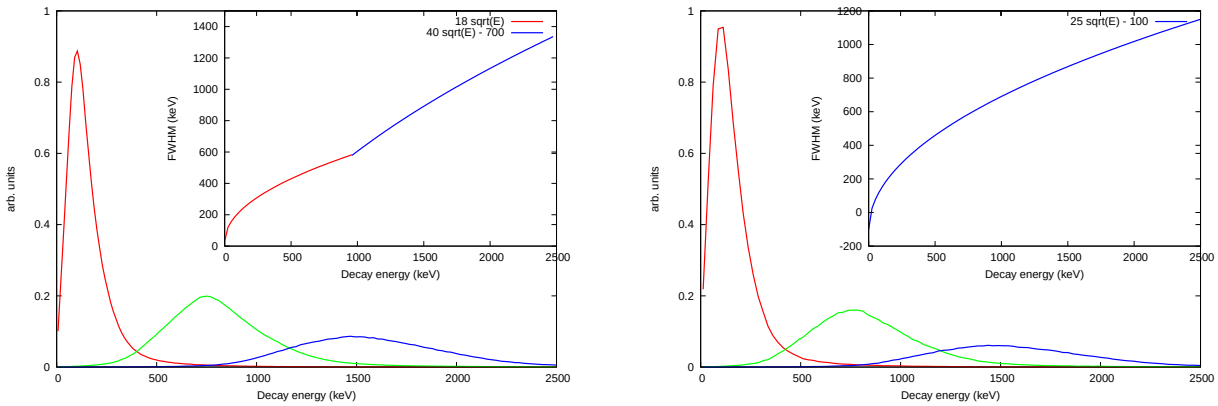

Figure 5.13: The FWHM resolution functions are given for the decay of ^{25}O (inset left) and the decay of ^{24}O* (inset right). They are FWHM= $17\sqrt{E_{decay}}$ and FWHM= $40\sqrt{E_{decay}}$ below and above ∼1 MeV respectively for the ^{25}O decay and FWHM= $41\sqrt{E_{decay}}$ for the ^{24}O decay. Also shown are three different relative energy decays (0.1 MeV, 0.75 MeV and 1.5 MeV) which have widths comprised of solely the experimental resolution as delta functions were the input decay distributions.

mainly due to the fragment acceptance through the Sweeper magnet and the fact that the decay fragments (^{23}O) were off of the central track $B\rho$ of the magnet.

5.4.1 ST-mona Simulation Procedure

The simulation used the experimental distributions of the secondary beam at the target as input. These distributions were then used to calculate the positions and angles of the nucleon removal reaction inside the target. For the ^{26}F removal reactions, a sudden approximation is implemented in the simulation to account for the knock-out of a single proton in the ^{25}O case, or possibly multiple nucleons in the ^{24}O case. The decay of the parent nucleus into a fragment plus a neutron is nearly instantaneous; therefore still occurring within the target. The distribution of the decay is determined by the user. Three different distributions were included for this analysis. The Breit-Wigner single level distribution (see eq. 3.8 in chapter 3) was included to describe resonances. Maxwellian and Gaussian distributions (eqs. 3.28 and 3.29, also described in chapter 3) were included to simulate the non-resonance contributions to the decay spectrum.

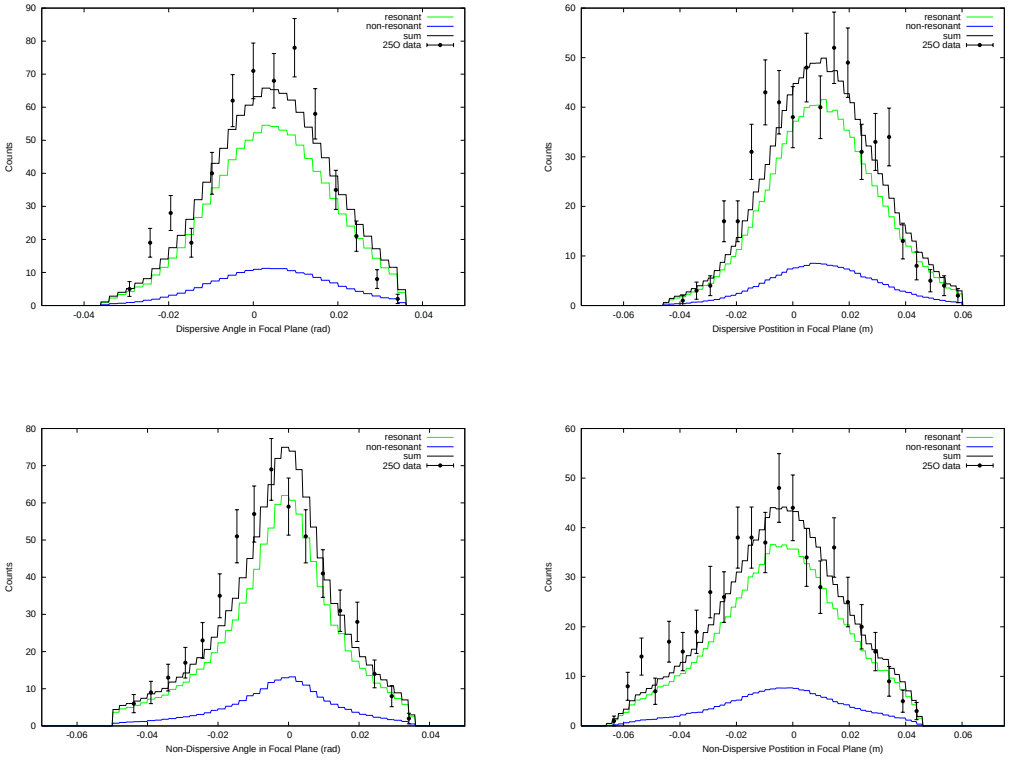

Figure 5.14: The measured dispersive angles (top left) and positions (top right) and non-dispersive angles (bottom left) and positions (bottom right) of ^{24}O fragments that have a coincidence with a neutron are shown by the data points with their statistical error bars. The solid black line is the total sum of the simulated data from the Monte Carlo simulation ST-mona [15]. As can be seen, all of the observables are very well reproduced by the simulated data.

The fragments are forward tracked through the dipole Sweeper magnet using the forward ion-optical matrix created by COSY. This produces simulated data in the focal plane in the same way as the experimental data that was observed. The forward map used is the same as described above which was inverted to allow for inverse tracking of the particles. To check the correctness of the forward map and the acceptance and resolution inputs of the simulation, the dispersive and non-dispersive angles and positions for the simulation are overlaid with the experimental data in Fig. 5.14 and in Fig. 5.15.

The neutrons that are simulated in the decay events are transformed to the position of MoNA. These simulated events are compared to the experimental measurable neutron data

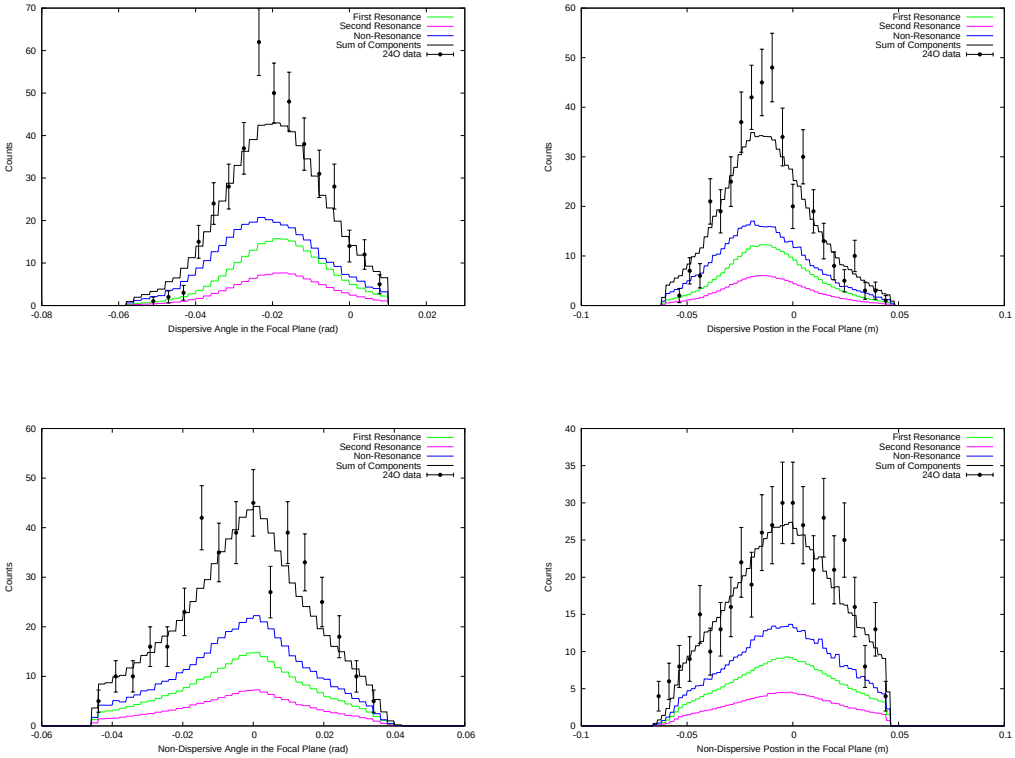

Figure 5.15: The data and the simulation are the same as in Fig. 5.14 except that it is for ^{23}O fragments in the focal plane that have a neutron in coincidence.

as well. Fig. 5.16 shows the dispersive positions of measured neutrons at MoNA and the simulated events for the same observables. With all of these first order observables, the four-vectors for the neutrons and fragments are then calculated from the simulated data. The analysis pipeline for all of the simulated data is identical to that of the experimental data, so a direct comparison is warranted. Using the simulated data, the second order parameters are calculated and the simulated results are overlaid with the measured data as is for the kinetic energies in Fig. 5.8 and the laboratory angle in Fig. 5.11. The relative velocity spectra, which are calculated by the difference between the scalar velocities of a fragment-neutron pair, are also very well reproduced, as is shown in Fig. 5.17.

These excellent representations of the experimental data reflect the understanding of the experimental response as the simulated data reproduces all of the measured data. With this very good handle on the experimental response, the invariant mass and decay spectra

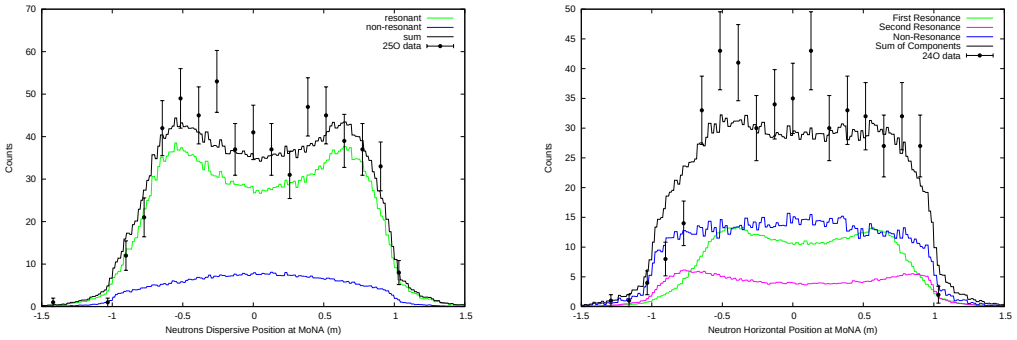

Figure 5.16: The observed horizontal positions of neutrons detected by MoNA that are in coincidence with an ^{24}O (left) or ^{23}O (right) fragment, are shown by the black data points. The Monte Carlo ST-mona simulated data is also shown on the same figures, for the same parameters, by the solid black lines.

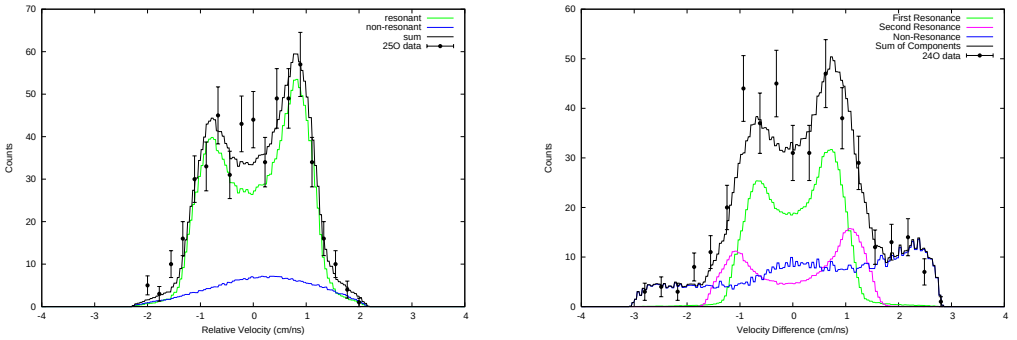

Figure 5.17: The experimental relative velocities, determined by the velocity difference between coincidence fragments and neutrons, are shown for ^{24}O+n (left) and ^{23}O+n (right) coincidences by the black data points with their statistical uncertainties. The simulated data is shown by the solid black line, which reproduces the observed data very well. The components of the simulated data from ST-mona will be discussed in chapter 6.

for the measured resonances may be simulated and compared directly with the data. The final simulated decay spectra, which include Breit-Wigner resonance line-shapes and non-resonance line-shapes as described in chapter 3, are fit to the experimental decay spectra to extract properties such as decay energy and resonance width. This was carried out by allowing all of the parameters of the Breit-Wigner and the non-resonance line-shape to very and adopting a goodness-of-fit minimum chi-squared (χ^2) procedure.

CHAPTER 6

RESULTS

6.1 Ground State Mass of ^{25}O

The simulated data produced by ST-mona [15] was shown in chapter 5 to reproduce the experimental measurements for all of the components needed to reconstruct the ^{25}O decay spectrum (see Figs. 5.8, 5.10, 5.11, 5.14, 5.16,and 5.17). This confidence in understanding the experimental response allows for the invariant mass decay spectrum for the ^{24}O+n coincidence data to be fit by simulated line-shapes. The decay spectrum for the ^{25}O ground state, shown in Fig. 5.12, appears to have a single resonance structure. Therefore, a single-level Breit-Wigner line-shape will be used to describe the resonance contribution to the data. The derivation of the Breit-Wigner line-shape was given in chapter 3 and the final form of the function (eq. 3.8) is given again here;

$$\sigma_l(E) \propto \frac{\Gamma_l(E)}{(E_{\text{decay}} + \Delta_l(E) - E)^2 + \frac{1}{4}\Gamma_l(E)^2}. \tag{6.1}$$

The width $\Gamma_l(E)$ depends on the decay energy and the orbital angular momentum by $\Gamma_l(E) = 2P_l(E)\gamma^2$. $P_l(E)$ is the penetrability function and is comprised of the Bessel functions for a neutron decay. The shift function also depends on the Bessel functions and the orbital angular momentum as $\Delta_l(E) = -(S_l(E) - B(E))$. $B(E)$ is value of the boundary condition, set so that $\Delta_l(E) = 0$ when $E = E_{\text{decay}}$, the resonance energy. Also, the interaction (channel) radius was found from eq. 3.11, with $A_1 = 24$ and $A_2 = 1$, so $a \sim 5$ fm. Variations on either of the boundary conditions were found to have effects less than the resolution of the experimental system. See chapter 3 for further details and derivations of the aforementioned values and expressions. The resonance energy E_{decay}, width $\Gamma_l(E_{decay})$, and amplitude of the Breit-Wigner function are all free parameters. The orbital angular momentum (l), is also a parameter of the Breit-Wigner equation. All of the parameters (E_{decay}, Γ and the amplitude)

may be determined by a minimum chi-squared (χ^2) fitting procedure. However, for the decay of ^{25}O$\rightarrow^{24}$O+n, the orbital angular momentum l may be determined by investigating the single-particle structure of ^{25}O and ^{24}O, along with a few simple theoretical arguments.

6.1.1 Theoretical Background

The lowest single-particle proton structure of ^{25}O consists of $Z = 8$ protons filling the lowest three $s-p$ orbitals ($(0s_{1/2})^2(0p_{3/2})^4(0p_{1/2})^2$). $Z = 8$ is a traditional magic number as the next orbital ($0d_{5/2}$) is high in energy. The single-particle neutron structure has 17 neutrons filling all orbitals up to the $0d_{3/2}$ level, plus a single neutron sitting above the predicted $N = 16$ shell gap ($(0s_{1/2})^2(0p_{3/2})^4(0p_{1/2})^2(0d_{5/2})^6(1s_{1/2})^2(0d_{3/2})^1$). The sd orbitals that are filled by the neutrons for the ground states of ^{25}O and ^{24}O, are shown in Fig. 6.1. To predict the ground state total angular momentum (spin) and parity of ^{25}O, the unpaired protons and neutrons are investigated. Since the protons are an even number ($Z = 8$), they couple to the lowest energy possible, a spin-parity of $J^\pi = 0^+$. The same happens for the lowest $N = 16$ neutrons. Therefore, the unpaired neutron in the $\nu 0d_{3/2}$ orbital provides the ground state spin of the nucleus in the independent single-particle model. The total angular momentum of the state is $J = 3/2$. The parity of the state is related to the orbital angular momentum by $\pi = (-1)^l$. With the final unpaired neutron in a d–wave state of $l = 2$, the parity is positive. The result is a ground state spin-parity of $J^\pi = 3/2^+$ for ^{25}O. The simple single-particle prediction is confirmed by more sophisticated shell model calculations using the USD [13], USD05a [27] and SDPF-M [11] interactions. Each of these predict a $3/2^+$ ground state spin-parity, and no nearby states that compete in energy.

With the ^{25}O ground state spin-parity inferred, the orbital angular momentum l, needed for the Breit-Wigner function for the decay neutron, may be suggested. The ^{25}O($3/2^+$) ground state decays to the ^{24}O (0^+) ground state by the emission of a single neutron. A schematic of the single-particle structure for this decay is shown in Fig. 6.1. The single neutron decay path is the only decay path that is observed in this experiment as there are no bound excited states in ^{24}O [9].

The neutron decay process must conserve total angular momentum (spin) J, where $J = l \pm s$. s is the intrinsic momentum of the neutron and l, the orbital angular momentum of the neutron. The intrinsic spin value for a neutron is 1/2. The conservation of momentum

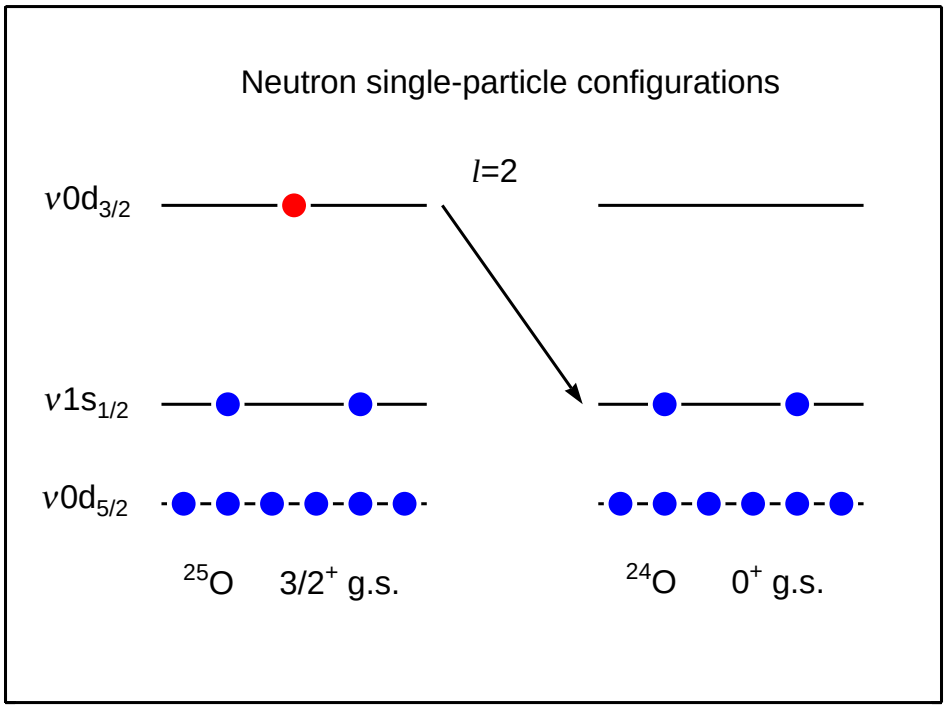

Figure 6.1: The neutron single-particle structure for the ground states of ^{25}O and ^{24}O, are shown for the *sd* orbitals. The $l = 2$ neutron decay of ^{25}O $(3/2^+)$ to ^{24}O (0^+) is depicted by the arrow. The orbital angular momentum assumed for this decay is the only value allowed inside the *sd* shell.

looks like

$$J_f - J_i = \Delta J = \frac{3}{2} = l \pm \frac{1}{2} \tag{6.2}$$

for the ^{25}O ground state decay to the ^{24}O ground state decay. Therefore, l may only have values of either 1 or 2. Since we have already determined above that the neutron is in the *d*–wave state with $l = 2$, and there is no change in parity between the two states in the decay $(3/2^+ \rightarrow 0^+)$, then the neutron must have orbital angular momentum $l = 2$. This parameter may now be set for the Breit-Wigner line-shape 6.1 used in the χ^2 fitting procedure of the invariant mass spectrum.

The use of a single-level Breit-Wigner distribution of $l = 2$, which infers an isolated single resonance with little interference from nearby states, for the description of the ground state

Table 6.1: A table listing the occupation numbers for neutrons in particular *sd* shell orbitals for the ground states of ^{25}O and ^{24}O [1, 2].

^{25}O ($3/2^+$)				^{24}O (0^+)			
Interaction	$0d_{5/2}$	$1s_{1/2}$	$0d_{3/2}$	Interaction	$0d_{5/2}$	$1s_{1/2}$	$0d_{3/2}$
USD	5.889	1.957	1.154	USD	5.786	1.909	0.305
USD05a	5.917	1.977	1.107	USD05a	5.836	1.953	0.211
USD05b	5.931	1.976	1.093	USD05b	5.865	1.950	0.185

resonance of ^{25}O, is supported by the calculated particle configurations of the initial and final ground states. The ^{25}O ground state is calculated to have a wave function dominated by a configuration of a closed proton $Z = 8$ shell $(0s_{1/2})^2(0p_{3/2})^4(0p_{1/2})^2$ and one neutron above the new shell gap at $N = 16$ $(0d_{3/2})^1$ [11]. The occupations for the *sd* shell orbitals for the ground states of ^{25}O and ^{24}O are shown for the USD [13] and USD05 [27] shell model interactions in Table 6.1.

For ^{25}O, the occupations of the three orbitals are consistent with the single-particle model occupations of the $0d_{5/2} = 6$, $1s_{1/2} = 2$, and the $0d_{3/2} = 1$ orbitals. Hence, the calculated occupation numbers support the use of the single-particle model. The ^{24}O ground state wave function is also dominated by a single configuration having the same closed $Z = 8$ proton shell as ^{25}O, but with a closed $N = 16$ shell for the neutrons. The occupation number for the $\nu 0d_{3/2}$ orbital in ^{24}O, as calculated by using the USD interactions, are all around 0.2. This indicates that the more dominant configuration prefers an un-occupied $\nu 0d_{3/2}$ orbital [1, 2]. There is no surprise from these occupations numbers, that the spectroscopic factor is nearly 1 for an $l = 2$ neutron decay from the $\nu 0d_{3/2}$ of ^{25}O to the ground state of ^{24}O. In fact it is greater than 0.9 for all three *sd*-shell interactions (USD,USD05a and b) [1, 2] as is shown in Table 6.2. It should be noted, that for a purely single particle ^{25}O ground state the spectroscopic factor for the $\nu 0d_{3/2}$ orbital would be unity because only a single neutron occupies that orbital. These arguments support the validity of a single Breit-Wigner line-shape with an $l = 2$ orbital angular momentum as a good representation of the ^{25}O$\rightarrow^{24}$O+n decay.

The non-resonance contributions to the decay spectrum were simulated by an input distribution of Maxwellian shape into the decay energy distribution for ST-mona. The description

Table 6.2: A table of the spectroscopic factor S, between the initial ground state $J^\pi = 3/2^+$ in ^{25}O and the 0^+ ground state in ^{24}O.

Initial J^π	Orbital nl_j	S	Interaction
$3/2^+$	$0d_{3/2}$	0.904	USD
$3/2^+$	$0d_{3/2}$	0.942	USD05a
$3/2^+$	$0d_{3/2}$	0.945	USD05b

of this distribution was given in chapter 3, and its final form given by equation 3.28. The Maxwellian distribution of beam velocity neutrons had two variables; temperature T and amplitude. They were both free parameters of the fit to the experimental data. The choice of the Maxwellian distribution to reproduce the non-resonance data was two-fold. First, it was found to reproduce the decay distributions for mixed and random events. Second, the shape of the relative velocity curve, which was very sensitive to the input decay distribution, was well reproduces by the Maxwellian distribution of beam velocity neutrons. This excellent reproduction of the relative velocity data is shown on the left side of Fig. 5.17.

6.1.2 Single-level Breit-Wigner Fit

The fit of the simulated data, comprised of both the resonance Breit-Wigner distribution and non-resonance Maxwellian distribution, to the observed ^{24}O+n decay spectrum, was carried out. A χ^2 value was computed for each variation of the free parameters. There were 19 degrees-of-freedom in the fit, 25 data points and 6 free fit parameters. A minimum χ^2 value of 15.1 was found for resonance parameters of $E_{\text{decay}} = 770^{+20}_{-30}$ keV and $\Gamma = 172(30)$ keV. The optimum temperature for the Maxwellian distribution was $T = 1.75$ MeV. The minimum reduced chi-squared value was $\chi^2_{red} = 0.8$. The best fit to the measured data points is shown by the solid black line in Fig. 6.2. The total sum for the simulation is comprised of a resonance (red, dotted line) Breit-Wigner component and a non-resonance (blue, dashed line) Maxwellian distribution component. The ratio of the resonance to non-resonance contribution to the spectrum is 3.25:1 as determined by the ratio of their amplitude coefficients. Fig. 6.3 shows the 1 and 2 σ limits for the χ^2 values with a dependence on the decay energy E_{decay} and the width Γ. The Maxwellian temperature T was minimized at each point along the contour. The uncertainties in the energy and width measurements

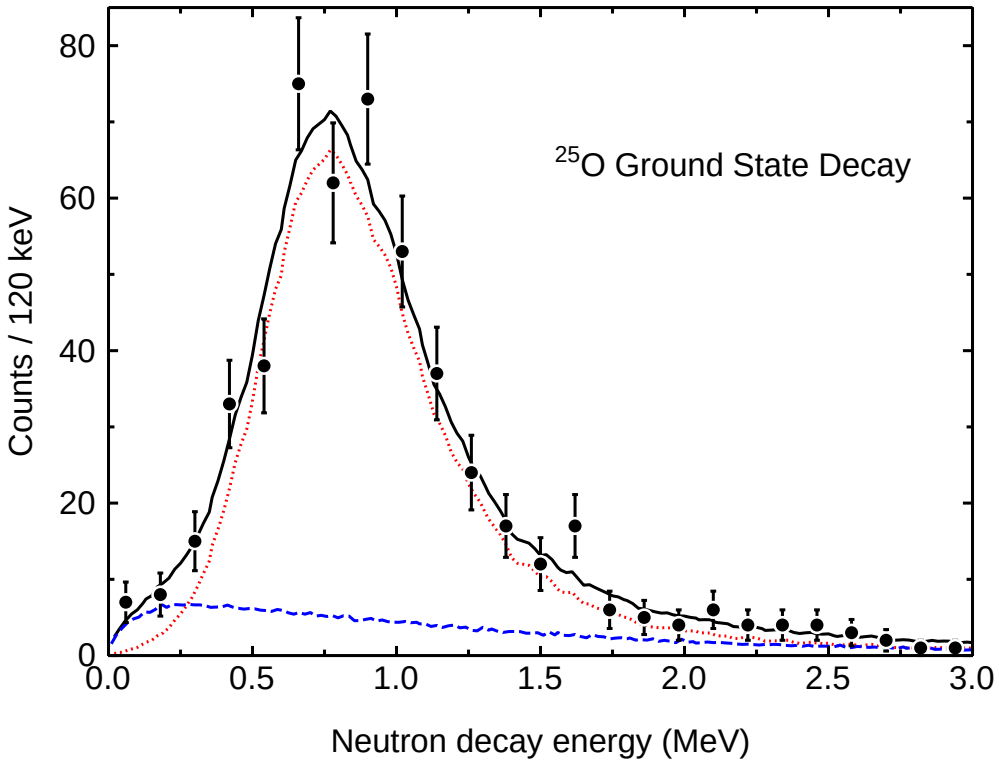

Figure 6.2: The reconstructed relative decay energy for ^{25}O is shown by the black data points with their statistical uncertainty. The solid black line shows the simulated line-shape composed of both a resonant (red, dotted) ($E_{decay} = 770^{+20}_{-30}$ keV and $\Gamma = 172(30)$ keV, $l = 2$) and non-resonant (blue, dashed) contribution (ratio 3.25:1).

reflect only the statistical 1 σ limits from the χ^2 fit. There may be systematic uncertainties arising from the simulated data or other areas. The systematic uncertainties have not been included. Table 6.3 shows the optimum values for all of the fit parameters with their statistical uncertainties.

As was shown extensively in chapter 5 the simulated data reproduced the observed data on all levels. The simulated data that was shown in Figs. 5.8, 5.10, 5.11, 5.14, 5.16,and 5.17, all have the same components as the decay spectrum (Fig. 6.2). They all have the same ratio of resonance to non-resonance contribution as well, again, solidifying that the simulation reproduces all experimental data well and brings confidence to the parameters extracted from the fit of the invariant mass decay spectrum.

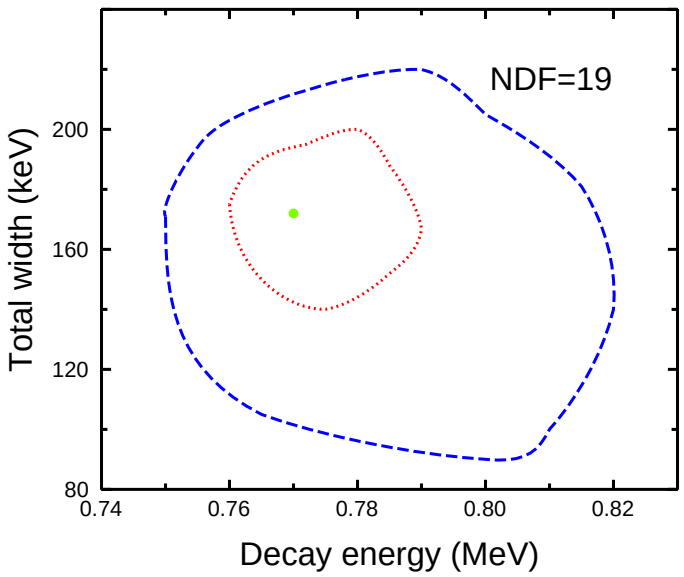

Figure 6.3: The minimum chi-squared χ^2 contour plot for the fit of the simulated data of ST-mona to the experimental data for the invariant mass decay spectra as a function of decay energy E_{decay} and width $\Gamma_l(E_{decay})$. The dot represents the minimum χ^2 value (16.1) and the red and blue contours show the 1 and 2 σ limits.

Table 6.3: A table listing the optimum parameters from the fit of the simulated data to the observed decay spectrum for the ^{25}O$\rightarrow^{24}$O+n decay.

Parameter	Optimum Value (Statistical Uncertainty) Units
Decay Energy (E_{decay})	770^{+20}_{-30} keV
Width ($\Gamma(E_{decay})$)	172(30) keV
Orbital Angular Momentum (l)	2
Temperature (T)	1.75 MeV
Amplitude of Resonance	3.25
Amplitude of Non-resonance	1

6.1.3 Ground State Mass of ^{24}O

The ground state mass (binding energy) of ^{25}O can be found from the measured decay energy, the ground state binding energy of ^{24}O, and the rest mass of a neutron. The equation may be found from the expression for the decay energy (eq. 3.6)

$$E^* = \sqrt{s} - M_f - M_n = M_{^{25}O} - M_{^{24}O} - M_n. \tag{6.3}$$

$M_{^{25}O}$, $M_{^{24}O}$, and M_n are the rest masses of the ground states of ^{25,24}O and a neutron. With some manipulation of the above equation we have,

$$M_{^{25}O} = E_{\text{decay}} + M_{^{24}O} + M_n. \tag{6.4}$$

The decay energy measured in the present work gives a value of $E_{\text{decay}} = 0.77^{+0.02}_{-0.03}$ MeV, and the rest mass of a neutron is known to be $M_n = 939.565346$ MeV [65]. All that remains to include in expression 6.4 is the rest mass of the ground state of ^{24}O. Since most mass measurements work in terms of the mass excess, it is useful to give that expression here in units of MeV,

$$M_{EX}(\text{MeV}) = M(\text{MeV}) - A(u) \cdot amu(\text{MeV/u}). \tag{6.5}$$

M is the total binding energy of the nucleus, A is the number of nucleons in the nucleus, and amu is the atomic mass unit ($amu = 931.494028$ MeV/u [65]).

Recently an experiment was carried out which measured and re-measured a number of nuclei in the mass 20–40 region [24]. The experimental technique used was a time-of-flight measurement, combined with a high-resolution energy-loss spectrometer. From this work, a mass excess of 18.50(11) MeV was measured and a mass excess of 18.6(1) MeV was adopted for ^{24}O. The adopted value was calculated by the weighted average of the measurement and the previously adopted value of the 2003 Atomic Mass Evaluation (AME) [25]. The 2003 AME value was determined from three independent measurements [21, 22, 23], each made using a direct time-of-flight technique. The measured values for each ^{24}O ground state binding, and the adopted values, are shown in Fig. 6.4. The solid line in the figure represents the most recently adopted value of Ref. [24].

The newly accepted value of Ref. [24] is 470 keV lower than the previously accepted value of the 2003 AME (19.70(24) MeV) [25]. Investigating all of these mass measurements for the ground state binding energy of ^{24}O revealed that there was a single anomalous observation [23] that skewed the 2003 AME value. Since the recent measurement agrees with the

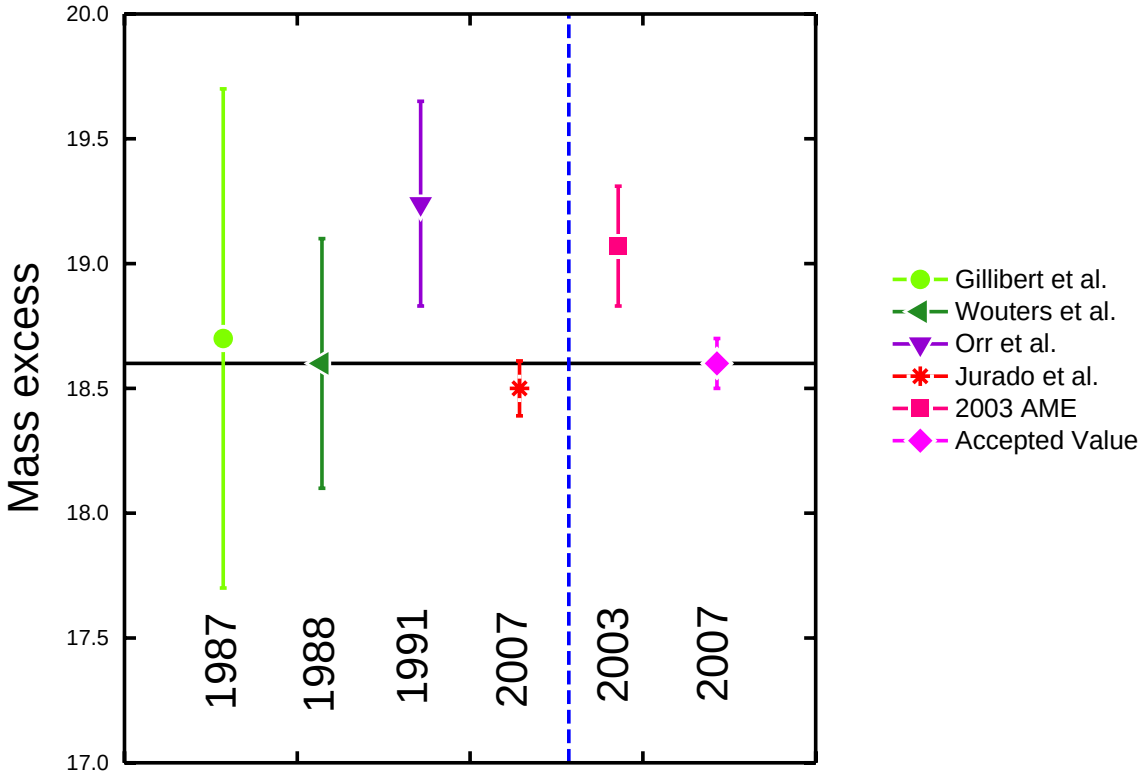

Figure 6.4: The experimental mass excess (eq. 6.5) measurements are shown for the ground state of ^{24}O on the left side of the figure by the year they were measured [21, 22, 23, 24]. The value accepted by the Atomic Mass Evaluation of 2003 [25], and the recently adopted value of Ref. [24] (the adopted value for this work), are shown on the right side of the figure. The solid line also shows the recently accepted value of Ref. [24].

majority of the previous measurements, and has less uncertainty than all others, it suggests that this is the most reasonable value. The adopted value of Ref. [24] (18.6(1) MeV)has also been accepted in this work for the calculations and comparisons of all of the experimental data. It should be noted that the presently accepted value does include the anomalous value [23] in the calculation of the ^{24}O mass excess through the average with the 2003 AME value.

The ^{24}O ground state mass excess can now be used to calculate the total ground state

binding energy of ^{25}O. Using equation 6.4, the total binding energy of the ^{25}O ground state was calculated to be $M_{^{25}O} = 23314.79$ MeV. This correlates to a mass excess of $M_{EX} = 27.44(11)$ MeV using equation 6.5.

6.1.4 Size of the $N = 16$ Shell Gap

An estimation of the experimental shell gap between the $\nu 0d_{3/2}$ and $\nu 1d_{1/2}$ orbitals ($N = 16$) may be determined using the measured ^{25}O ground state binding energy. First, one must assume a closed $(0p - 0h)$ ground state configuration for ^{24}O with the neutrons filling the $1s_{1/2}$ orbital. Then the single-particle energy for the $\nu 0d_{3/2}$ orbital may be determined by the energy difference between the closed ^{24}O core and the one neutron state [53]. The one neutron state in this case is the $N = 17$ ground state of ^{25}O, the current measurement. Therefore, the energy difference between the ^{24}O and ^{25}O ground state binding energies, $\epsilon 0d_{3/2} = 770^{+20}_{-30}$ keV, is in fact the single-particle energy for the $\nu 0d_{3/2}$ orbital. It should be noted, that in this notation, an unbound orbital will have positive energy and a bound orbital will have a negative energy. In the same manner, a single neutron hole state ($N = 15$) for the closed ^{24}O core can estimate the single-particle energy of the $\nu 1s_{1/2}$ orbital [53]. The energy of the neutron hole state comes from the ground state binding energy of ^{23}O. The difference between the energies of the ^{24}O ground state and the ^{23}O ground state, gives the $\nu 1s_{1/2}$ orbital energy. This energy is $\epsilon 1s_{1/2} = -4.09(13)$ MeV. The size of the $N = 16$ shell gap is the difference in energy between the two single-particle orbitals, $gap_{N=16} = \epsilon 0d_{3/2} - \epsilon 1s_{1/2} = 4.86(13)$ MeV. The single-particle energies and the estimation of the $N = 16$ shell gap at the oxygen drip line are shown by the black data points in Fig. 7.1 with their uncertainties.

6.1.5 ^{25}O Neutron Separation Energies (S_n and S_{2n})

To understand the location of the oxygen drip-line, the energy of the $\nu 0d_{3/2}$ orbital will become of extreme importance. Observables that reflect this energy very well are the neutron separation energies. These measurable values provide the amount of energy needed to remove a one (S_n) or two (S_{2n}) neutrons from a nucleus. The equations for the neutron separation energies of ^{25}O are given by

$$S_n = M_{^{25}O} - M_{^{24}O} - M_n, \tag{6.6}$$

$$S_{2n} = M_{^{25}O} - M_{^{23}O} - 2M_n. \quad (6.7)$$

M represents the ground state binding energies and the rest mass of a neutron (M_n = 939.565346 MeV [65]). The ground state binding energies of ^{23}O and ^{24}O are known (see discussion above for the ground state binding energy of ^{24}O) [25, 24]. The binding energy of ^{25}O has been determined in this work ($M_{^{25}O}$ = 23314.79 MeV). Since the ground state of ^{25}O is unbound to both one– and two–neutron decay, the separation energies will be positive. Looking at equation 6.6, we see that this value is in fact the experimental decay energy as expressed in equations 3.6 and 6.4. Therefore, the ^{25}O one–neutron separation energy is S_n=770^{+20}_{-30} keV. The two–neutron separation is calculated from the ground state binding of ^{23}O, S_{2n} = 3.33(13) MeV.

6.2 Excited States of ^{24}O

Similar to the ^{24}O+n coincidence data in the decay of the ^{25}O ground state, all of the ^{23}O+n measurable parameters needed for the ^{24}O* decay were well reproduced by the simulated ST-mona data (see Figs. 5.8, 5.10, 5.11, 5.15, 5.16,and 5.17). Therefore, the ^{24}O* invariant mass spectrum may be fit with confidence. The resonance features of this fit will be described by a Breit-Wigner line-shape. This line-shape has the same free parameters of decay energy E_{decay}, width Γ, amplitude, and orbital angular momentum l, as in the ^{25}O resonance fit. Also, as was the case with the ^{25}O decay, the values for the orbital angular momentum l may be constrained if a theoretical investigation of the ^{24}O* decay to the ground state of ^{23}O, is undertaken.

6.2.1 Theoretical Background

^{24}O has 8 protons and 16 neutrons and with a normal filling of the nuclear shells, this leads to a closed $Z = 8$ $\pi 0p_{1/2}$ shell and a closed $N = 16$ $\nu 1s_{1/2}$ orbital. Assuming that this single particle configuration dominates the ground state of ^{24}O, a possible lowest excited single-particle configuration may result from the promotion of a neutron from the $1s_{1/2}$ orbital across the $N = 16$ shell gap into the $\nu 0d_{3/2}$ orbital. This leaves a neutron hole in the $\nu 1s_{1/2}$ orbital and an unpaired neutron in the $\nu 0d_{3/2}$ orbital. The single-particle structure for this configuration is shown, along with the decay of the unbound neutron, in Fig. 6.5. The coupling of the unpaired neutron to the neutron hole gives possible spin-parity values

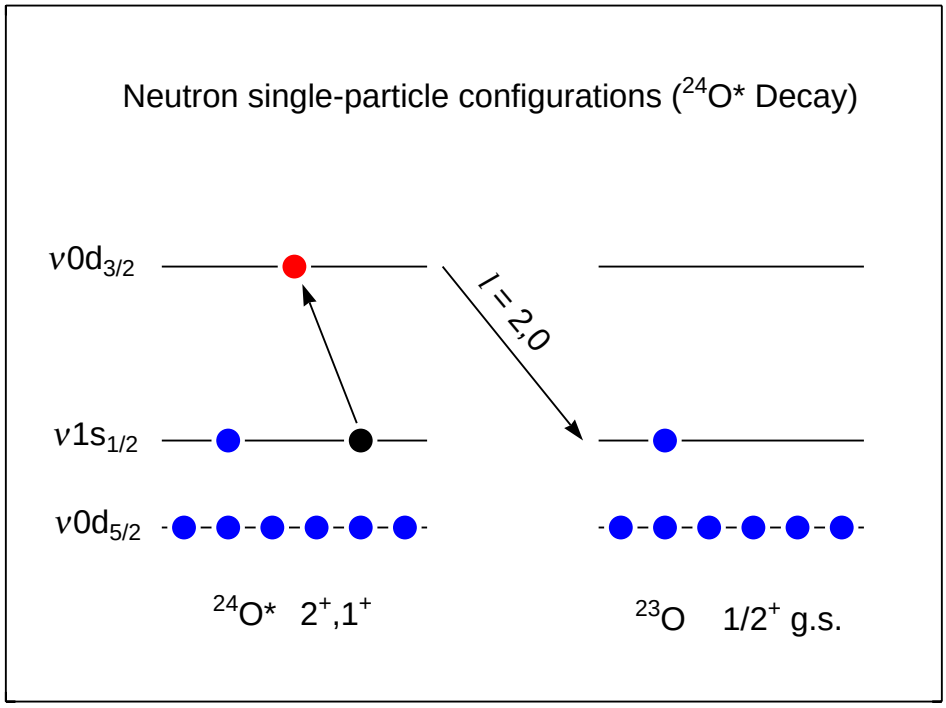

Figure 6.5: The single-particle neutron configuration for the lowest excited states in ^{24}O is shown on the left side of the figure. This configuration has a single, excited neutron (red circle), from the $\nu 1s_{1/2}$ orbital raised into the $\nu 0d_{3/2}$ orbital, leaving a hole (black circle) in the $\nu 1s_{1/2}$ orbital. The coupling of these two states results in spin-parities of $J^\pi = 2^+, 1^+$. The unbound neutron is allowed to decay to the ground state of ^{23}O ($1/2^+$ [26]), with either orbital angular momentum $l = 2$ or 0.

of $(1s_{1/2})^1 \otimes (0d_{3/2})^1 \rightarrow J^\pi = 1^+, 2^+$ as $|J_{max} - J_{min}| \leq J \leq |J_{max} + J_{min}|$. Another possible configuration for the lowest excited states may come from a neutron in the $\nu 1p_{3/2}$ or $\nu 0f_{7/2}$ orbitals, giving rise to spins states of $J^\pi = 1^-, 2^-, 3^-$ or 4^-. However, these do not seem as likely as the neutron must be promoted above the $N = 20$ (although possible reduced) shell gap. Therefore, this work has assumed the 2^+ and 1^+ states to lie lowest in energy.

These first two excited states in ^{24}O must be unbound to neutron decay because no evidence was found for a γ decaying state (i.e. bound state) by a recent experiment [9]. The excited states of ^{24}O must decay by a neutron to states in ^{23}O. ^{23}O was also found to lack a bound excited state, as none were found during the same search for states in ^{24}O [9]. Therefore, by detecting a neutron in coincidence with an ^{23}O fragment, it is known for certain that the excited state must have decayed to the known $1/2^+$ ground state in ^{23}O [26].

Applying the same arguments that were used in the ^{25}O decay, mainly conservation of total angular momentum J, we see that confined to the *sd* single-particle shell space, the 2^+ state must decay via a neutron with an $l = 2$ orbital angular momentum. The 1^+ state may decay by neutrons of either *s*-wave ($l = 0$) or *d*-wave ($l = 2$) nature (Fig. 6.5). This simple picture, already limits the values of the orbital angular momentum. These orbital angular momentum assumptions can be supported and further constrained by modern theoretical calculations, including many-body shell model calculations.

There are a number of predictions available for the first excited state(s) in ^{24}O [13, 27, 11, 2, 29]. These calculations include both standard shell model Hamiltonians [13, 27, 11], as well as calculations which recognize the continuum explicitly [2, 29]. Each of them calculates a low lying doublet of states of spin-parity $J^\pi = 2^+, 1^+$. Also, they all predict that the 2^+ state will lie lower in energy than the 1^+ state. Therefore, if a single excited state were to be observed in the invariant mass spectrum for the ^{24}O* decay, it will most likely be the 2^+ level. The orbital angular momentum of the neutron decaying from this state would have to have angular momentum $l = 2$ (inside the *sd* shell). The energy of the first predicted negative parity states by the WBP interaction using a $1p-1h$ calculation into the fp shells, was the 1^- state more than 1.5 MeV higher in energy than the 2^+ and 1^+ states.

The spectroscopic factors between the 2^+ and 1^+ states in ^{24}O, with the ground state of ^{23}O ($1/2^+$), can give an indication of the single-particle nature of the decaying state. The spectroscopic factors are strong indicators for the likelihood that the parent states would decay to the daughter state, as it is a measure of the overlap of the wave functions of the two states. Therefore, a spectroscopic factor near unity in this case, suggests a strong overlap of the excited state in ^{24}O with the $1/2^+$ ground state of ^{23}O. Furthermore, it suggests that the state in ^{24}O is dominated by a single-particle configuration. The spectroscopic factors for the 2^+ and 1^+ states decaying to the $1/2^+$ ground state of ^{23}O, have been calculated using the USD [13] and USD05 [27] shell model interactions [1, 2]. These values are given in Table 6.4. The 2^+ state is nearly one for the $0d_{3/2}$ orbital as was expected from the simple-single particle model in the *sd* shell space. The 1^+ state is also near unity for the $0d_{3/2}$ orbital and virtually zero for the $1s_{1/2}$ orbital. This suggests that the 1^+ state does not decay with any reasonable amount via an *s*-wave $l = 0$ neutron, and indeed has a single-particle configuration similar to that of the 2^+ state. If the 1^+ state were also present in the invariant mass spectrum, then the theoretical arguments would suggest that it too decays via a neutron with angular

Table 6.4: A table of the spectroscopic factor S, between the initial states J^π in ^{24}O and the $1/2^+$ ground state in ^{23}O.

Initial J^π	Orbital nl_j	S	Interaction
2^+	$0d_{3/2}$	0.906	USD
	$0d_{5/2}$	0.014	
1^+	$0d_{3/2}$	0.887	
	$1s_{1/2}$	0.001	
2^+	$0d_{3/2}$	0.951	USD05a
	$0d_{5/2}$	0.013	
1^+	$0d_{3/2}$	0.921	
	$1s_{1/2}$	2×10^{-5}	
2^+	$0d_{3/2}$	0.945	USD05b
	$0d_{5/2}$	0.011	
1^+	$0d_{3/2}$	0.928	
	$1s_{1/2}$	6×10^{-5}	

momentum $l = 2$.

6.2.2 Non-resonant line-shape

The above theoretical arguments support the use of only an $l = 2$ orbital angular momentum for the Breit-Wigner functions used to describe the resonance features of the invariant mass spectrum. Also apparent in the decay spectrum are contributions from non-resonant components. These non-resonance contributions showup as well in the relative velocity spectrum for the ^{23}O+n coincidence data. The experimental relative velocity differences between ^{23}O fragments and their coincident neutrons are shown by the data points in Fig. 6.6. The same simulated relative velocity spectra are also shown in Fig. 6.6, where two different non-resonance input distributions (Gaussian and Maxwellian) were used with ST-mona. In the left figure the Gaussian distribution was used in the simulation and on the right side of Fig. 6.6, the Maxwellian input distribution was used. The black solid line in each is the sum of the resonance (not shown) and these non-resonance contributions (green, dash-dotted).

What can be clearly noticed is that at large relative velocity differences (less than -1.5 cm/ns and greater than 1.5 cm/ns), the total line-shape is dominated by the non-resonance contribution. Allowing the Maxwellian distribution to vary for all thermal energies

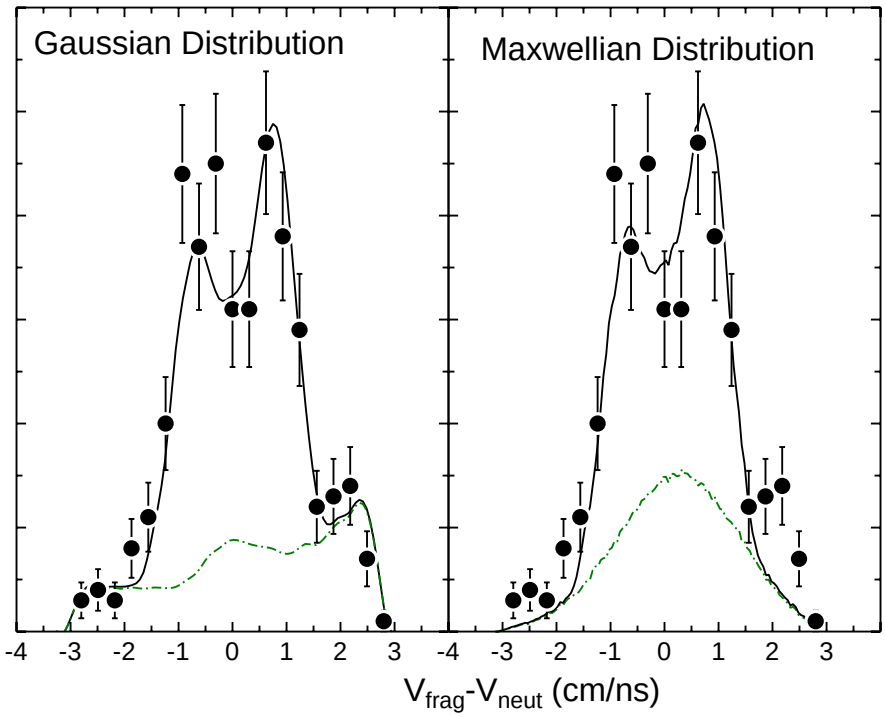

Figure 6.6: The relative velocity difference between coincident ^{23}O fragments and neutrons are shown by the black data points with their statistical uncertainties (same data as on the right side of Fig. 5.17). The lines in each figure are the simulated line-shapes from ST-mona. The solid black line is the sum of the resonance (not shown) and non-resonance (green, dot-dashed) contributions. The non-resonance contribution described by the Gaussian distribution having a central decay energy of $E = 10$ MeV and $\sigma = 5$ MeV, is shown in the left figure. The non-resonance contribution described by Maxwellian distribution of thermal energy $T = 1.75$ MeV, is shown on the right. Note the better reproduction of the data at large relative velocities (less than -1.5 cm/ns and greater than 1.5 cm/ns) by the Gaussian input distribution.

T, could not reproduce this large relative velocity region. However, the Gaussian distribution, with a central energy around $E = 10$ MeV and $\sigma = 5$ MeV, described the velocity difference spectrum very well. The Gaussian distribution overall was much better at reproducing the experimental data. Therefore, a Gaussian distribution was used to describe the non-resonance data for all of the ^{23}O+n observed spectra. It should be noted, and is shown by Fig. 6.7 that the shape of the decay distribution is not drastically affected by the choice of non-resonance distribution. Also, the variation of the central energy ($8 - 12$ MeV) and σ ($4 - 6$ MeV) of the Gaussian distribution, was found to have little effect on the shape of the

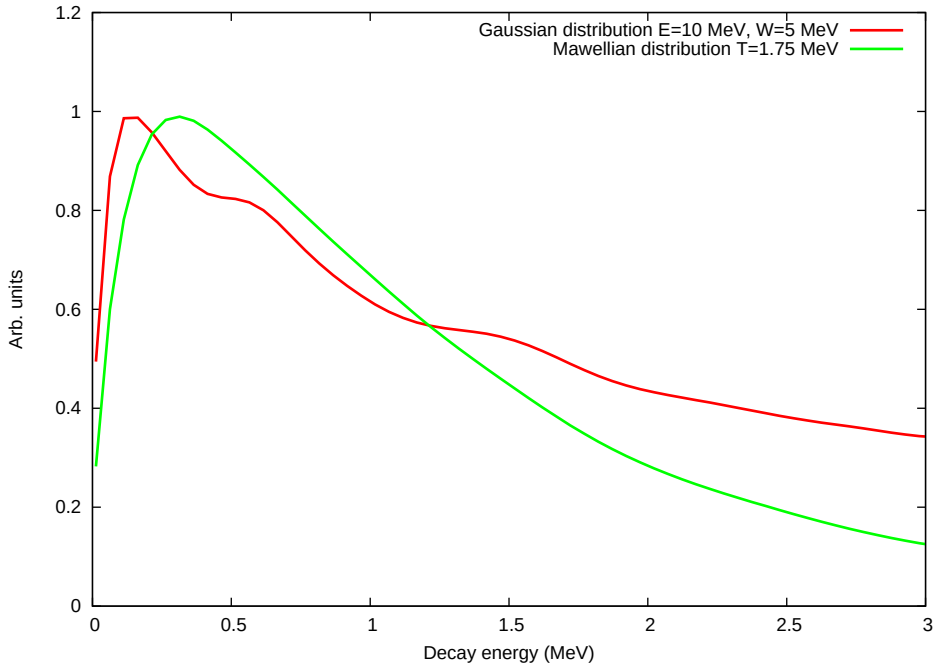

Figure 6.7: The final ^{24}O decay spectrum line-shapes for two non-resonance distributions, Gaussian (E=10 MeV, σ=5 MeV) and Maxwellian (T=1.75 MeV), are shown by the solid red and green lines respectively. These line-shapes result from the two non-resonance input distributions that are compared in Fig. 6.6, the relative velocity spectra. It should be noted that the two distributions do not have drastically difference overall line-shapes in this decay spectrum.

non-resonance contribution in decay spectrum.

The physical explanation of the large relative velocity features may come from the way that the excited states in ^{24}O are populated. Instead of the direct population of the states by a nucleon knock-out, as is the most likely case for the ground state of ^{25}O, the excited states in ^{24}O are most likely fed through the high-lying states in ^{25}O. A proton knock-out from the inner p shell of the secondary ^{26}F beam would populate continuum states in ^{25}O which are likely to decay to the excited states in ^{24}O. The large differences in relative velocities are likely remnants of these high energy statistical decays. Another, possibility is that there are high energy excited states being populated. However, due to the limited resolution of our

Table 6.5: A table listing the optimum parameters from the fit of the simulated data to the observed decay spectrum for the $^{24}O^{*} \rightarrow ^{23}O+n$ decay for a single resonance of $l = 2$ orbital angular momentum.

Parameter	Optimum Value (Statistical Uncertainty) Units
Decay Energy (E_{decay})	0.73(4) MeV
Width ($\Gamma(E_{decay})$)	$1.8^{+>2.2}_{-1.1}$ MeV
Orbital Angular Momentum (l)	2
Gaussian Central Energy	10.0 MeV
Gaussian σ	5.0 MeV
Amplitude of Resonance	3.25
Amplitude of Non-resonance	1

experimental setup these states can not be individually resolved and identified.

6.2.3 Single energy-dependent Breit-Wigner Line-Shape fit

The experimental decay spectrum for coincidence $^{23}O+n$ events was fit with a single energy-dependent Breit-Wigner line-shape of angular momentum $l = 2$. The decay energy (E_{decay}), width ($\Gamma(E)$) and amplitude, were all allowed to vary freely. A non-resonance Gaussian distribution was also included in the fit with the parameters described above ($E = 10$ MeV and $\sigma = 5$ MeV). The minimized χ^2 value was found for a resonance energy of $E_{\text{decay}} = 0.73(4)$ MeV and a width of $\Gamma = 1.8^{+>2.2}_{-1.1}$ MeV. The upper limit on the decay width reflects the lack of sensitivity the Breit-Wigner line-shape has for large decay widths. Since Γ is not equal to the FWHM, and the amplitude of the Breit-Wigner function is a free parameter, the function saturates at large width. In this case, the change in the FWHM for widths of $\Gamma \approx 4$ MeV, was minute. Add to this the large experimental resolution at the decay energy (~ 600 keV), and the change in χ^2 for different widths was minimal. Therefore, the 1 σ limit was not reached for the upper limit on Γ. The lower limit does come from the 1 σ limit from the χ^2 fit. The best fit to the data ($E_{\text{decay}} = 0.74$ MeV, $\Gamma = 1.8$ MeV) is shown in Fig. 6.8 and the optimized parameters of the minimum χ^2 fit are given in Table 6.5.

To interpret the single Breit-Wigner fit, the single-particle width for an $l = 2$ neutron at a decay energy of 0.73 MeV was calculated using equation 3.49, derived in chapter 3. Using this expression a single-particle width of $\Gamma_{sp} = 0.06$ MeV was calculated for an $l = 2$

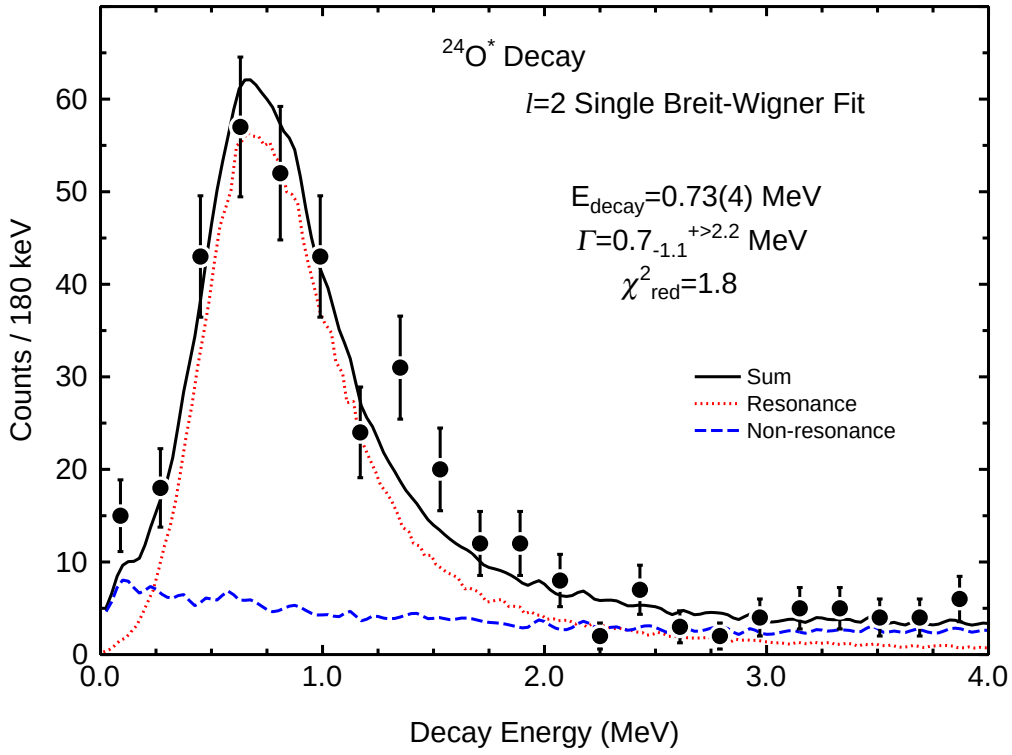

Figure 6.8: The invariant mass decay spectrum for ^{23}O+n coincidences is shown by the black data points with their statistical uncertainties. The best fit to the data for a single simulated $l = 2$ Breit-Wigner resonance (red, dotted line) and a non-resonance Gaussian distribution (blue, dashed). The minimized reduced chi-squared value was $\chi^2_{red} = 1.8$ for $E_{\rm decay} = 0.73(4)$ MeV and width $\Gamma = 1.8^{+>2.2}_{-1.1}$ MeV.

decay at 0.73 MeV. The observed width at its lower 1 σ value ($\Gamma = 0.7$ MeV) is more than an order of magnitude larger than the calculated single-particle width. One can infer a spectroscopic factor from this lower limit by taking a ratio of the observed width Γ to the single-particle width. Hence, if the state were of completely $l = 2$ single-particle nature, the spectroscopic factor would be unity, as the $0d_{3/2}$ orbital should be occupied by a single neutron. The spectroscopic factors for this transition have been calculated using the USD interactions [13, 27] and are in Table 6.4. They are all around 0.9, just slightly less than 1. This ratio for the observed width, at its 1 σ lower limit, over the single-particle width ($\frac{\Gamma}{\Gamma_{sp}}$), and hence, the experimentally observed spectroscopic factor for a single $l = 2$ state, is greater than 10. This order of magnitude difference between the observed and expected values is

Table 6.6: A table listing the occupation numbers for neutrons in particular *sd* shell orbitals for the first two excited states in ^{24}O, the 2^+ and 1^+ states [1, 2].

	2^+				1^+		
Interaction	$0d_{5/2}$	$1s_{1/2}$	$0d_{3/2}$	Interaction	$0d_{5/2}$	$1s_{1/2}$	$0d_{3/2}$
USD	5.7956	0.9899	1.2145	USD	5.832	1.0270	1.1410
USD05a	5.8326	1.0130	1.1540	USD05a	5.8738	1.0120	1.1142
USD05b	5.8444	1.0173	1.1383	USD05b	5.8833	1.0142	1.1025

very un-physical. This indicates an inconsistent fit of the line-shapes with the experimental data.

The conclusion of this comparison leads to three possible outcomes: 1) The single-particle model used is inaccurate and parameters such as the nuclear potential radius are incorrect 2) The orbital angular momentum of the Breit-Wigner fit is incorrect 3) There is more than one resonance state present in the ^{24}O* decay spectrum. The first option may be eliminated by applying a larger radius to the single-particle equation (eq. 3.49). In order to reproduce the observed width, a radius (R) of more than 7 fm would be needed. This is nearly a factor of 2 larger than has been determined from a measurement of the ^{24}O interaction cross-section ($R = 3.98$ fm) [66]. Although this large width could be the manifestation of an extended matter distribution in the ground state of ^{24}O, such an increase is beyond a realistic likelihood. The second point is also very unlikely. As mentioned previously, all theoretical predictions are consistent with a large spectroscopic factor for the $l = 2$ neutron decay (see Table 6.4). Furthermore, calculations of all kinds predict the 2^+ level to lie lowest in energy. Therefore, the most likely cause of the inconsistent comparison between the single-particle prediction and the observed width, is due to the presence of another resonance state or states in the ^{24}O* decay spectrum.

The theoretical calculations presented above also provide further support for the multiple resonance hypothesis. In particular, two resonances in the excited state spectrum result from the coupling of the $\nu 0d_{3/2} \otimes \nu 1s_{1/2}$ orbitals to produce a doublet of states with spin-parity $J^\pi = 2^+$ and 1^+ in the single-particle picture. Also, all theoretical calculations predict these two nearby low lying states [13, 27, 11, 2, 29]. The shell model calculations of the single-particle configurations for these two states [13, 11, 27] also show that they have nearly

identical configurations, as is shown by the occupations of the neutrons in their *sd* shell orbitals given in Table 6.6. Also, since their spectroscopic factors were nearly identical (Table 6.4), if one of these states were to be populated with some strength, then it is hard to understand why the other state should not be populated within the same order.

6.2.4 Two resonance line-shapes fit

The observed large decay width of the energy spectrum assuming a single resonance of orbital angular momentum $l = 2$, and the theoretical arguments presented above, have led to the proposal of a fitting of the $^{24}O^*$ decay spectrum by two independent resonances. Therefore, two single-level Breit-Wigner line-shapes and a non-resonant Gaussian line-shape were fit to the experimental data. The decay energies, widths and amplitudes, were allowed to vary for resonance contributions and the non-resonance component was the same as in the single resonance fitting (Gaussian distribution with $E = 10$ MeV and $\sigma = 5$ MeV). An orbital angular momentum of $l = 2$ was used for both resonances due the calculated spectroscopic factor of zero from the USD interactions for the $l = 0$ ($1s_{1/2}$ orbital) decay to the ground state of ^{23}O (see Table 6.4). However, it should be noted that the use of $l = 1, 3$ or 4 for the second resonance state did not effect the fit results. This is due to the increased experimental with at high decay energy, which lead to intensity in the measured width Γ.

A minimum reduced chi-squared value of $\chi^2 = 1.4$ resulted from the two Breit-Wigner fit. The resonant decay energies at the minimum χ^2 value were $E_{\text{decay}} = 0.63(4)$ MeV and $E_{\text{decay}} = 1.24(7)$ MeV for the lower and higher Breit-Wigner line-shapes respectively. The decay widths corresponding to these two decay energies were $\Gamma = 0.05^{+0.21}_{-0.05}$ MeV and $\Gamma = 0.03^{+0.12}_{-0.03}$ MeV. This best fit to the experimental data is shown in Fig. 6.9 and has a low energy resonance (dashed, blue), a high energy resonance (dotted, red), and a non-resonant (dash-dotted, green), contribution. The limits on the decay widths reflect the 1 σ range of the chi-squared fit for their upper values. The lower limits reflect the fact that they are each consistent with $\Gamma = 0$ within the 1 σ range. Because of the experimental resolution, and the increased number of fitting parameters, these decay widths were relatively insensitive at low energy. A list of the optimized parameters for the two Breit-Wigner fit is given in Table 6.7. As was mentioned above, the inclusion of a high energy resonance with $l = 1, 3$ or 4, resulted in nearly identical minimum values for the two energies and widths.

The single-particle calculations for the widths of the two resonance states at $E_{\text{decay}} =$

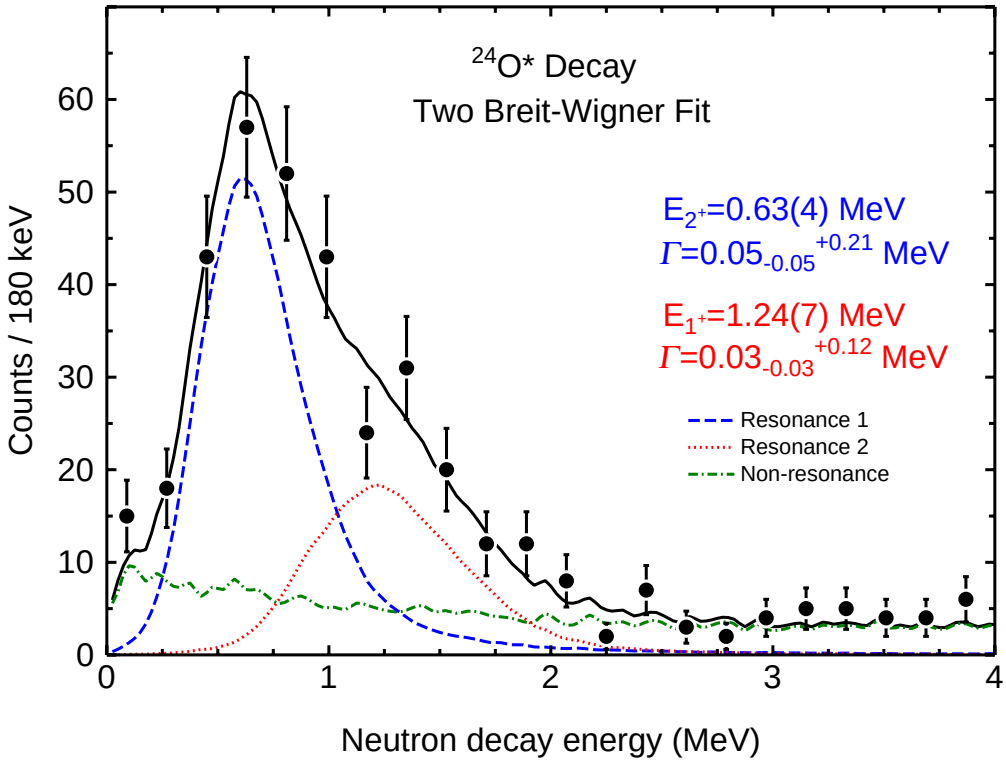

Figure 6.9: The data points represent the measured decay energies for ^{23}O-n coincidences (same as in Fig. 6.8). However, the solid black line in this figure (which provides a better fit to the data) is composed of two independent Breit-Wigner line shapes (dashed, blue and dotted, red) on top of the non-resonance Gaussian distribution (dash-dotted, green). The lower resonance (dashed, blue) has $E_{\rm decay}$ = 0.63(4) MeV and $\Gamma = 0.05^{+0.21}_{-0.05}$ MeV with the upper (dotted, red) having $E_{\rm decay}$ = 1.24(7) MeV and $\Gamma = 0.03^{+0.12}_{-0.03}$ MeV.

0.63(4) MeV and $E_{\rm decay}$ = 1.24(7) MeV are Γ_{sp} = 0.05 MeV and Γ_{sp} = 0.22 MeV, respectively [49]. The predicted single-particle width of the lower energy resonance is in excellent agreement with the observed value $\Gamma = 0.05^{+0.21}_{-0.05}$ MeV while the higher energy resonance has a calculated single-particle width that is outside of the 1 σ upper limit, $\Gamma = 0.03^{+0.12}_{-0.03}$ MeV. It should be noted that the single-particle widths suggest a spectroscopic factor of 1, so a measured value below this value is completely reasonable. Also, although the observed widths are each consistent with Γ = 0 MeV inside of 1 σ, which may indicate an inadequacy for the presence of two excited states, the energies of the observed widths at which χ^2 is a minimum are indeed above 0 MeV (Γ = 0.05 MeV and Γ = 0.03 MeV). Therefore, the experimental data is consistent with the presence of two independent resonances in the

Table 6.7: A table listing the optimum parameters from the fit of the simulated data to the observed decay spectrum for the $^{24}O^{*} \rightarrow ^{23}O+n$ decay assuming two resonances, each with $l = 2$ orbital angular momentum.

Parameter	Optimum Value (Statistical Uncertainty) Units
First State	
Decay Energy (E_{decay})	0.63(4) MeV
Width ($\Gamma(E_{\text{decay}})$)	$0.05^{+0.21}_{-0.05}$ MeV
Orbital Angular Momentum (l)	2
Amplitude of Resonance	1.4
Second State	
Decay Energy (E_{decay})	1.24(7) MeV
Width ($\Gamma(E_{\text{decay}})$)	$0.03^{+0.12}_{-0.03}$ MeV
Orbital Angular Momentum (l)	2
Amplitude of Resonance	1
General	
Gaussian Central Energy	10.0 MeV
Gaussian σ	5.0 MeV
Amplitude of Non-resonance	5

decay spectrum.

Overall, the presence two nearby resonances in the observed decay spectrum gives a slightly better reproduction of the data over the single resonance fit. Coupled with the fact that a doublet of states (2^+, 1^+) with nearly identical configurations are predicted by each theoretical model [13, 27, 11, 2, 29], the results of the two Breit-Wigner line-shape fit are adopted as the description of the observed data in this work. Hence, it is believed that there is a presence of two low-lying unbound excited states in the ^{24}O decay spectrum.

6.2.5 Inferred Spin-Parity Values

The decay scheme for these two excited states in ^{24}O, which decay to the $1/2^+$ ground state in ^{23}O, is shown in Fig. 6.10. The spin-parity values of the observed excited states may be inferred if we revisit the theoretical arguments presented above. As previously stated, the lowest excited single-particle configuration in ^{24}O ($1p-1h$) results in either a 2^+ or 1^+ level. All theoretical calculations that can calculate the doublet of states, predict the 2^+ state as the lower energy of the two [13, 27, 11, 2, 29]. The observed resonance at $E_{\text{decay}} = 0.63(4)$ MeV

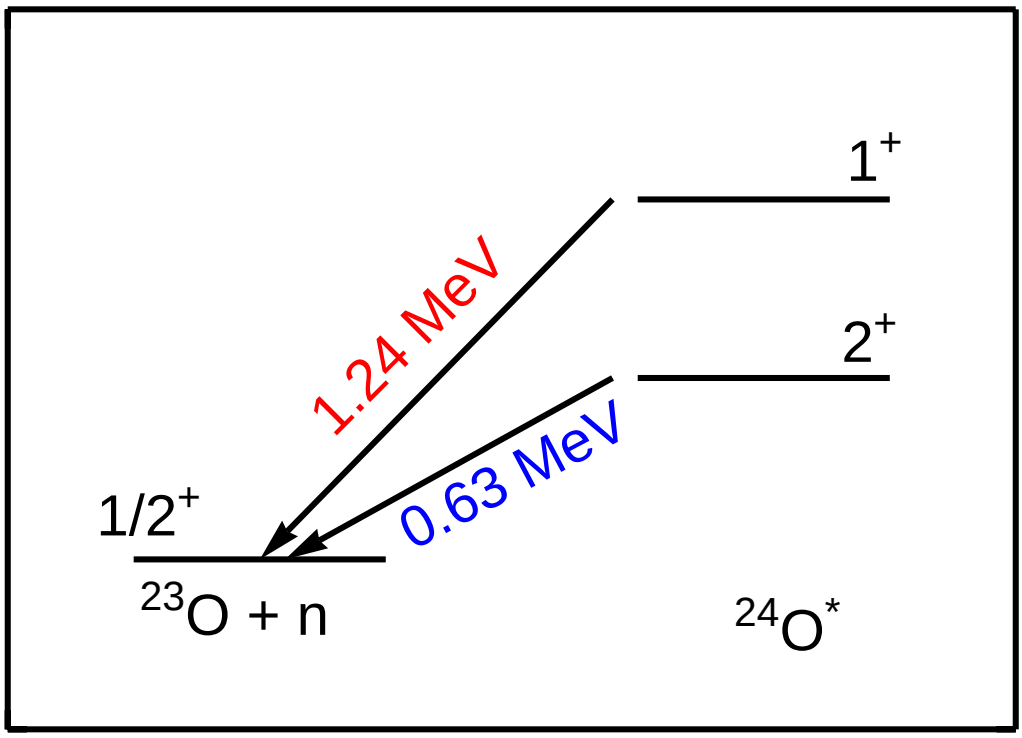

Figure 6.10: The decay paths of the inferred 2^+ (blue) and 1^+ (red) excited states in ^{24}O to the $1/2^+$ ground state of ^{23}O are shown.

can therefore be assumed as the 2^+ state in ^{24}O. The $E_{\text{decay}} = 1.24(7)$ MeV state is then inferred to be the 1^+ excited state. It should be noted that the $E_{\text{decay}} = 1.24(7)$ MeV state is also consistent with $l = 1, 3$ and 4, hence, with other spin-parity values of $1^-, 2^-, 3^-$ or 4^-. However, in this work we have deemed that the most likely case is for the 2^+ and 1^+ states to lie lowest in energy. This assumption is therefore carried throughout the rest of this work.

Experimental support for these spin assignments comes from the consistency of the single-particle widths with Breit-Wigner line-shapes of $l = 2$ orbital angular momentum. Also, the appearance of two states and their inferred spin assignments are supported by the ratio of the intensities of the lower-energy decay branch ($E_{\text{decay}} = 0.63(4)$ MeV) to the higher-energy decay branch ($E_{\text{decay}} = 1.24(7)$ MeV). This ratio is observed to be 1.4(2), determined by the ratio of the resonance amplitude parameters, obtained from the χ^2 fit. This value is consistent with the expected statistical population of a $J = 2$ state to a $J = 1$ state, i.e. the ratio of their magnetic sub-states. This value is $(2J_2 + 1)/(2J_1 + 1) \approx 1.67$.

6.2.6 Determination of the Excited States in ^{24}O

In order to calculate the excitation energy of our assumed 2^+ and 1^+ states, the ground state binding energy difference between ^{23}O and ^{24}O has to been known. The expression for the excitation energy is given as

$$E_{\text{ex}} = S_n + E_{\text{decay}}, \tag{6.8}$$

where S_n is the neutron separation energy between ^{23}O and ^{24}O, and E_{decay} is the observed decay energy. As was mentioned above in the ^{25}O ground state mass section, the binding energy of ^{24}O has been recently remeasured [24]. From this work, and the observations made above, a newly adopted mass excess of 18.6(1) MeV has been accepted over the previous value of the 2003 Atomic Mass Evaluation (AME) [25]. The S_n value for ^{24}O from the newly accepted value is then 4.09(10) MeV, as opposed to 3.62(15) MeV from the 2003 AME value. Again, this value is supported by the previous mass measurements shown in Fig. 6.4. Using the accepted S_n and calculating the excitation energies, we find $E_{2^+} = 4.72(11)$ MeV and $E_{1^+} = 5.33$ MeV for the two excited states above the ^{24}O ground state. The energies of these two states are plotted in Fig. 6.11 by the blue (2^+ level) and red (1^+ level) boxes, where the box size represents the uncertainty in the measurement.

6.2.7 Determination of the $N = 16$ Shell Gap

The $N = 16$ shell gap, the energy difference between the $\nu 1s_{1/2}$ and $\nu 0d_{3/2}$ orbitals, may be determined from the energy of the two excited states in ^{24}O if one believes that indeed the 2^+ and 1^+ states have been identified. Assuming the single-particle picture, with a closed proton $Z = 8$ shell, the two excited states are composed of the same $1p - 1h$ neutron excitation above the $N = 16$ shell. This is the coupling of the $\nu 1s_{1/2}$ and $\nu 0d_{3/2}$ orbitals. These two states would lie degenerate if not for the residual interaction between them. This residual interaction between the 1^+ and 2^+ states, causes them to split in energy relative to the energy of the $\nu 1s_{1/2} - \nu 0d_{3/2}$ single-particle gap. The 2^+ energy is lowered in energy relative to this gap energy, while the 1^+ energy is raised relative to the gap energy. By using a $2J + 1$ weighting for each state the approximate size of the relative energy difference between the $\nu 1s_{1/2}$ and $\nu 0d_{3/2}$ orbitals, and hence, the energy of the $N = 16$ shell gap, is found. This energy is observed to be 4.95(16) MeV from the two excited states in ^{24}O. This value for the $N = 16$ shell gap agrees very well with the energy that was determined above

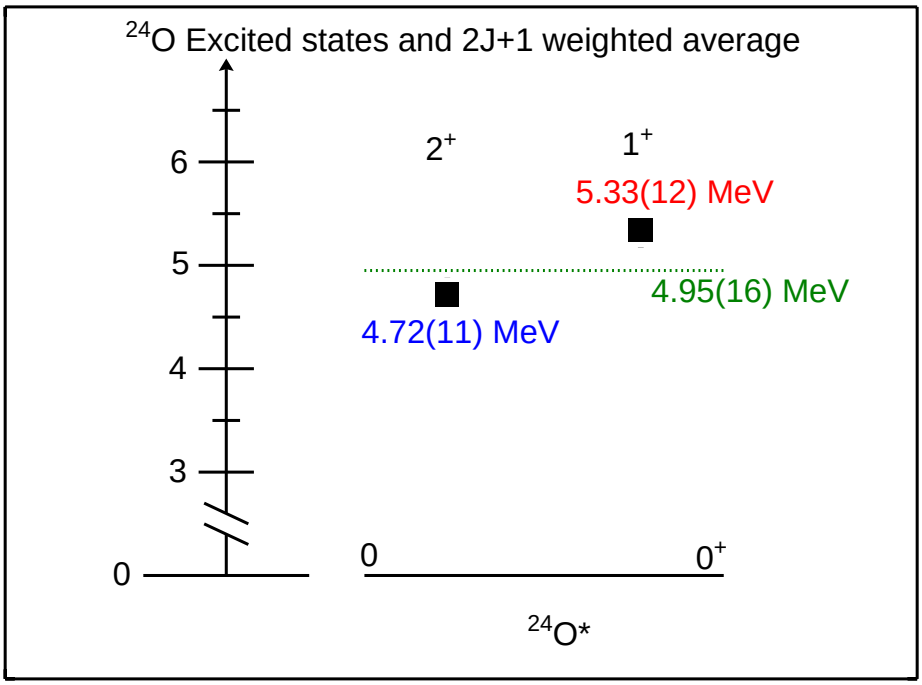

Figure 6.11: The experimental energies of the lowest lying 2^+ ($E_{2^+} = 4.72(11)$ MeV) and 1^+ ($E_{1^+} = 5.33$ MeV) levels in ^{24}O, are shown by the blue and red boxes respectively. The size of the box corresponds to the uncertainty in the energy. Also shown by the dotted green line is the $2J + 1$ weighted average of the two states. This indicates the the size of the $N = 16$ shell at for ^{24}O (4.95(16) MeV), from the observed excited states.

by the ground state mass measurement of ^{25}O (4.86(13) MeV).

CHAPTER 7

DISCUSSION

7.1 $N = 16$ Shell Gap

The size of the $N = 16$ shell gap, defined as the energy difference between the $\nu 1s_{1/2}$ and $\nu 0d_{3/2}$ orbitals, has been determined by two separate measurements. First, it was found from the ground state mass measurement of ^{25}O. The energies of the $\nu 1s_{1/2}$ and $\nu 0d_{3/2}$ orbitals could then both be calculated from the ground state binding energies of ^{25}O, ^{24}O and ^{23}O. The $N = 16$ shell gap was then determined to be 4.86(13) MeV from the energy difference of the two orbitals. Second, the $N = 16$ shell gap was determined by the weighted average of the observed 2^+ and 1^+ excited states in ^{24}O. These two states have an energy gap of 4.95(16) MeV, in very good agreement with the other observation.

The single-particle energies for the $\nu 1s_{1/2}$ and $\nu 0d_{3/2}$ orbitals were determined in chapter 6 to be $\epsilon 0d_{3/2} = 770^{+20}_{-30}$ keV and $\epsilon 1s_{1/2} = -4.09(13)$ MeV. These energies reflect the one-particle and one-hole energies from a closed (0p-0h) ^{24}O ground state. The black data points on the left side of Fig. 7.1 show the single-particle energies for the two orbitals. The difference between the two orbitals, the $N = 16$ shell gap energy, for $N = 15$ and $N = 16$ (present result), are plotted on the right side of Fig. 7.1. The size of the $N = 16$ shell gap for ^{23}O ($N = 15$) was found from an ^{22}O particle transfer experiment [67]. In this work, the $3/2^+$ excited state energy in ^{23}O was observed to be 4 MeV above the $1/2^+$ ground state. The $3/2^+$ state was also noted to be of single-particle nature as it was strongly populated in the particle transfer reaction. Therefore, the excitation energy is a good indication of the energy difference between the $\nu 1s_{1/2}$ and $\nu 0d_{3/2}$ orbitals for $N = 15$ (4 MeV). Experimentally, what can be clearly noticed is an increase of the $N = 16$ shell gap size when moving from $N = 15$ ($N = 16$ shell gap of 4 MeV) to $N = 16$ (gap of $\sim$5 MeV).

Also shown with the data points in Fig. 7.1 are the calculated single-particle levels,

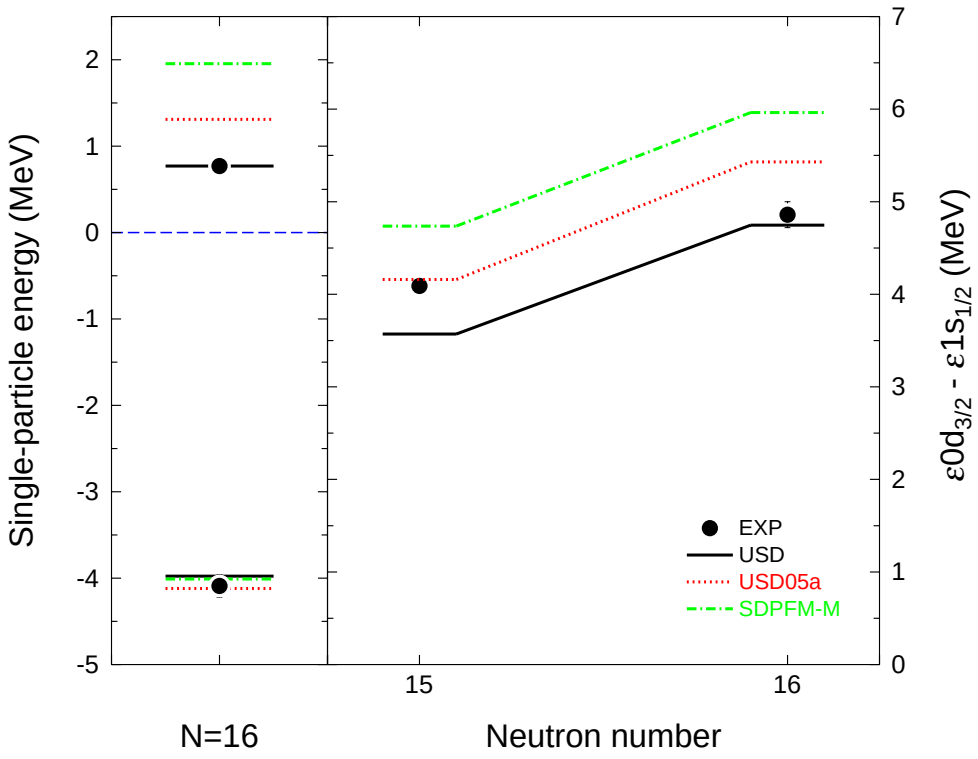

Figure 7.1: The experimental single-particle energies as determined assuming a closed $0p-0h$ ^{24}O are shown on the left by the data points with their error bars if larger than the symbol. The size of the $N-16$ shell gap for $N=15$ and 16 are also plotted by the black data points with their errors on the right side of the figure. The calculated single-particle energies $N=16$ shell gap sizes are also shown for the USD [13] (black solid line), USD05a [27] (red, dotted line), and the SDPF-M [11] (green, dot-dashed) interactions. [28]

and their corresponding $N=16$ shell gaps, for three different shell model interactions, the USD [13], USD05a [27] and the SDPF-M [11] interactions. They are represented by the solid black (USD), dotted red (USD05a) and dash-dotted green (SDPF-M) lines. The dashed line in the figure represents zero energy. As was mentioned in chapter 2 the USD interaction results from an empirically adjusted re-normalized G-matrix, while the USD05a interaction is the same however, fit to more recent data. In the oxygen drip line region, these two interactions have drastically different results as the USD interaction incorrectly calculates a bound ^{26}O ground state by 1 MeV but the USD05a interaction calculates an unbound ground state in agreement with observations. The underlying cause for this change between the two

is an increase in the energy of the $\nu 0d_{3/2}$ orbital for the USD05a interaction. This energy change is apparent in Fig. 7.1, as the energies for the $\nu 1s_{1/2}$ orbital are consistent for all calculations. However, the energies for the $\nu 0d_{3/2}$ orbital all vary by the $\sim$ 500 keV. Also, the SDPF-M interaction is a combination of three separate interactions (USD-WB-MK) to allow calculations across the $sd-fp$ shell gap. It was adjusted to ensure the unbound nature of the ^{26}O ground state. Again, the way that the ^{26}O bound state was made to become unbound to two neutron decay was to adjust the two-body matrix elements (TBME) of the $\nu 0d_{3/2}$ orbital causing its energy to rise. As is seen in Fig. 7.1 its location is high into the continuum, i.e. large positive energy.

Comparing the calculated $N = 16$ shell gap sizes for $N = 15$ and 16 in Fig. 7.1 to the experimental results we see a good agreement between the USD05a prediction for the ^{23}O case. The other two calculations are each off by nearly 500 keV with the SDPF-M interaction over, and the USD interaction under-predicting the energy. This agreement suggests that the USD05a interaction is indeed a good description of the data as the gap is reproduced and the interaction predicts an unbound ^{26}O ground state. However, moving to $N = 16$, the present value for the measurement of the difference between the $\nu 1s_{1/2}$ and $\nu 0d_{3/2}$ orbitals is most consistent with the older USD interaction. Furthermore, when the energies of the two orbitals are separated, as on the left side of Fig 7.1, the discrepancy between the data and the calculations is linked solely to the location of the $\nu 0d_{3/2}$ orbital. All calculations are consistent for the $\nu 1s_{1.2}$ orbital energy; however, the USD interaction is the only calculation that reproduces the energy of the $\nu 0d_{3/2}$ level. The problem this creates is that the USD interaction is the only interaction that incorrectly predicts a bound ^{26}O ground state to two neutron decay.

7.2 Neutron Separation Energies

The oxygen neutron drip line has been experimentally determined to lie at $N = 16$ ^{24}O [35, 36, 37, 7, 6, 38, 39]. This implies that all neutron orbitals above the filled $\nu 1s_{1/2}$ orbital ($N = 16$) must lie in the continuum, i.e. unbound. The first orbital that lies in this continuum is the $\nu 0d_{3/2}$. The energy of the $\nu 0d_{3/2}$ orbital competes with the correlation energy between nucleons to determine whether a nucleus is bound to neutron emission. Therefore, the $\nu 0d_{3/2}$ orbital is vital to the binding energy in all of the oxygen isotopes

above $N = 16$, i.e. $^{25-28}$O. At $N = 17$ neutrons begin to fill this orbital; hence, its location, whether unbound (positive energy) or bound (negative energy), is vital to the overall binding energy of these nuclei. Since ^{25}O is known to be unbound to neutron decay by one neutron, then the $\nu 0d_{3/2}$ orbital must have a positive energy. Also, since the ground state of ^{26}O is unbound to two neutron decay then the positive energy of the $\nu 0d_{3/2}$ orbital must be larger than the pairing energy, as well as other correlations, that lead to negative binding energy effects. The precise energy of the $\nu 0d_{3/2}$ orbital becomes very import to the binding of ^{26}O and the oxygen drip line. Mainly, since a change of a few hundred keV of this orbital's energy, as was the case with the USD [13] interaction versus the USD05a [27] interaction, leads to a different drip line for the oxygen isotopes.

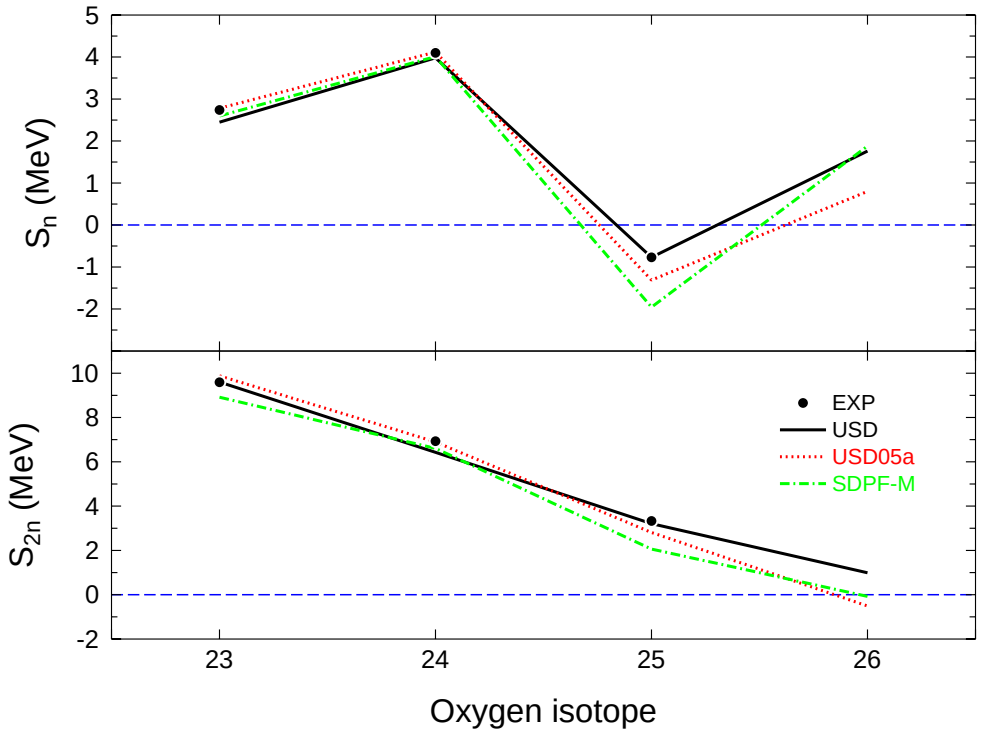

Figure 7.2: The experimental one- and two-neutron separation energies are shown by the black data points with their uncertainties [24, 25] for the neutron-rich oxygen isotopes from $^{23-26}$O. Also, represented by the lines, are the theoretical calculations for these values from the USD [13] (black, solid), USD05a [27] (red, dotted), and SDPF-M [11] (green, dot-dashed) shell model interactions.

To understand the effects of the location of the $\nu 0d_{3/2}$ orbital on the oxygen drip line in a different manner, the one- and two-neutron separation energies (S_n and S_{2n}) are investigated for $Z = 8$ from $N = 15 - 18$. The neutron separation energies were calculated using equations 6.6 and 6.7, where the ground state masses used were from Refs. [25] and [24], in the case of ^{24}O. The current measurement determined the neutron separation energies for ^{25}O (S_n=770^{+20}_{-30} keV and S_{2n} = 3.33(13) MeV).

The S_n and S_{2n} calculated for $^{23-26}$O are plotted in Fig. 7.2 by the black data points. The energy point zero is represented by the blue dashed line and values less than this (< 0) are unbound to neutron decay. The neutron separation energies represent the amount of energy needed to remove the outer most neutron or neutrons. A positive value indicates that the neutron or neutrons are bound to the nucleus by the strong force. A negative energy shows the amount of energy gained by the loss of the neutron or neutrons. This energy translates into the decay energy of the unbound system. A nucleus that lies beyond the drip line is unbound to one–, two–, and all other orders of neutron emission. In the case of ^{26}O, the ground state is believed to be bound by a single-neutron having a binding energy lower the that of the ground state of ^{25}O. However, the ground state is not believed to be lower in energy than the ground state of ^{24}O, and hence, it is unbound by two-neutrons. In any case, if the ground state energy is above either ^{24}O or ^{25}O, then it is beyond the oxygen drip line.

Plotted with the experimental data in Fig. 7.2 are the neutron separation energies calculated from the USD [13], USD05a [27] and SDPF-M [11] interactions. The main difference to notice between these calculations is their location for ^{26}O. They show the unbound predictions of the USD05a and SDPF-M interactions by the fact each predicts a negative energy of -510 keV [27] and -77 keV [11] respectively, with the USD interactions having a positive result of 1 MeV [13]. Calculated values for all three interactions reproduce well the separation energies up to ^{25}O, the present result. Here the calculations diverge, and again the USD interaction is the most consistent with the data. This is important because of the difference in calculations for ^{26}O as was previously mentioned. The main point is that once more it is shown that the USD interaction describes the ^{25}O neutron separation energies for $N = 17$ but incorrectly predicts the binding energy of ^{26}O, where as the other interactions are worse in their reproduction of the data at $N = 17$, making their predictions for ^{26}O uncertain.

7.3 Excited States in ^{24}O

The excited states in nuclei give an excellent testing ground for different theoretical predictions. In the case of ^{24}O, a large number of theoretical endeavors have taken place to predict the lowest excited states. A number of these theoretical predictions [13, 27, 11, 2, 29, 30, 31] for the excitation energies of the 2^+ and 1^+ states in ^{24}O are shown by the lines in Fig. 7.3. The USD [13], USD05 [27] and SDPF-M [11] interactions are standard shell model calculations that have been described in chapter 3. The work of Refs. [2] and [29] are each also shell model calculations using the HBUSD and SDPF-M interactions, respectively. However, each of these also have an explicit inclusion of the continuum in their calculations. The work of Refs. [30] and [31], both calculate the first excited 2^+ by mean field Hartree-Fock-Bogoluibov Methods.

These theoretical predictions are compared with the measured excited levels, assumed to be the 2^+ and 1^+ states, and shown by the black squares in Fig. 7.3. The new universal *sd* interactions (USD05a, and b), and the SDPF-M interaction, all overestimate the absolute energies of the states. The USD05a interaction does correctly predict the residual splitting between the two states ($\sim$600 keV). The USD interaction is far below for the first excited 2^+ state but is in agreement with the 1^+ state. The two Mean Field calculations are both drastically low in energy for the prediction of the 2^+ state. This indicates that they both infer a slightly more deformed ^{24}O nucleus, where as the SDPF-M and USD05 interactions suggest a more spherical ^{24}O than has been observed.

Due to the fact that the states being investigated are resonance states, it is important to isolate calculations that handle the continuum more explicitly than the standard shell model calculations. The continuum calculation using the HBUSD [2] interaction and the predictions of the USD interaction each reproduce only one of the two excited states, as each calculation has an overly large residual energy ($\sim$1.1 MeV). The decay energy predictions of Ref. [29] are the most consistent with the observed results as their calculated values of $E_{2^+} = 0.61$ MeV and $E_{1^+} = 1.35$ MeV, lie within $\sim$100 keV of the observed energies ($E_{2^+} = 0.63(4)$ MeV and $E_{1^+} = 1.24(7)$ MeV). These calculations include the unbound $\nu 0d_{3/2}$ orbital in the wave function, supporting the direct handling of the continuum when describing resonance states near the neutron drip line.

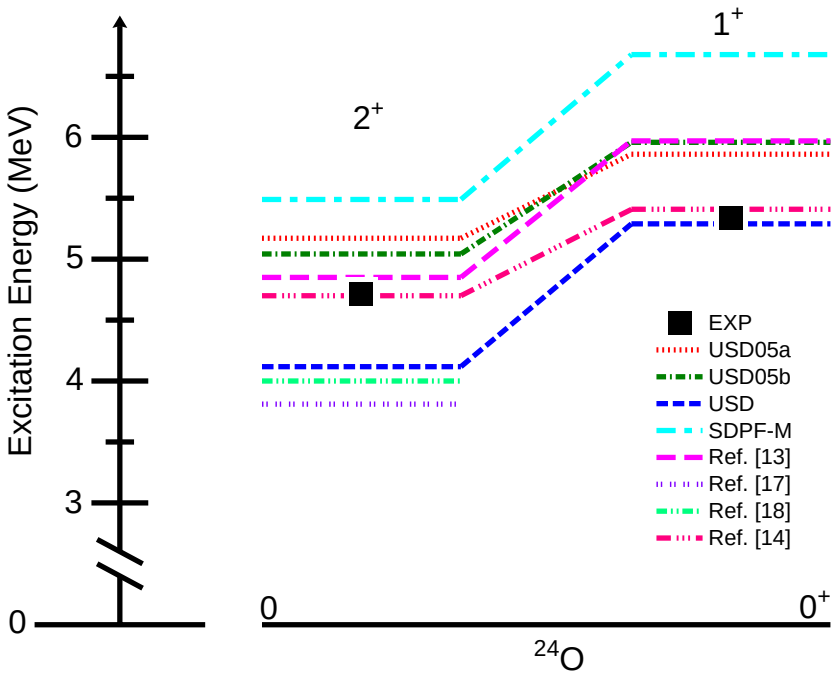

Figure 7.3: The measured energies for the assumed 2_1^+ and 1_1^+ excited states in ^{24}O are shown by the black squares, with the size of the symbol representing the uncertainty. The predicted energies from a number of theoretical calculations [13, 27, 11, 2, 29, 30, 31] are also shown by the different lines. The experimental excitation energies were determined using $E_{\rm ex}(^{24}O) = S_n(^{24}O) + E_{\rm decay}$, where the more recently measured S_n value (4.09(10) MeV) for ^{24}O has been used [24].

7.4 2_1^+ Energy Systematics of the Even-Even Isotopes

The oxygen isotopes have a closed $Z = 8$ proton shell, and therefore systematic investigations of the 2_1^+ energies in the even-even isotopes show great sensitivity to the neutron shell structure. To illustrate this, the energies for the first excited 2_1^+ states in all of the known oxygen isotopes ($Z = 8, N = 6-16$) [32], including the present result at $N = 16$, are plotted in Fig. 7.4 by the filled black squares. At $N = 6$ and 8, ^{14}O and ^{16}O have very high 2_1^+ states (6.5 MeV and 6.7 MeV) consistent with their filled $\nu 0p_{3/2}$ and $\nu 0p_{1/2}$ orbitals, respectively. As neutrons fill the $\nu 0d_{5/2}$ orbital (^{18}O and ^{20}O), the 2_1^+ energy shows a drop of a factor

of $\sim$3 due to the deformation caused by the partially filled neutron orbital. A full $\nu 0d_{5/2}$ orbital again leads to the (sub-)shell closure at $N = 14$ (^{22}O) and is apparent by the increase in the 2_1^+ energy. Finally, a full $\nu 1s_{1/2}$ orbital at $N = 16$ (^{24}O) leads to a dramatic increase in the energy of the 2_1^+ level relative to the $N = 10, 12$ levels and even the $N = 14$ ^{22}O level. Therefore, ^{24}O has a clear signature of an even-even doubly magic nucleus ($Z = 8, N = 16$), namely a relatively high energy 2_1^+ excited state.

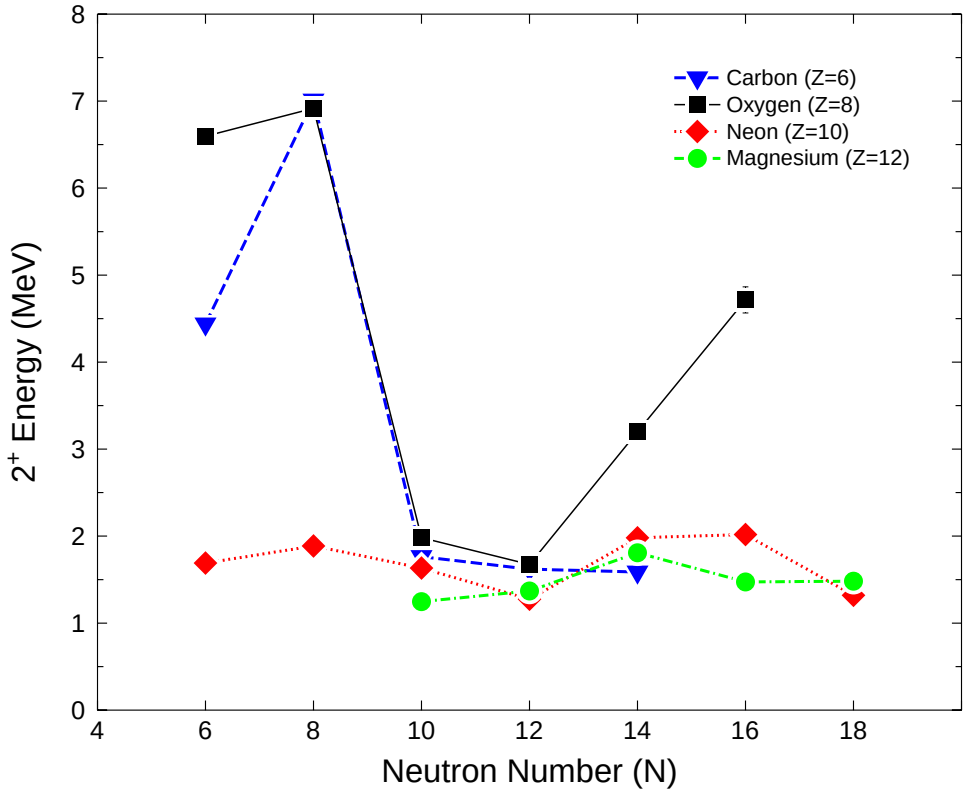

Figure 7.4: The experimental 2_1^+ energies for the even-even isotopes of oxygen $Z = 8$, including the present result at $N = 16$, are shown by the black squares with the errors. Also shown are the experimental 2_1^+ energies for carbon ($Z = 6$) (upside-down triangle, blue) neon ($Z = 10$) (diamond, red) and magnesium ($Z = 12$) (circle, green) [32, 33, 34]. Clearly noticed is the increase in the 2_1^+ energy for the ^{24}O relative to the nearby even-even nuclei; indicating a large $N = 16$ shell gap for $Z = 8$.

Also shown in Fig. 7.4 are the 2^+ energies for the even-even carbon ($Z = 6$), neon ($Z = 10$) and magnesium ($Z = 12$) isotopes having neutron numbers between $N = 6$ and 18 [32, 33, 34]. The energies of the 2_1^+ levels for the $N = 10$ and 12 isotopes are very

similar (∼500 keV) for all of the elements. At $N = 14$ (filled $\nu 0d_{5/2}$ orbital) and $N = 16$ (filled $\nu 1s_{1/2}$ orbital), the 2_1^+ energies of the carbon ($N = 14$ only), neon and magnesium isotopes remain relatively constant as compared to the oxygen isotopes which rise sharply. This reflects the increase in the $N = 14$ and 16 shell gaps for $Z = 8$ relative to $Z = 6, 10$ and 12, again supporting a doubly magic ^{24}O.

7.5 Overview

The measurement of the $\nu 0d_{3/2}$ orbital energy and the size of the $N = 16$ shell gap, sheds light on the structure of the oxygen isotopes at the drip line. In particular, these measurements showed that the older USD shell model interaction [13], is most consistent with the $\nu 0d_{3/2}$ orbital location at the oxygen drip line. This is quite significant being that the USD interaction incorrectly predicts a bound ^{26}O ground state. However, the calculations of the SDPF-M [11] and the USD05a [27] interactions do predict an unbound ^{26}O ground state to two neutrons decay. The difference between the USD interaction and the other two, is a lower energy $\nu 0d_{3/2}$ orbital. Therefore, although the weakening of the spin-orbit force is apparent by the relatively large $N = 16$ shell gap observed for the neutron-rich oxygen isotope, its result of raising the $\nu 0d_{3/2}$ orbital to produce an unbound ^{26}O must not be the complete story. Another, possible large effect near the drip line, may be the presence of the nearby continuum. First evidence for these effects are shown by the reproduction of the excited states in ^{24}O by the continuum calculations of Ref. [29]. It has yet to be shown what these effects may have on both the oxygen and fluorine drip line in a single calculation. Hence, a combination of all these pieces may lead to a full description of bound and unbound states around the neutron drip line.

CHAPTER 8

CONCLUSIONS

In conclusion, neutron unbound states of the neutron-rich oxygen isotopes of ^{25}O and ^{24}O, have been investigated for the first time. The unbound ground state of ^{25}O, and the unbound excited states in ^{24}O, were reconstructed by the invariant mass method. This method used a full kinematic measurement of all decay products. The unbound states were populated by a nucleon removal reaction from a secondary radioactive beam of ^{26}F on a ^{9}Be target. The experiment was conducted at the National Superconducting Cyclotron Laboratory (NSCL) at Michigan State University and the beam was produced by the Coupled Cyclotron Facility (CCF), with isotopic separation completed by the A1900 mass spectrometer [16]. Important components of the experimental setup included beam-line position-sensitive parallel-plate avalanche chambers, a large-gap dipole Sweeper magnet to deflect charged particles after the target, the Modular Neutron Array to detect beam velocity neutrons, and a number of position, time or energy sensitive charge particle detectors to detect fragments after the Sweeper magnet.

The resulting invariant mass resonance spectra were analyzed and fitted using one or two single-level energy dependent Breit-Wigner line-shapes (eq. 3.8) which were derived from the R-matrix theory [47]. A non-resonance contribution to the fit of the decay spectrum was also included by either a Maxwellian distribution (eq. 3.28) for the ^{25}O ground state, or a Gaussian distribution (eq. 3.29) for the ^{24}O excited states. By comparison of the extracted widths of the resonance states ($\Gamma_l(E)$) to single particle predictions, along with the guidance of theoretical shell model calculations [13, 11, 2, 27, 1], the ground state mass properties of ^{25}O and the first two excited states in ^{24}O, were determined.

The ground state mass excess of ^{25}O was observed to have an energy of M_{EX} = 27.44(11) MeV. The energies of the first two excited states in ^{24}O, believed to be the

lowest lying 2^+ and 1^+ states, were found to be at $E_{2^+} = 4.72(11)$ MeV and $E_{1^+} = 5.33$ MeV. The ground state mass measurement of ^{25}O gives the location of the $\nu 0d_{3/2}$ orbital, $\epsilon 0d_{3/2} = 770^{+20}_{-30}$ keV. The energy difference between the $\nu 0d_{3/2}$ orbital and the $\nu 1s_{1/2}$ orbital gives the size of the $N = 16$ shell gap for the oxygen isotopes, which was determined to be $gap_{N=16} = \epsilon 0d_{3/2} - \epsilon 1s_{1/2} = 4.86(13)$ MeV at the oxygen drip line. The $N = 16$ shell gap was also determined from the center of gravity of the two excited states in ^{24}O giving, $gap_{N=16} = 4.95(16)$ MeV. These two measurements were consistent, and they were compared to nuclear shell model calculations using the universal *sd* (USD) [13] interaction, the USD05 [27] interactions, and the SDPF-M [11] interaction. Furthermore, the neutron separation energies (S_n and S_{2n}) for ^{25}O, provided from the ^{25}O ground state mass measurement, were also compared to the theoretical predictions. The final conclusions showed that the location of the $\nu 0d_{3/2}$ orbital, and the size of the $N = 16$ shell gap, agreed with the predictions of the USD interaction. This was surprising because the USD interaction incorrectly calculates a bound ^{26}O ground state, contrary to experiment [35, 36, 37, 7, 6, 38, 39].

The energies of the excited states observed in ^{24}O, taken to be the lowest 2^+ and 1^+ states, were also compared to a number of theoretical calculations [13, 27, 11, 2, 29, 30, 31]. The best reproduction of both states came from a state-of-the-art continuum shell model calculation [29], where the $\nu 0d_{3/2}$ orbital was included explicitly in the continuum. The measured 2^+ energy was also investigated in a systematic manner by comparison with other even-even nuclei in the region. Relative to the other oxygen isotopes, ^{24}O was seen to nearly restore the doubly magic nature that was apparent for the $N = 6$ and 8 ^{14}O and ^{16}O isotopes [32, 33, 34]. In particular, the relatively high energy of the 2^+ state showed the spherical nature and lack of collectivity for ^{24}O. Also, compared to other elements (Z) with neutron numbers around $N = 16$, it was apparent that the increase in 2^+ energy for ^{24}O was far more dramatic than in any other case, i.e. $Z = 10$(Ne) or 12(Mg). Therefore, the variable size of the $N = 16$ shell gap, with respect to proton number, was observed.

The conclusions from the neutron spectroscopy of the neutron-rich ^{25}O and ^{24}O nuclei, show that ^{24}O is a doubly magic nucleus having a new neutron shell gap identified at $N = 16$. Although this new shell gap may contribute to the cause for the abrupt end to the oxygen drip line at $N = 16$, it can not be the complete story. The location of the $\nu 0d_{3/2}$ orbital at the drip line supports the $N = 16$ shell gap. However, its energy is not nearly as high-up in

the continuum (at least 500 keV lower), than the predictions of the USD05a, and SDPF-M interaction, which both correctly predict an unbound ^{26}O ground state. Therefore, this work has been a gateway into the need for further experimental and theoretical exploration along the oxygen drip line.

In a general perspective these measurements impact such things as the basis for nuclear shell structure, the understanding of the existence of nuclei, and the origin of our elements. Magic numbers and shell gaps played crucial roles in the understanding of atomic and nuclear shell structures. Therefore, the identification of one of these pillars of understanding at a different location, can add a strong presence to our expanded understanding. Furthermore, by being able to describe the limit around where nuclei may or may not exist helps to understand the origin of our elements. Stellar explosions may occur at the nuclear extremes and through the study of these nuclei, we may understand both the ingredients and products needed to create all elements around us.

REFERENCES

[1] D. Morris and A. Volya. Web site: https://cygnus.physics.fsu.edu/cosmo (2008). (document), 3.1, 3.5, 3.5, 6.1, 6.1.1, 6.2.1, 6.6, 8

[2] Alexander Volya and Vladimir Zelevinsky. Discrete and continuum spectra in the unified shell model approach. *Phys. Rev. Lett.*, 94:052501, 2005. (document), 3.5, 3.5, 6.1, 6.1.1, 6.2.1, 6.6, 6.2.3, 6.2.4, 6.2.5, 7.3, 7.3, 8

[3] T. Baumann, A. M. Amthor, D. Bazin, B. A. Brown, C. M. Folden III, A. Gade, T. N. Ginter, M. Hausmann, M. Matos caron, D. J. Morrissey, M. Portillo, A. Schiller, B. M. Sherrill, A. Stolz, O. B. Tarasov, and M. Thoennessen. Discovery of ^{40}mg and ^{42}al suggests neutron drip-line slant towards heavier isotopes. *Nature*, 449:1022, 2007. (document), 2.1, 2.1

[4] P. Möller, J. R. Nix, W. D. Myers, and W. J. Swiatecki. Nuclear ground-state masses and deformations. *Atomic Data Nucl. Data Tables*, 59:185, 1995. (document), 2.1

[5] M. Samyn, S. Goriely, M. Bender, and J. M. Pearson. Further explorations of skyrme-hartree-fock-bogoliubov mass formulas. iii. role of particle-number projection. *Phys. Rev. C*, 70:044309, 2004. (document), 2.1

[6] H. Sakurai, S. M. Lukyanov, M. Notani, N. Aoi, D. Beaumel, N. Fukuda, M. Hirai, E. Ideguchi, N. Imai, M. Ishihara, H. Iwasaki, T. Kubo, K. Kusaka, H. Kumagai, T. Nakamura, H. Ogawa, Yu. E. Penionzhkevich, T. Teranishi, Y. X. Watanabe, K. Yoneda, and A. Yoshida. Evidence for particle stability of 31f and particle instability of 25n and 28o. *Phys. Lett. B*, 448:180–184, 1999. (document), 2.1, 2.2, 5.3.3, 7.2, 8

[7] O. Tarasov, R. Allatt, J. C. Angelique, R. Anne, C. Borcea, Z. Dlouhy, C. Donzaud, S. Grevy, D. Guillemaud-Mueller, M. Lewitowicz, S. Lukyanov, A. C. Mueller, F. Nowacki, Yu. Oganessian, N. A. Orr, A. N. Ostrowski, R. D. Page, Yu. Penionzhkevich, F. Pougheon, A. Reed, M. G. Saint-Laurent, W. Schwab, E. Sokol, O. Sorlin, W. Trinder, and J. S. Winfield. Search for 28o and study of neutron-rich nuclei near the n = 20 shell closure. *Phys. Lett. B*, 409:64–70, 1997. (document), 2.1, 2.2, 5.3.3, 7.2, 8

[8] A. Ozawa, T. Kobayashi, T. Suzuki, K. Yoshida, and I. Tanihata. New magic number, $n = 16$, near the neutron drip line. *Phys. Rev. Lett.*, 84:5493, 2000. (document), 2.2, 2.4

[9] M. Stanoiu, F. Azaiez, Zs. Dombrádi, O. Sorlin, B. A. Brown, M. Belleguic, D. Sohler, M. G. Saint Laurent, M. J. Lopez-Jimenez, Y. E. Penionzhkevich, G. Sletten, N. L. Achouri, J. C. Angélique, F. Becker, C. Borcea, C. Bourgeois, A. Bracco, J. M. Daugas, Z. Dlouhý, C. Donzaud, J. Duprat, Zs. Fülöp, D. Guillemaud-Mueller, S. Grévy, F. Ibrahim, A. Kerek, and A. Krasznahorkay. $n = 14$ and 16 shell gaps in neutron-rich oxygen isotopes. *Phys. Rev. C*, 69:034312, 2004. (document), 2.2, 2.5, 6.1.1, 6.2.1

[10] B. Alex Brown and W. A. Richter. Magic numbers in the neutron-rich oxygen isotopes. *Phys. Rev. C*, 72:057301, 2005. (document), 2.6

[11] Yutaka Utsuno, Takaharu Otsuka, Takahiro Mizusaki, and Michio Honma. Varying shell gap and deformation in $n \sim 20$ unstable nuclei studied by the monte carlo shell model. *Phys. Rev. C*, 60:054315, 1999. (document), 2.1, 2.3, 2.7, 2.3, 3, 3.1, 3.5, 3.5, 6.1.1, 6.1.1, 6.2.1, 6.2.3, 6.2.4, 6.2.5, 7.1, 7.2, 7.3, 7.3, 7.5, 8

[12] T. Otsuka, Y. Utsuno, R. Fujimoto, B.A. Brown, M. Honma, and T. Mizusak. Frontiers and challenges of nuclear shell model. *Eur. Phys. J. A*, 15:151, 2002. (document), 2.3, 2.7, 2.3

[13] B. A. Brown and B. H. Wildenthal. Status of the nuclear shell model. *Ann. Rev. Part. Nucl. Sci.*, 38:29, 1988. (document), 2.1, 2.3, 2.3, 3, 3.1, 3.1, 3.5, 3.5, 6.1.1, 6.1.1, 6.2.1, 6.2.3, 6.2.3, 6.2.4, 6.2.5, 7.1, 7.2, 7.2, 7.3, 7.3, 7.5, 8

[14] M. Thoennessen, T. Baumann, B. A. Brown, J. Enders, N. Frank, P. G. Hansen, P. Heckman, B. A. Luther, J. Seitz, A. Stolz, and E. Tryggestad. Single proton knock-out reactions from $f24, 25, 26$. *Phys. Rev. C*, 68:044318, 2003. (document), 3.1, 3.1, 3.2, 5.3.3

[15] H. Scheit. Simple track for mona. Technical report, NSCL, 2006. (document), 3.4, 3.3.2, 5.1, 5.4, 5.14, 6.1

[16] D. J. Morrissey, B. M. Sherrill, M. Steiner, A. Stolz, and I. Wiedenhoever. Commissioning the a1900 projectile fragment separator. *Nucl. Instr. Meth. B*, 204:90, 2003. (document), 4.1.1, 4.1, 5.3.1, 8

[17] M. D. Bird, S. J. Kenney, J. Toth, H. W. Weijers, J. C. DeKamp, M. Thoennessen, and A. Zeller. System testing and installation of the nhmfl/nscl sweeper magnet. *IEEE Trans. Appl. Supercond.*, 15:1252, 2005. (document), 4.2, 4.2, 4.2.3, 5.3.4

[18] W. A. Peters. *Study of Neutron Unbound States Using the Modular Neutron Array (MoNA)*. PhD Thesis, Michigan State University, 2007. (document), 4.2.6, 4.6, 5.2.1, 5.4

[19] N. Frank, A. Schiller, D. Bazin, W.A. Peters, , and M. Thoennessen. Reconstruction of nuclear charged fragment trajectories from a large-gap sweeper magnet. *Nucl. Instr. Meth. A*, 580:1478–1484, 2007. (document), 5.3.4, 5.7, 5.3.4, 5.8

[20] N. Frank. *Spectroscopy of Neutron Unbound States in the Neutron Rich Oxygen Isotopes*. PhD Thesis, Michigan State University, 2006. (document), 4.2.3, 4.2.6, 5.2.4, 5.7, 5.3.4, 5.8, 5.4

[21] A. Gillibert, W. Mittig, L. Bianchi, A. Cunsolo, B. Fernandez, A. Foti, J. Gastebois, C. Gregoire, Y. Schutz, and C. Stephan. New mass measurements far from stability. *Phys. Lett. B*, 192:39–43, 1987. (document), 6.1.3, 6.4

[22] J. M. Wouters, R. H. Kraus, D. J. Vieira, G. W. Butler, and K. E. G. Löbner. Direct mass measurements of the neutron-rich light isotopes of lithium through fluorine. *Z. Phys. A*, 331:229–233, 1988. (document), 6.1.3, 6.4

[23] N. A. Orr, W. Mittig, L. K. Fifield, M. Lewitowicz, E. Plagnol, Y. Schutz, Zhan Wen Long, L. Bianchi, , A. Gillibert, A. V. Belozyorov, S. M. Lukyanov, , Yu. E. Penionzhkevich, A. C. C. Villari, A. Cunsolo, , A. Foti, G. Audi, C. Stephan, , and L. Tassan-Got. New mass measurements of neutron-rich nuclei near n=20. *Phys. Lett. B*, 258:29–34, 1991. (document), 6.1.3, 6.1.3, 6.4

[24] B. Jurado, H. Savajols, W. Mittig, N.A. Orr, P. Roussel-Chomaz, D. Baiborodin, W.N. Catford, M. Chartier, C.E. Demonchy, Z. Dlouhy, A. Gillibert, L. Giot, A. Khouaja, A. Lepine-Szily, S. Lukyanov, J. Mrazek, Y.E. Penionzhkevich, S. Pita, M. Rousseau, and A.C. Villari. Mass measurements of neutron-rich nuclei near the n=20 and 28 shell closures. *Phys. Lett. B*, 649:43, 2007. (document), 2.2, 6.1.3, 6.1.3, 6.4, 6.1.5, 6.2.6, 7.2, 7.3

[25] G. Audi, O. Bersillon, J. Blachot, and A. H. Wapstra. The evaluation of nuclear and decay properties. *Nucl. Phys. A*, 729:3, 2003. (document), 6.1.3, 6.1.3, 6.4, 6.1.5, 6.2.6, 7.2

[26] E. Sauvan, F. Carstoiu, N. A. Orr, J. C. Angelique, W. N. Catford, N. M. Clarke, M. Mac Cormick, N. Curtis, M. Freer, S. Grevy, C. Le Brun, M. Lewitowicz, E. Liegard, F. M. Marques, P. Roussel-Chomaz, M. G. Saint Laurent, M. Shawcross, and J. S. Winfield. One-neutron removal reactions on neutron-rich psd-shell nuclei. *Phys. Lett. B*, 491:1–7, 2000. (document), 6.5, 6.2.1

[27] B. Alex Brown and W. A. Richter. New "usd" hamiltonians for the sd shell. *Phys. Rev. C*, 74:034315, 2006. (document), 2.1, 2.3, 3, 3.1, 3.5, 3.5, 6.1.1, 6.1.1, 6.2.1, 6.2.3, 6.2.3, 6.2.4, 6.2.5, 7.1, 7.2, 7.2, 7.3, 7.3, 7.5, 8

[28] C. R. Hoffman, T. Baumann, D. Bazin, J. Brown, G. Christian, P. A. DeYoung, J. E. Finck, N. Frank, J. Hinnefeld, R. Howes, P. Mears, E. Mosby, S. Mosby, J. Reith, B. Rizzo, W. F. Rogers, G. Peaslee, W. A. Peters, A. Schiller, M. J. Scott, S. L. Tabor, M. Thoennessen, P. J. Voss, and T. Williams. Determination of the n = 16 shell closure at the oxygen drip line. *Phys. Rev. Lett.*, 100:152502, 2008. (document), 7.1

[29] K. Tsukiyama, T. Otsuka, and R. Fujimoto. Continuum effects for the shell-model calculation of the low-lying states of oxygen drip line. *To be published*. (document), 6.2.1, 6.2.3, 6.2.4, 6.2.5, 7.3, 7.3, 7.5, 8

[30] A. Obertelli, S. Péru, J. P. Delaroche, A. Gillibert, M. Girod, and H. Goutte. N = 16 subshell closure from stability to the neutron drip line. *Phys. Rev. C*, 71:024304, 2005. (document), 7.3, 7.3, 8

[31] E. Khan, N. Sandulescu, M. Grasso, and Nguyen Van Giai. Continuum quasiparticle random phase approximation and the time-dependent hartree-fock-bogoliubov approach. *Phys. Rev. C*, 66:024309, 2002. (document), 7.3, 7.3, 8

[32] Web site: www.nndc.bnl.gov (2007). (document), 7.4, 7.4, 8

[33] M. Stanoiu, F. Azaiez, F. Becker, M. Belleguic, C. Borcea, C. Bourgeois, B.A. Brown, Z. Dlouh, Z. Dombrdi, Z. Flp, H. Grawe, S. Grvy, F. Ibrahim, A. Kerek, A. Krasznahorkay, M. Lewitowicz, S. Lukyanov, H. van der Marel, P. Mayet, J. Mrzek, S. Mandal, D. Guillemaud-Mueller, F. Negoita, Y.E. Penionzhkevich, Z. Podolyk, P. Roussel-Chomaz, M.G. Saint Laurent, H. Savajols, O. Sorlin, G. Sletten, D. Sohler, J. Timr, C. Timis, and A. Yamamoto. Study of drip line nuclei through two-step fragmentation. *Eur. Phys. J. A*, 20:95, 2004. (document), 7.4, 8

[34] M. Stanoiu, D. Sohler, O. Sorlin, F. Azaiez, Zs. Dombrádi, B. A. Brown, M. Belleguic, C. Borcea, C. Bourgeois, Z. Dlouhy, Z. Elekes, Zs. Fülöp, S. Grévy, D. Guillemaud-Mueller, F. Ibrahim, A. Kerek, A. Krasznahorkay, M. Lewitowicz, S. M. Lukyanov, S. Mandal, J. Mrázek, F. Negoita, Yu.-E. Penionzhkevich, Zs. Podolyák, P. Roussel-Chomaz, M. G. Saint-Laurent, H. Savajols, G. Sletten, J. Timár, C. Timis, and A. Yamamoto. Disappearance of the n = 14 shell gap in the carbon isotopic chain. *Phys. Rev. C*, 78:034315, 2008. (document), 7.4, 8

[35] M. Langevin, E. Quiniou, M. Bernas, J. Galin, J. C. Jacmart, F. Naulin, F. Pougheon, R. Anne, C. Detraz, D. Guerreau, D. Guillemaud-Mueller, and A. C. Mueller. Production of neutron-rich nuclei at the limits of particles stability by fragmentation of 44 mev/u 40ar projectiles. *Phys. Lett. B*, 150:71–74, 1985. 2.1, 7.2, 8

[36] D. Guillemaud-Mueller, J. C. Jacmart, E. Kashy, A. Latimier, A. C. Mueller, F. Pougheon, A. Richard, Yu. E. Penionzhkevich, A. G. Artuhk, A. V. Belozyorov, S. M. Lukyanov, R. Anne, P. Bricault, C. Détraz, M. Lewitowicz, Y. Zhang, Yu. S. Lyutostansky, M. V. Zverev, D. Bazin, and W. D. Schmidt-Ott. Particle stability of the isotopes *o*26 and *ne*32 in the reaction 44 mev/nucleon *ca*48+ta. *Phys. Rev. C*, 41:937, 1990. 2.1, 5.3.3, 7.2, 8

[37] M. Fauerbach, D. J. Morrissey, W. Benenson, B. A. Brown, M. Hellström, J. H. Kelley, R. A. Kryger, R. Pfaff, C. F. Powell, and B. M. Sherrill. New search for *o*26. *Phys. Rev. C*, 53:647–651, 1996. 2.1, 5.3.3, 7.2, 8

[38] Z Dlouhú ¡i¿et al¡/i¿. Dripline nuclei produced by quasi-fragmentation of the 32, 34, 36s primary beams. *Journal of Physics G: Nuclear and Particle Physics*, 25(4):859–862, 1999. 2.1, 7.2, 8

[39] S. M. Lukyanov and Yu. E. Penionzhkevich. The neutron drip line in the region of n = 20 and n = 28 closures. *Phys. Atomic. Nucl.*, 67:1627, 2004. 2.1, 5.3.3, 7.2, 8

[40] Yutaka Utsuno, Takaharu Otsuka, Takahiro Mizusaki, and Michio Honma. Extreme location of f drip line and disappearance of the $n = 20$ magic structure. *Phys. Rev. C*, 64:011301, 2001. 2.1, 3.5

[41] P. G. Thirolf, B. V. Pritychenko, B. A. Brown, P. D. Cottle, M. Chromik, T. Glasmacher, G. Hackman, R. W. Ibbotson, K. W. Kemper, T. Otsuka, L. A. Riley, and H. Scheit. Spectroscopy of the 21+ state in 22o and shell structure near the neutron drip line. *Phys. Lett. B*, 485:16, 2000. 2.2, 2.3

[42] M. Belleguic, M. J. Lopez-Jimenez, M. Stanoiu, F. Azaiez, M. G. Saint-Laurent, O. Sorlin, N. L. Achouri, J. C. Angelique, C. Bourgeois, C. Borcea, J. M. Daugas, C. Donzaud, F. De Oliveira-Santos, J. Duprat, S. Grevy, D. Guillemaud-Mueller, S. Leenhardt, M. Lewitowicz, Yu. E. Penionzhkevich, and Yu. Sobolev. In-beam γ–spectroscopy using projectile fragmentation: Structure of neutron-rich nuclei around n = 20. *Nucl. Phys. A*, 682:136c, 2001. 2.2, 2.3

[43] Takaharu Otsuka, Rintaro Fujimoto, Yutaka Utsuno, B. Alex Brown, Michio Honma, and Takahiro Mizusaki. Magic numbers in exotic nuclei and spin-isospin properties of the *nn* interaction. *Phys. Rev. Lett.*, 87:082502, 2001. 2.3

[44] B. M. Sherrill. Scientific opportunities with in-flight separated beams. *Nuclear Physics A*, 701:422 – 428, 2002. 3.1

[45] A. T. Reed, O. Tarasov, R. D. Page, D. Guillemaud-Mueller, Yu. E. Penionzhkevich, R. G. Allatt, J. C. Angélique, R. Anne, C. Borcea, V. Burjan, W. N. Catford, Z. Dlouhý, C. Donzaud, S. Grévy, M. Lewitowicz, S. M. Lukyanov, F. M. Marqués, G. Martinez, A. C. Mueller, P. J. Nolan, J. Novák, N. A. Orr, F. Pougheon, P. H. Regan, M. G. Saint-Laurent, T. Siiskonen, and E. Sokol. Radioactivity of neutron-rich oxygen, fluorine, and neon isotopes. *Phys. Rev. C*, 60:024311, 1999. 3.1

[46] A. Schiller, N. Frank, T. Baumann, D. Bazin, B. A. Brown, J. Brown, P. A. DeYoung, J. E. Finck, A. Gade, J. Hinnefeld, R. Howes, J.-L. Lecouey, B. Luther, W. A. Peters, H. Scheit, M. Thoennessen, and J. A. Tostevin. Selective population and neutron decay of an excited state of ^{23}o. *Phys. Rev. Lett.*, 99:112501, 2007. 3.1, 5.3.3

[47] A. M. Lane and R. G. Thomas. R-matrix theory of nuclear reactions. *Rev. Mod. Phys.*, 30:257–353, 1958. 3.3.1, 3.3.1, 8

[48] G. Breit and E. Wigner. Capture of slow neutrons. *Phys. Rev.*, 49:519, 1936. 3.3.1

[49] A .Bohr and B. R. Mottelson. *Nuclear Structure*, volume 1. World Scientific Publishing Co. Pte. Ltd., 1998. 3.4, 6.2.4

[50] Maria Goeppert Mayer. On closed shells in nuclei. ii. *Phys. Rev.*, 75:1969, 1949. 3.5

[51] Otto Haxel, J. Hans D. Jensen, and Hans E. Suess. On the "magic numbers" in nuclear structure. *Phys. Rev.*, 75:1766, 1949. 3.5

[52] Kris L. G. Heyde. *The Nuclear Shell Model*. Springer-Verlag Berlin Heidelberg, 2 edition, 1990. 3.5

[53] B. Alex Brown. The nuclear shell model towards the drip lines. *Prog. Part. Nuc. Phys.*, 47:517, 2001. 3.5, 6.1.4

[54] B. A. Brown, A. Etchegoyen, N. S. Godwin, W. D. M. Rae, W. A. Richter, W. E. Ormand, E. K. Warburton, J. S. Winfield, L. Zhoa, and C. H. Zimmerman. Oxbash for windows. Technical report, NSCL/MSU, 2005. Report No. 1289. 3.5, 3.5

[55] C. Thibault, R. Klapisch, C. Rigaud, A. M. Poskanzer, R. Prieels, L. Lessard, and W. Reisdorf. Direct measurement of the masses of $li11$ and $na26-32$ with an on-line mass spectrometer. *Phys. Rev. C*, 12:644–657, 1975. 3.5, 3.5

[56] T. T. S. Kuo and G. E. Brown. Reaction matrix elements for the 0f-1p shell nuclei. *Nuclear Physics A*, 114:241 – 279, 1968. 3.5

[57] E. K. Warburton, D. E. Alburger, J. A. Becker, B. A. Brown, and S. Raman. Probe of the shell crossing at a=40 via beta decay: Experiment and theory. *Phys. Rev. C*, 34:1031–1051, 1986. 3.5

[58] D.J. Millener and D. Kurath. The particle-hole interaction and the beta decay of 14b. *Nuclear Physics A*, 255:315 – 338, 1975. 3.5

[59] Vandana Tripathi, S. L. Tabor, P. F. Mantica, Y. Utsuno, P. Bender, J. Cook, C. R. Hoffman, Sangjin Lee, T. Otsuka, J. Pereira, M. Perry, K. Pepper, J. S. Pinter, J. Stoker, A. Volya, and D. Weisshaar. Competition between normal and intruder states inside the "island of inversion". *Phys. Rev. C*, 76:021301, 2007. 3.5

[60] T. Baumann, J. Boike, J. Brown, M. Bullinger, J.P. Bychoswki, S. Clark, K. Daum, P.A. DeYoung, J.V. Evans, J. Finck, N. Frank, A. Grant, J. Hinnefeld, G.W. Hitt, R.H. Howes, B. Isselhardt, K.W. Kemper, J. Longacre, Y. Lu, B. Luther, S.T. Marley, D. McCollum, E. McDonald, U. Onwuemene, P.V. Pancella, G.F. Peaslee, W.A. Peters, M. Rajabali, J. Robertson, W.F. Rogers, S.L. Tabor, M. Thoennessen, E. Tryggestad, R.E. Turner, P.J. VanWylen, and N. Walker. Construction of a modular large-area neutron detector for the nscl. *Nucl. Instr. Meth. A*, 543:517–527, 2005. 4.2, 5.2.1, 5.3.5

[61] R. Fox. Spectcl user's guide. Technical report, NSCL/MSU, 2003. http://docs.nscl.msu.edu/daq/spectcl. 5.1

[62] M. Berz, K. Joh, J. A. Nolen, B. M. Sherrill, and A. F. Zeller. Reconstructive correction of aberrations in nuclear particle spectrographs. *Phys. Rev. C*, 47:537, 1993. 5.3.4, 5.3.4

[63] Kyoko Makino and Martin Berz. Cosy infinity version 9. *Nucl. Instr. Meth. A*, 558:346, 2006. 5.3.4, 5.3.4

[64] Geant3: Cern program library long writeup q121, 1994. 5.4

[65] Web site: http://physics.nist.gov/cuu/Constants/index.html(2008). 6.1.3, 6.1.3, 6.1.5

[66] A. Ozawa, T. Suzuki, and I. Tanihata. Nuclear size and related topics. *Nucl. Phys. A*, 693:32, 2001. 6.2.3

[67] Z. Elekes, Zs. Dombrádi, N. Aoi, S. Bishop, Zs. Fülöp, J. Gibelin, T. Gomi, Y. Hashimoto, N. Imai, N. Iwasa, H. Iwasaki, G. Kalinka, Y. Kondo, A. A. Korsheninnikov, K. Kurita, M. Kurokawa, N. Matsui, T. Motobayashi, T. Nakamura, T. Nakao, E. Yu. Nikolskii, T. K. Ohnishi, T. Okumura, S. Ota, A. Perera, A. Saito, H. Sakurai, Y. Satou, D. Sohler, T. Sumikama, D. Suzuki, M. Suzuki, H. Takeda, S. Takeuchi, Y. Togano, and Y. Yanagisawa. Spectroscopic study of neutron shell closures via nucleon transfer in the near-dripline nucleus ^{23}o. *Phys. Rev. Lett.*, 98:102502, 2007. 7.1

BIOGRAPHICAL SKETCH

Calem R. Hoffman

Calem R. Hoffman was born on March 21, 1982 in Dansville, NY. He graduated from Wayland-Cohocton Central School in the spring of 2000. He completed his Bachelors degree in Physics in the fall of 2003. It was during this time that he began work under Dr. Samuel Tabor on Nuclear Structure Physics. He pursued his doctorate degree in Nuclear Physics at Florida State University under Dr. Tabor.

Calem's research interest include the structure of exotic nuclei far from the line of stability. His personal interests include watching and participating in all sports, music, and travel. He has accepted a post-doctoral position at the prestigious Argonne National Laboratory located outside Chicago, IL.